NONCONFORMING FORMULATIONS WITH SPECTRAL ELEMENT METHODS

A Dissertation

by

CUNEYT SERT

Submitted to the Office of Graduate Studies of
Texas A&M University
in partial fulfillment of the requirements for the degree of

DOCTOR OF PHILOSOPHY

August 2003

Major Subject: Mechanical Engineering

NONCONFORMING FORMULATIONS

WITH SPECTRAL ELEMENT METHODS

A Dissertation

by

CUNEYT SERT

Submitted to Texas A&M University
in partial fulfillment of the requirements
for the degree of

DOCTOR OF PHILOSOPHY

Approved as to style and content by:

Ali Beskok (Chair of Committee)	
J. N. Reddy (Member)	N. K. Anand (Member)
Paul Cizmas (Member)	Dennis O'Neal (Head of Department)

August 2003

Major Subject: Mechanical Engineering

ABSTRACT

Nonconforming Formulations with Spectral Element Methods. (August 2003)

Cuneyt Sert, B.S., Middle East Technical University;

M.S., Middle East Technical University

Chair of Advisory Committee: Dr. Ali Beskok

A spectral element algorithm for solution of the incompressible Navier-Stokes and heat transfer equations is developed, with an emphasis on extending the classical conforming Galerkin formulations to nonconforming spectral elements. The new algorithm employs both the Constrained Approximation Method (CAM), and the Mortar Element Method (MEM) for p-and h-type nonconforming elements. Detailed descriptions, and formulation steps for both methods, as well as the performance comparisons between CAM and MEM, are presented. This study fills an important gap in the literature by providing a detailed explanation for treatment of p-and h-type nonconforming interfaces. A comparative eigenvalue spectrum analysis of diffusion and convection operators is provided for CAM and MEM. Effects of consistency errors due to the nonconforming formulations on the convergence of steady and time dependent problems are studied in detail. Incompressible flow solvers that can utilize these nonconforming formulations on both p-and h-type nonconforming grids are developed and validated. Engineering use of the developed solvers are demonstrated by detailed parametric analyses of oscillatory flow forced convection heat transfer in two-dimensional channels.

ACKNOWLEDGMENTS

I want to thank my advisor Dr. Ali Beskok for providing me this graduate study opportunity. He was always supportive, understanding and very friendly. I learned a lot from him as an academician and a researcher. I also want to thank Mrs. Beskok, for her friendly and welcoming attitude towards my family during our stay in College Station.

I am also thankful to my committee members, Dr. J.N. Reddy, Dr. P. Cizmas, Dr. N.K. Anand and Dr. M. Andrews for supervising and evaluating my work.

I can not thank my wife, Aytulu, enough for the love and support she has provided since the day we met. It would have been impossible to finish this study without her. I wish I had five more years that I can spend just to thank her. I am also thankful to my little daughter, Elif, for the last minute joy she brought to this work.

Every single day in the last five years, my mind has travelled thousands of miles back to Turkey. I have missed my family back there a lot. Thank you all for your unconditional support. I am happy that I'll be back soon.

I feel very lucky to have worked with my officemates Pradip, Imtiaz, Prashanta and Mr. Hahm. I hope you feel the same way. Thank you all for being a part of this experience. And, Saurabh, your sudden loss saddened all of us a lot. You were a really good friend of mine, rest in peace.

Son olarak Semsettin babama da tesekkur etmek istiyorum. Gider insallah o kadar uzaga.

TABLE OF CONTENTS

CHAPTER Page

I INTRODUCTION 1

A. Background 1
1. Spectral and Spectral Element Methods 1
2. Nonconforming Formulations 5
B. Literature Survey 8
C. Specific Objectives 10
D. Organization of Thesis 10
E. Nomenclature 11

II CONFORMING GALERKIN SPECTRAL ELEMENT FORMULATION 13

A. Steady Formulation 13
B. Semi-discrete Formulation 19

III NONCONFORMING FORMULATIONS, CAM AND MEM . . 21

A. Definitions About Nonconformities 21
B. Constrained Approximation Method (CAM) 24
C. Mortar Element Method (MEM) 31

IV CONVERGENCE AND EIGENVALUE ANALYSIS OF THE DIFFUSION AND CONVECTION OPERATORS 42

A. Steady Diffusion Operator 42
1. Spectral Convergence on a Conforming Mesh 43
2. Convergence on a p-type Nonconforming Mesh 44
3. Convergence Problems of CAM with the Maximum Rule 46
4. Convergence on an h-type Nonconforming Mesh 48
B. Eigenvalue Analysis of the Diffusion Operator 49
C. Eigenvalue Analysis of the Convection Operator 50
D. Convergence Analysis of the Pure Convection Equation . . 56
E. Convergence Analysis of the Convection-Diffusion Equation 62

CHAPTER Page

V INCOMPRESSIBLE STOKES AND NAVIER-STOKES EQUATIONS 64

A. Governing Equations 64
B. Typical Numerical Solution Techniques 65
C. Galerkin Spectral Element Formulation of the Navier-Stokes Equations 67
D. Uzawa Method 70
1. Uzawa Method for Steady Problems 71
2. Uzawa Method for Time Dependent Problems 71
E. Test Problems 73
1. Oscillatory Flow in a Channel 73
2. Kovasznay Flow 75
3. Lid-Driven Cavity Problem 77

VI APPLICATION: OSCILLATORY FLOW FORCED CONVECTION IN TWO-DIMENSIONAL CHANNELS 81

A. Background 81
B. Problem Definition and Important Parameters 84
C. Non-Dimensionalization and Governing Equations 88
D. Analytical Solution of the Velocity Field 89
E. Results 91
1. Temperature Contours 92
2. Temperature Profiles 94
3. Top-Wall Temperature Variations 95
4. Bulk Temperature and the Nusselt Number 98
5. Steady Unidirectional Forced Convection 102
F. Summary of Oscillatory Forced Convection Studies 103

VII SUMMARY AND DISCUSSIONS 106

REFERENCES 110

VITA 118

LIST OF FIGURES

FIGURE		Page
1	Domain and element discretization of a one-dimensional problem . .	4
2	Three commonly used refinement strategies	7
3	Model problem	14
4	Element discretization for a typical two-dimensional quadrilateral element	15
5	Sample Gauss-Lobatto-Legendre (GLL) interpolants and shape function	17
6	Types of interfaces: (a) conforming. (b) p-type nonconforming. (c) h-type type nonconforming	22
7	Selection of active and passive faces at (a) a p-type nonconforming interface using maximum and minimum rules, and (b) an h-type nonconforming interface using long and short rules	23
8	An element with $N_x = N_y = 3^{rd}$ order expansion and $ncp = 16$ collocation points	25
9	CAM: (a) Original element with $ncp = 16$. (b) Constrained element with $\widehat{ncp} = \widehat{18}$	26
10	Graphical interpretation of how pointwise projection of CAM works at a p-type interface	27
11	Graphical interpretation of how pointwise projection of CAM works at an h-type interface	29
12	MEM: (a) Original element with $ncp = 16$. (b) Constrained element with $\widehat{ncp} = \widehat{19}$	32
13	Details about how MEM works at a p-type interface	34

FIGURE Page

14 Details about how MEM works at an h-type interface 38

15 (a) Two-element and (b) three-element meshes to test p-type and h-type nonconformities. (c) Exact solution given by equation Eq. (4.3) 43

16 Spectral convergence obtained for Test 1 44

17 Convergence obtained for Test 2 45

18 Convergence curves obtained for Test 3 47

19 Convergence obtained for Test 4 48

20 Maximum eigenvalues for Test 5 50

21 Four-element meshes used in the convection tests 51

22 Eigenvalue spectrums for Test 6a (top) and 6b (bottom) 52

23 Maximum real part of the eigenvalues for Test 6b using maximum and minimum rules 54

24 Eigenvalue spectrums for Test 7a (top) and 7b (bottom) 55

25 Maximum real parts of the eigenvalues for Test 7b using CAM and MEM 56

26 Initial condition for the convection problem, $\theta_0 = sin(2\pi x)sin(\pi y)$ . . 58

27 Time history of the error for Test 8 58

28 Time history of the error for Test 9 59

29 Time history of the error for Test 10 60

30 Time history of the error for Test 11 63

31 A typical semi staggered grid element 69

32 Convergence results for the solution of the oscillatory flow in a channel 75

FIGURE Page

33 Streamlines for the exact solution of the Kovasznay flow and two-different meshes used for the Kovasznay problem 76

34 Convergence results for different solutions of the Kovasznay flow . . . 77

35 Lid-driven cavity problem 78

36 Meshes used and u-velcoity contours obtained for the lid-driven cavity problem at $Re = 500$ 79

37 The geometry and thermal boundary conditions used for the oscillatory flow forced convection problem 85

38 Schematic view of a hypothetical problem that consists of a channel with repeating heated and constant temperature boundaries . . . 85

39 Analytical solution of the velocity profiles at various times during a cycle for (a) $\alpha = 1$, (b) $\alpha = 10$ flow 90

40 A typical mesh used for the solution of the heat transfer problem that takes advantage of h- and p-type nonconforming elements, as well as anisotropic expansions (elements with $N_x \neq N_y$). 91

41 Instantaneous temperature contours for cases 2, 4, 6 and 8 93

42 Instantaneous temperature and velocity profiles at axial locations of $x = 5$ (solid-lines) and $x = 10$ (dashed-lines) 96

43 Instantaneous top-wall temperatures 97

44 Time-averaged wall-temperature (solid lines) and time-averaged bulk temperature (dashed-lines) variations for reciprocating flows . . 99

45 Axial distribution of time-averaged Nusselt number for (a) reciprocating, (b) unidirectional steady flows 101

CHAPTER I

INTRODUCTION

A. Background

1. Spectral and Spectral Element Methods

Spectral Methods (SM) are generally considered as a sub-category of Method of Weighted Residuals (MWR) [1]. A typical MWR formulation for solving a partial differential equation includes the following steps:

Step 1. Put the partial differential equation into a residual form and equate it to zero

$$\mathcal{R} = 0$$

Step 2. Represent the unknowns by a truncated series expansion

$$u(x) \approx u_N(x) = \sum_{i=0}^{N} \hat{u}_i S_i$$

where N is the order of the approximation, S_i are the approximation (trial, basis, shape) functions and $\hat{u}_i$ are the unknown coefficients. This step will yield to an approximated residual

$$\mathcal{R}_{\mathcal{N}} \approx 0$$

Step 3. Equate the weighted integral of this approximated residual to zero.

$$\int_{x_0}^{x_1} \mathcal{R}_{\mathcal{N}} \; w \; dx = 0$$

where w is the weight (test) function.

Step 4. By selecting different weight functions for each unknown, form a

---

The journal model is *IEEE Transactions on Automatic Control.*

$(N+1)*(N+1)$ set of algebraic equations and solve for the unknown coefficients $\hat{u}_i$.

Spectral Methods provide global approximations, i.e. the truncated series approximation given in the second step covers the whole problem domain. Depending on the choice of weight functions, one can end up with one of the three commonly used techniques: collocation, Galerkin and Tau methods. In the collocation (pseudospectral) method, weight functions are Dirac delta functions based on a set of collocation points. This method forces the residual to be exactly zero at the collocation points. Collocation method is sometimes referred as the nodal method, because it calculates the unknowns at the nodes of the physical space. Collocation method formulates the non-linearities very easily but it suffers from aliasing errors [2]. Galerkin formulation is the case where the weight functions are selected to be the same as the approximation functions. Weight functions cover the whole domain and satisfy the boundary conditions. Tau method is a slightly different version of the Galerkin method, where the weight functions do not necessarily satisfy the boundary conditions. Instead, boundary conditions are enforced by a separate set of constraints. In Galerkin and Tau methods the unknowns are just the coefficients of a series expansion that are not in the physical space and therefore these methods are sometimes referred as modal methods.

Choice of the approximation functions provide another categorization of the Spectral Methods. Commonly used functions are trigonometric polynomials, Chebyshev polynomials and Legendre polynomials. The use of trigoneometric polynomials is known as the Fourier Spectral Method [3]. It is mostly used with periodic boundary conditions, such as the simulation of three-dimensional homogeneous turbulence in simple domains. Chebyshev and Legendre polynomials belong to the family of Jacobi polynomials, which are the eigenfunctions of singular Sturm-Liouville problems

[1]. Chebyshev polynomials can also be interpreted as a Fourier cosine expansion with a change of variable. All these three types of polynomials provide spectral accuracy (exponential convergence with increased order of approximation) for smooth (C^∞) solutions. Thus SM is the preferred solution technique for problems where high resolution is required.

One big disadvantage of SMs is that they provide global approximations and therefore are not suitable for complex domains. Problems with arbitrarily shaped boundaries can be solved with domain discretization methods, such as the Finite Element Method (FEM) [4]. FEM introduces a new domain discretization step to our summary of MWR formulation. In this step the problem domain is subdivided into simple elements (sub-domains), such as triangles, quadrilaterals, tetrahedrals, etc. Complexity of the domain is no longer a problem, because one can arrange these elements of different shapes and sizes in any desired way. Unlike SMs, test and trial functions used in FEM are local, i.e. they are defined on each element separately. Another step used in FEM is the global assembly, where the local set of equations, written individually for each element are assembled by a direct-stiffness-summation procedure. The locality of the test and trial functions results in a sparse global system of equations, which is advantageous in regards to computational resources.

FEM is first designed and used as a low-order approximation for the analysis of structural problems. Still today, many FEM codes use first or second order polynomial approximations. For many fluid flow problems, which require high resolution and accuracy, this is a major limitation. One alternative is provided by the Spectral Element Method (SEM), which combines the competitive advantages of Spectral and Finite Element Methods [5]. Similar to FEM it discretizes the domain into elements but not as many or as fine as utilized in a typical finite element mesh. On these small number of elements SEM uses high order Chebshev or Legendre polynomials to

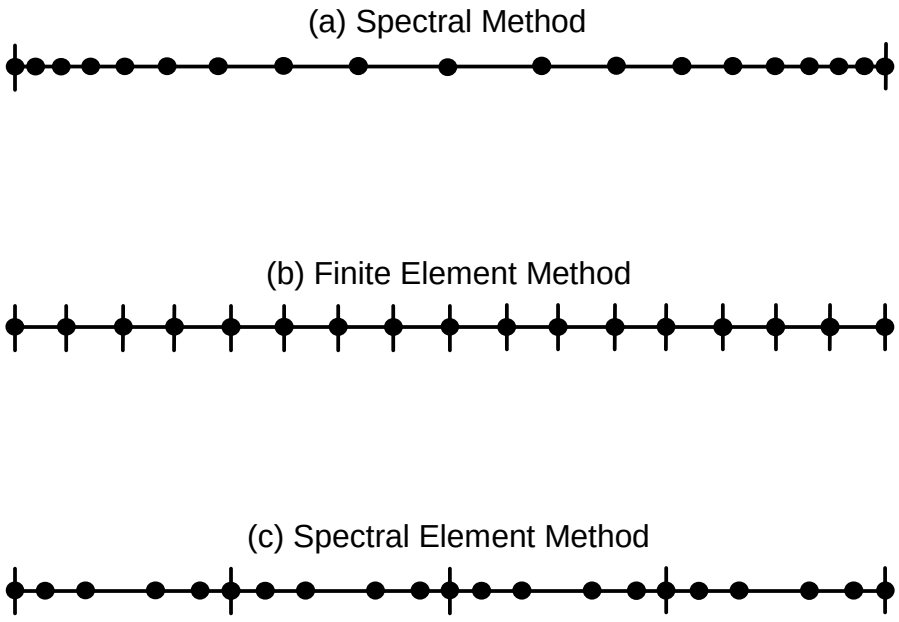

Fig. 1. Domain and element discretization of a one-dimansional problem. Vertical lines show element boundaries. Circles show collocation points. (a) SM uses a single element approximated with very high order polynomial expansions (b) FEM uses many small elements with low order approximations. (c) SEM uses larger elements with higher order approximations.

achieve high accuracy. A visual comparison of the discretization of a one-dimensional domain with different methods are shown in Fig 1. In SEM codes, polynomial orders of 6-12 are typically used. SEM is first designed for the solution of incompressible Navier-Stokes equations. Similar to Spectral Methods, SEM applications are still mostly fluid flow oriented.

The most important advantage of high order methods (SM and SEM), compared to low order ones (FEM) is the higher accuracy they provide. Another advantage of high-order methods is that they are memory minimizing [3], which is the reason why they are preferred for computationally demanding meteorology problems. However, compared to low-order methods, they require more computations per degree of freedom. Also they suffer more from the geometric singularities such as corners or

discontinuities inherent in the solution such as shock waves.

2. Nonconforming Formulations

In numerical simulations, local (non-propagating) mesh refinement is a key requirement for efficient and accurate solvers. For example in the typical test case of flow over a cylinder, the thin boundary layer around the cylinder and the wake behind it are the regions where most flow physics happens. Therefore these regions need to be resolved better than the inflow or far field regions. Another example is the lid-driven cavity problem, where finer elements are required near the corners in order to properly confine the geometric singularities. If one has a priori idea of what the solution will be, the simulation can be performed with a properly refined mesh. But usually adaptive strategies are required, where the mesh is refined continuously during the solution process, according to the error estimations. For time dependent problems, such as a travelling wave, adaptive strategies are necessary in order to capture the moving gradients properly.

In domain decomposition methods, three types of refinement strategies are used when more accuracy is needed. These are summarized in Fig. 2, where a four element mesh is refined in order to resolve the sharp gradients in the upper right corner of the domain. The most basic technique is to use smaller size elements in the regions where higher resolution is required. This is called h-type refinement because the element sizes, which are usually denoted by h, are changed. Number of elements is increased, but approximation orders inside the elements are kept the same. As seen in Fig. 2 this may result in elements which are not geometrically conforming. By geometrical nonconformity we mean the situation where the intersection of neighboring elements are not a whole face or a vertex. In this study for geometrical nonconformity we use the term h-type nonconformity because it is usually generated by an h-type refinement.

Second type of refinement is the p-type refinement. In this case the number of elements and their sizes are kept the same but the approximation order inside the elements, where higher resolution is required, is increased. This type of refinement results in polynomial order nonconformity, which is called p-type nonconformity. This is the case, where the interfaces of the neighboring elements match geometrically but the unknowns defined on those faces do not match.

Third type of refinement is the r-type refinement, which keeps the number of elements and their approximation orders the same but changes the shapes and the distribution of them. It moves the elements closer to the locations, where more resolution is required. Although sounds simple, this is the most difficult of all three refinement strategies due to the requirement of clever relocating algorithms. It is also limited in the sense that too much mesh movement may result in too distorted elements, in which case, remeshing might be necessary. It is useful in case of discontinuous solutions and used effectively for shock capturing in compressible flows. r-type refinement does not result in any type of nonconformities and is not covered in this study. Note that mesh coarsening is the opposite of refinement and the discussion about refinement equally applies to it. In adaptive simulations, mesh refinement and coarsening are usually used together.

Both h- and p-type nonconformities require special treatment, because nonmatching unknowns at nonconforming interfaces can not simply be assembled. There are several techniques to formulate these nonconformities. Constrained Approximation Method (CAM) is one of the very early ones and is very simple in theory [6]. It is based on the interpolation of unknowns at nonconforming interfaces and provides a pointwise projection. CAM is popular in the Finite Element community and usually used with low-order methods. Mortar Element Method (MEM) is another technique, in which the jump accross nonconforming interfaces are minimized in a

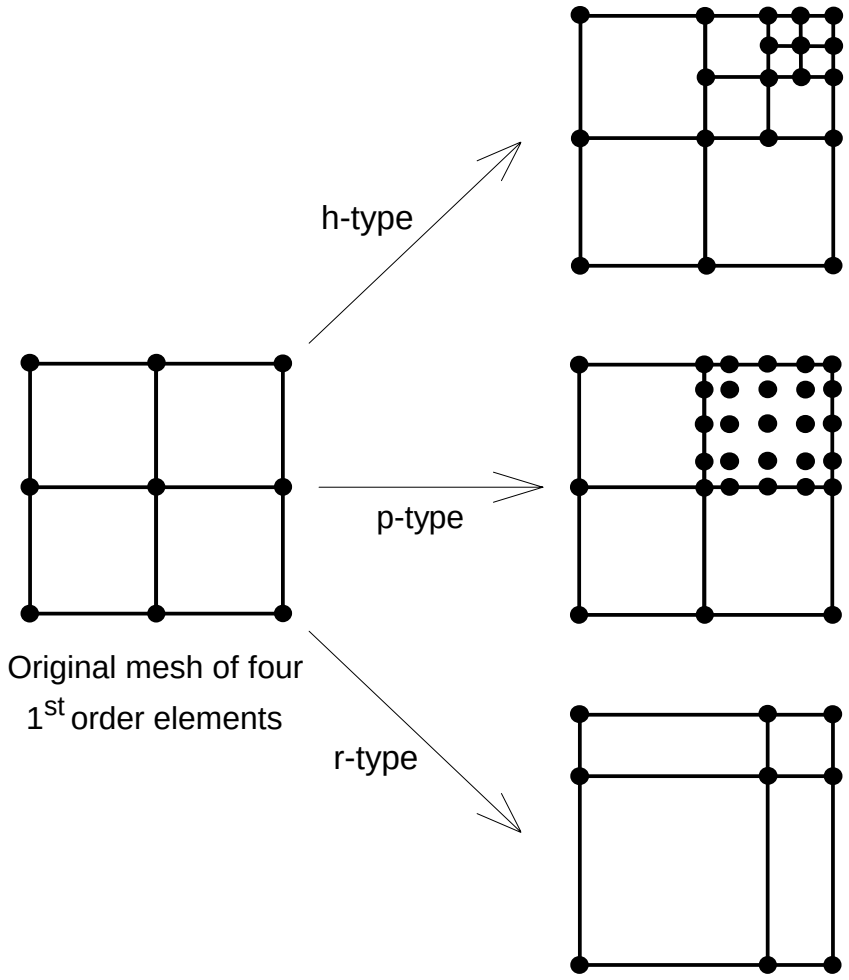

Fig. 2. Three commonly used refinemet strategies. Lines show element boundaries, circles show collocation points. (a) h-type refinement keeps the approximation orders the same but introduces new elements. (b) p-type refinement keeps number of elements the same but increases the approximation order. (c) r-type refinement keeps both the number of elements and approximation order in each element the same, but resize and relocate the elements.

weighted integral sense. It is first developed by the Spectral Element community and today it is mostly used in spectral solvers [7]. There are other formulations to handle nonconformities but in this study we will study CAM and MEM in detail.

Before finishing this section, it is important to note that Spectral Element Method is usually compared with p-type Finite Element Method (pFEM), which is an extension to the classical FEM, providing p-type refinements [8]. The main difference between pFEM and SEM lies in the choice of the trial and test functions. In pFEM case, hierarchical polynomials based on an equispaced elemental discretization are used as basis functions. In SEM, on the other hand, the basis in each element are formed using the Lagrange interpolants at the the Gauss-Lobatto quadrature points.

B. Literature Survey

Although mathematical background of global approximations, such as the Fourier expansion, goes back much earlier, the first practical use of Spectral Methods started in the beginning of 1970s. Earliest spectral Galerkin applications were given by Orszag [9]. He was also among the first to use the spectral collocation method [10]. A review of the fluid flow applications can be found in [11]. There are many excellent textbooks devoted to Spectral Methods. One of the pioneering work is the monograph by Gottlieb and Orszag [12], which provides the foundation of the modern SM. This study is than followed by many others such as Canuto et al. [1] which focuses on fluid mechanics applications. Boyd [3] discusses Fourier and Chebyshev methods in great detail. A more recent book by Peyret [13] concentrates on incompressible viscous flows.

The Spectral Element Method is first presented by Patera [5] for the solution of Navier-Stokes equations. Korczak and Patera [14] provided the foundations of the

iso-parametric SEM . More recent examples were given by Maday and Patera [15]. Spectral element multigrid formulations can be found in Ronquist and Patera [16]. Parallel applications are provided by Fischer [17]. A recent review of incompressible flow applications is given by Karniadakis and Henderson [18]. The book by Karniadakis and Sherwin [19] presents the spectral element formulations for unstructured elements and provides many large scale applications of the Navier-Stokes equations.

Nonconforming formulations goes back as early as the Finite Element Method. One of the earliest studies of the Constrained Approximation Method is given by Tsai and Szabo as an extension to FEM. [20]. A similar approach, called the transition element method, applied to low order elements is discussed in [21]. A recent and more complete discussion of CAM can be found in a series of papers by Demkowicz et al. [6] and Rachowicz and Demkowicz [22]. An hp adaptive strategy coupled with CAM is given by Ainsworth and Senior [23]. One of the few number of CAM and SEM combinations can be found in [24]. Zanolli patching technique, introduced by Funaro et al. [25], is an iterative procedure where Dirichlet and Neumann boundary conditions are imposed on the opposing sides of the nonconforming interface. Later the technique is modified by Henderson and Kardiadakis [26]. Mortar Element Method is introduced by Patera and his associates [7, 27]. A comparison of Zanolli patching and MEM can be found in [28]. One of the few number of papers studying CAM and MEM together is given by Ronquist [29]. Mavriplis [30] and Henderson [31] studied the adaptive refinement strategies using MEM. Finally, a modified version of MEM, called the FETI method, is discussed in [32]. As observed from these references, CAM is mostly used with low-order formulations, and MEM is preferred for high-order ones. This makes it quite difficult to find comparasions of these two techniques, which we intend to provide in this study.

C. Specific Objectives

In this study we are focusing on two different nonconforming extensions to the classical Galerkin Spectral Element formulation, namely the Constrained Approximation Method and the Mortar Element Method. The following are our specific objectives

- Setup a consistent terminology for h- and p-type nonconformities.
- Provide visual descriptions and step by step formulations of CAM and MEM, for easy comparisons.
- Study and compare the stability and consistency characteristics of CAM and MEM using advection and diffusion operators.
- Develop efficient Stokes and Navier-Stokes solvers that can use nonconforming formulations and validate them using test problems.
- Utilize the developed solvers in engineering applications, such as the analysis of oscillatory flow forced convection heat transfer in two-dimensional channels.

D. Organization of Thesis

In Chapter II, we review the conforming Galerkin spectral element formulation. In Chapter III, this formulation is extended to cover nonconforming elements using CAM and MEM. These two nonconforming formulations are tested in Chapter IV, using diffusion and advection operators. Chapter V provides formulations for Stokes and Navier-Stokes equations and validates them using test problems. Chapter VI demonstrates use of these new solvers for a detailed parametric study of oscillatory flow forced convection heat transfer. Finally, a summary of our work and recommendations for future studies are provided in Chapter VII.

E. Nomenclature

A	Convection matrix, pressure gradient amplitude.
C	Conformity matrix.
c_p	Specific heat at constant pressure.
D	Diffusion matrix.
f, F	Known force function and force vector.
H	Channel height.
k	Heat conduction coefficient.
K	Stiffness matrix.
L	Gauss Lobatto Legendre interpolant, total channel length.
L_p	Penetration length.
L_h	Heated channel length.
M	Mass matrix.
N	Polynomial expansion order.
Nu	Nusselt number.
p	Pressure.
Pe	Peclet number.
Pr	Prandtl number.
q	Heat flux.
Re	Reynolds number.
Re'	Reynolds number based on volumetric flowrate per channel width.
S	Two-dimensional shape function, pressure matrix.
t	Time.
T	Temperature.
u, v	Velocity components.
x, y	Cartesian coordinates.

Greek symbols:

- α Diffusivity, Womersley number.
- Γ Domain boundary.
- λ Eigenvalue.
- ξ, η Local coordinates of the master element.
- ν Kinematic viscosity.
- ρ Density, Gaussian integration weights.
- θ General scalar unknown.
- τ Period.
- ω Weight function, frequency.
- Ω Domain.

Subscripts and superscripts:

- b Bulk quantity.
- e Elemental.
- o Reference value, side-wall value.
- $\dot{}$ Time derivative.
- $\hat{}$ Related to the original element.
- $\tilde{}$ Related to the Gauss Lobatto points.
- $\bar{}$ Time-averaged quantity.
- $\overline{\overline{}}$ Time and space averaged quantity.
- * Dimensional quantity.

CHAPTER II

CONFORMING GALERKIN SPECTRAL ELEMENT FORMULATION

In this chapter, we present a Conforming Galerkin Spectral Element Formulation, to form the basis for the non-conforming extensions, which will be studied in the next chapter. We will first consider a steady two-dimensional Poisson problem, starting from its strong form and work step-by-step all the way to the final algebraic matrix form. Then the semi-discrete formulation will be presented which can be used to solve time dependent problems.

A. Steady Formulation

Step 1 - Strong Formulation: For a steady two-dimensional Poisson problem, strong form is expressed as, find θ such that

$$-\nabla^2\theta = f \quad \text{on } \Omega \tag{2.1a}$$

$$\theta = g \quad \text{on } \Gamma_g \tag{2.1b}$$

$$\mathbf{n}\cdot\nabla u = h \quad \text{on } \Gamma_h \tag{2.1c}$$

where θ is the scalar unknown. Ω is the domain of the problem and $\Gamma = \Gamma_g \bigcup \Gamma_h$ is the boundary of Ω (Fig. 3a). Eqs. (2.1b) and (2.1c) are the essential and natural boundary conditions, respectively. The unit normal $\mathbf{n}$, points outward from boundary Γ, and f, g and h are known functions of the space coordinates.

Step 2 - Weighted Residual Formulation: Define the "residual" of Eq. (2.1a) as

$$\mathcal{R} = -\nabla^2\theta - f \tag{2.2}$$

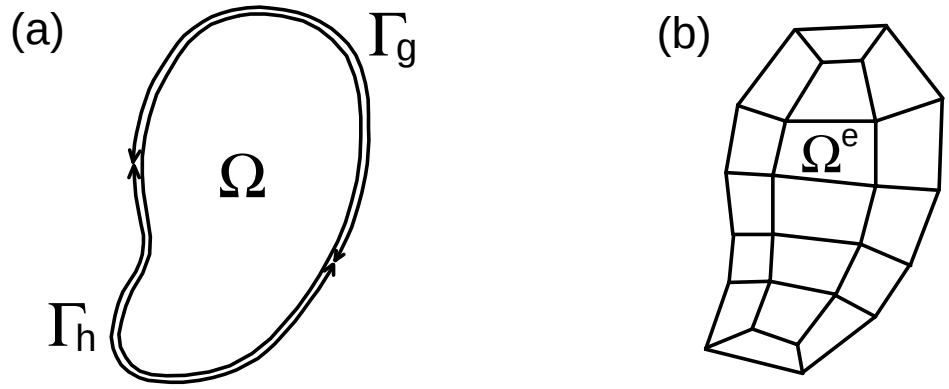

Fig. 3. Model problem. (a) Domain and boundary, (b) Domain discretization

In order to end up with a well defined algebraic set of equations (number of unknowns being equal to the number of equations) we force the approximate solution to satisfy the residual equation in a "weighted" integral sense

$$\int_\Omega \mathcal{R}w \; d\Omega \quad = \quad \int_\Omega (-\nabla^2\theta - f) \; w \; d\Omega = 0 \tag{2.3}$$

where the approximate solution θ and the weight function w belong to the following Hilbert spaces

$$\mathcal{L} = \{\theta : \theta \in H^1(\Omega), \; \theta = g \text{ on } \Gamma_g\}$$

$$\mathcal{V} = \{w : w \in H^1(\Omega), \; w = 0 \text{ on } \Gamma_g\}$$

Step 3 - Weak Formulation: In order to balance the order of differentiation between the approximation and weight functions, we apply integration by parts to the first term of Eq. (2.3)

$$\int_\Omega \nabla\theta \cdot \nabla w \; d\Omega = \int_\Omega f w \; d\Omega + \oint_{\Gamma_h} hw \; ds \tag{2.4}$$

Step 4 - Domain Discretization: Divide domain Ω into conforming subdomains (elements) Ω^e and apply the weak formulation in each subdomain individually

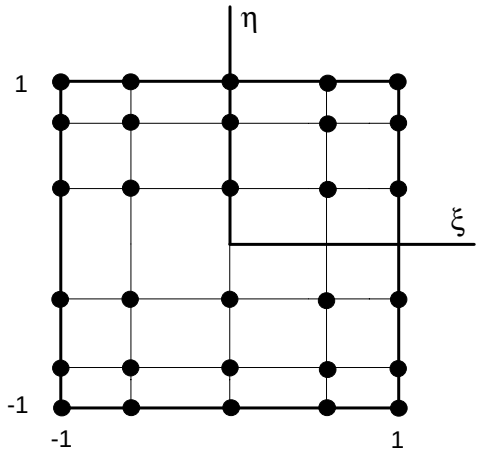

Fig. 4. Element discretization for a typical two-dimensional quadrilateral element. A 4×5 discretization yields 30 collocation points.

$$\int_{\Omega^e} \nabla\theta^e \cdot \nabla w^e \; d\Omega^e = \int_{\Omega^e} f^e w^e \; d\Omega^e + \oint_{\Gamma_h^e} h^e w^e \; ds^e \tag{2.5}$$

Figure 3b shows a sample discretization with quadrilateral elements.

Step 5 - Element Discretization: Map each element to a master element in (ξ, η) coordinate system and discretize further by introducing a set of collocation points (Fig. 4). The discretized form of θ can be written as

$$\theta(\xi, \eta) = \sum_{m=0}^{M} \sum_{n=0}^{N} \theta_{mn}^e \; L_M(\xi_m) \; L_N(\eta_n) \tag{2.6}$$

where $L_M(\xi_m)$ is the value of the M^{th} order Gauss-Lobatto-Legendre (GLL) interpolant at the m^{th} point in ξ direction. It is defined as

$$L_M(\xi_m) = -\frac{(1-\xi^2)P_M'(\xi)}{M(M+1)P_M(\xi_m)(\xi - \xi_m)} \; , \qquad m \in [0, M] \tag{2.7}$$

where P_M and P_M' are the M^{th}-order Legendre polynomial and its derivative, respectively. GLL collocation points are defined implicitly as

$$(1-\xi_m^2)L_M^{'}(\xi_m)=0 \tag{2.8}$$

By combining the two interpolants in Eq. (2.6) in a single shape function

$$S_j(\xi,\eta)=L_M(\xi_m)\ L_N(\eta_n)\ , \qquad j\in[1,ncp] \tag{2.9}$$

Eq. (2.6) can be simplified to

$$\theta(\xi,\eta)=\sum_{j=1}^{ncp}\theta_j^e\ S_j(\xi,\eta) \tag{2.10}$$

where $ncp=(M+1)(N+1)$ is the number of collocation points in element e. S_j is the two-dimensional shape function associated with the collocation point j, which is the tensor product of one-dimensional interpolants [19]. Sample GLL interpolants and the shape function obtained by their product are given in Fig. 5. Note that another common choice for element discretization is the Chebyshev points [3]. Although they provide similar accuracy, GLL points are known to have advantages in terms of computational efficiency, since they are orthogonal with respect to a unity weight function [33].

Step 6 - Weight Function Selection: In the Galerkin formulation weight function w in Eq. (2.5) is selected to be the same as the shape functions used for the unknown

$$w=S_i\ , \qquad i\in[1,ncp] \tag{2.11}$$

Step 7 - Elemental Matrix Form: Substitute Eqs. (2.10) and (2.11) into Eq. (2.5) to obtain

$$\int_{\Omega^e}\sum_{j=1}^{ncp}\theta_j^e\ \nabla S_j\cdot\nabla S_i\ d\Omega^e=\int_{\Omega^e}f^eS_i\ d\Omega^e+\oint_{\Gamma_h^e}h^eS_i\ ds^e \tag{2.12}$$

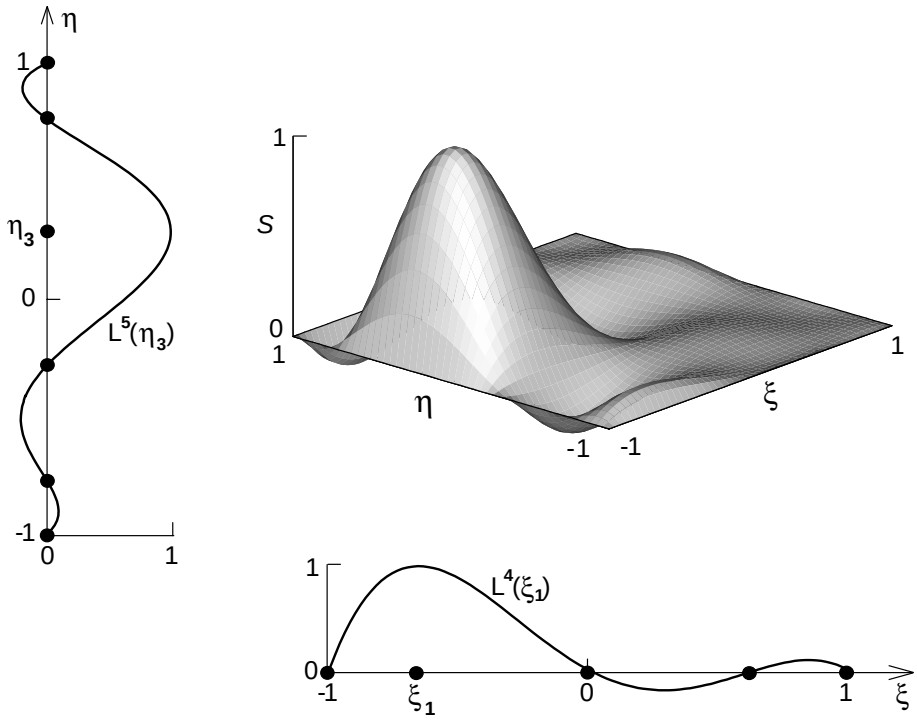

Fig. 5. Sample Gauss-Lobatto-Legendre (GLL) interpolants and shape function

which can be put into the following elemental matrix form

$$[K]^e\{\theta\}^e = \{F\}^e = \{f\}^e + \{Q\}^e \tag{2.13}$$

where $[K]^e$ is the elemental stiffness matrix given by

$$K^e_{ij} = \int_{\Omega^e} \nabla S_j \cdot \nabla S_i \; d\Omega^e \; , \qquad i,j \in [1, ncp] \tag{2.14}$$

and $\{F\}^e$ is the elemental force vector which includes the contribution from the actual forcing function $\{f\}^e$, as well as the contribution from the natural boundary conditions $\{Q\}^e$. It is given by

$$F^e_i = \int_{\Omega^e} f^e S_i \; d\Omega^e + \oint_{\Gamma^e_h} h^e S_i \; ds^e \; , \qquad i \in [1, ncp] \tag{2.15}$$

Step 8 - Numerical Integration: For a robust and problem-independent imple-

mentation, the integrals in Eqs. (2.14) and (2.15) need to be evaluated numerically. One obvious choice is to use the already available GLL points, given by Eq. (2.8), and corresponding integration weights. Numerical integration will convert the integrals to summations

$$K_{ij}^{e} = \sum_{k=1}^{ncp} \nabla S_j \cdot \nabla S_i \ \rho_k \tag{2.16}$$

$$F_{i}^{e} = \sum_{k=1}^{ncp} f^e S_i \ \rho_k + \sum_{k=1}^{nfp} h^e S_i \ \rho_k \tag{2.17}$$

where ncp is the number of collocation points of element e and nfp is the number of collocation points at the boundaries with natural boundary condition. Above, ρ_k are the GLL integration weights. Note that the differential operator ∇ in Eq. (2.16) acts on the real coordinates (x, y) and need to be converted to a corresponding operator acting on the local coordinates (ξ, η) of the master element. This requires evaluation of the Jacobian matrix, details of which can be found in [4].

Step 9 - Assembly and Matrix Form: After repeating steps 8 and 9 for all the elements, the global system can be assembled as

$$[K] = \sum_{e=1}^{ne}{}' [K]^e \ , \qquad \{F\} = \sum_{e=1}^{ne}{}' \{F\}^e \tag{2.18}$$

which yields the following final set of algebraic equations

$$[K]\{\theta\} = \{F\} \tag{2.19}$$

It is worth here to note that conformity between the element interfaces is implicitly used during the assembly process. That is there is a one to one matching between the unknowns of the elements sharing an interface and these matching points contribute to the same entry of the global matrix. However, as we will see in the next

section, in case of nonconforming elements a modified assembly process is required.

B. Semi-discrete Formulation

Let's extend the formulation presented in the previous section, to include time derivatives. The unsteady Poisson problem is given as

$$\frac{\partial \theta}{\partial t} - \nabla^2 \theta = f \tag{2.20}$$

Using the boundary conditions given in Eq. (2.1) and a proper initial condition, will yield to the following weak form

$$\int_\Omega (\frac{\partial \theta}{\partial t} w + \nabla \theta \cdot \nabla w) \; d\Omega = \int_\Omega f w \; d\Omega + \oint_{\Gamma_h} h w \; ds \tag{2.21}$$

Element discretization still involves only spatial variation. In other words, shape functions, given in Eq. (2.9) that are functions of ξ and η will be used. Discretized unknown is given as

$$\theta(\xi, \eta, t) = \sum_{j=1}^{ncp} \theta_j^e(t) \; S_j(\xi, \eta) \tag{2.22}$$

where the time variation is separated from the space variation.

Similar to the steady formulation, one can still use weight functions w to be the same as shape functions S, as given in Eq. (2.11). Substituting Eqs. (2.11) and (2.22) into Eq. (2.21) will give

$$\int_{\Omega^e} \sum_{j=1}^{ncp} \frac{\partial \theta_j^e}{\partial t} S_j \; S_i \; d\Omega^e + \int_{\Omega^e} \sum_{j=1}^{ncp} \theta_j^e \; \nabla S_j \cdot \nabla S_i \; d\Omega^e = \int_{\Omega^e} f^e S_i \; d\Omega^e + \oint_{\Gamma_h^e} h^e S_i \; ds^e \tag{2.23}$$

which can be put into the following elemental matrix form

$$[M]^e \{\dot{\theta}\}^e + [K]^e \{\theta\}^e = \{F\}^e \tag{2.24}$$

where $\dot{\theta}$ represents the time derivative of the approximation. The elemental stiffness matrix $[K]^e$ and the elemental force vector $\{F\}$ are given in Eqs. (2.14) and (2.15), respectively. $[M]^e$ is the elemental mass matrix, given by

$$M_{ij}^e = \int_{\Omega^e} S_i S_j \, d\Omega^e \tag{2.25}$$

Next step is the numerical evaluation of the integrals in elemental matrices and vectors, and assemble them into the following set of algebraic equations

$$[M]\{\dot{\theta}\} + [K]\{\theta\} = \{F\} \ , \qquad i, j \in [1, ncp] \tag{2.26}$$

Semi-discrete formulation continues by approximating the time derivative of the unknown $\dot{\theta}$ in terms of unknowns at various time steps. At this point it is important to note that the mass matrix, obtained after the numerical integration of Eq. (2.25) is diagonal. This is because of the fact that the collocation points used for numerical integration, and the points at which the shape functions are evaluated, are the same. This is an important property of spectral element methods, which is not found in classical finite element formulations [4]. Unfortunately, this property will be lost when the Galerkin formulation is modified with nonconforming formulations [28].

CHAPTER III

NONCONFORMING FORMULATIONS, CAM AND MEM

In this chapter we present details of the Constrained Approximation Method (CAM) and the Mortar Element Method (MEM). In the coming sections, we demonstrate the principles of both techniques on p-type and h-type nonconforming interfaces. Each method is studied sequentially using step by step instructions, which enables a better comparison between them.

A. Definitions About Nonconformities

First, we will provide several definitions that will be used in the coming sections. Some of them are first introduced to the literature in this study. We will start with the definitions of interfaces. We will distinguish three types of interfaces, conforming, p-type nonconforming and h-type nonconforming. Samples can be seen in Fig. 6. A *conforming interface* has two geometrically matching faces, with the same order of expansion used at each face. It results in matching collocation points. A *p-type nonconforming interface* has two geometrically matching faces, but different orders of expansion is used in each element. An *h-type nonconforming interface* has geometrically non-matching faces. The most popular one is shown in Fig. 6c, which is known as *1-irregular interface*. It is the only kind of h-type nonconforming interface used in this study. It is shared by one *long element* and two *short elements*. There is just one *hanging point*, which is the middle collocation point. The order of expansions at the three faces, sharing an h-type nonconforming interface, can be the same or different. As seen in Fig. 6 both p-type type and h-type nonconforming interfaces result in non-matching collocation points.

At a nonconforming interface one should decide on which face(s) to be con-

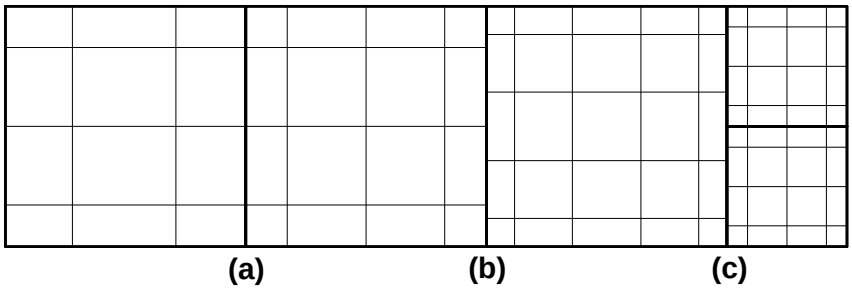

Fig. 6. Types of interfaces: (a) conforming. (b) p-type nonconforming. (c) h-type type nonconforming. Thick lines show element boundaries and intersection of thin lines show the collocation points.

strained. This depends on the selection of active and passive faces. A *passive face* is the one, the collocation points of which, will be replaced by the points of the corresponding *active face*. This is called *constraining a face*. Therefore not all the faces sharing a nonconforming interface are constrained. The selection of active and passive faces depend on the type of nonconformity and the formulation used (CAM or MEM).

At a p-type interface one can either use the *maximum rule*, which selects the face with higher expansion order as the active face, or the *minimum rule*, which is just the opposite. An example is given in Fig. 7a. The freedom of choosing between maximum and minimum rules is available for both CAM and MEM.

Selection of constrained faces at an h-type interface is different and depends on whether we use CAM or MEM. Maximum and minimum rules do not apply at an h-type interface, since the nonconformity is not related to the order of expansions. The nonconformity is related to the shapes of the elements and the selection of constrained faces is now determined by the long and short rules. The *long rule* selects the long face as the active face and the two short faces as passive faces. The *short rule* is just the opposite. In this study, for the reasons which will be discussed later in this chapter, at an h-type interface CAM and MEM can only use the long and short rules,

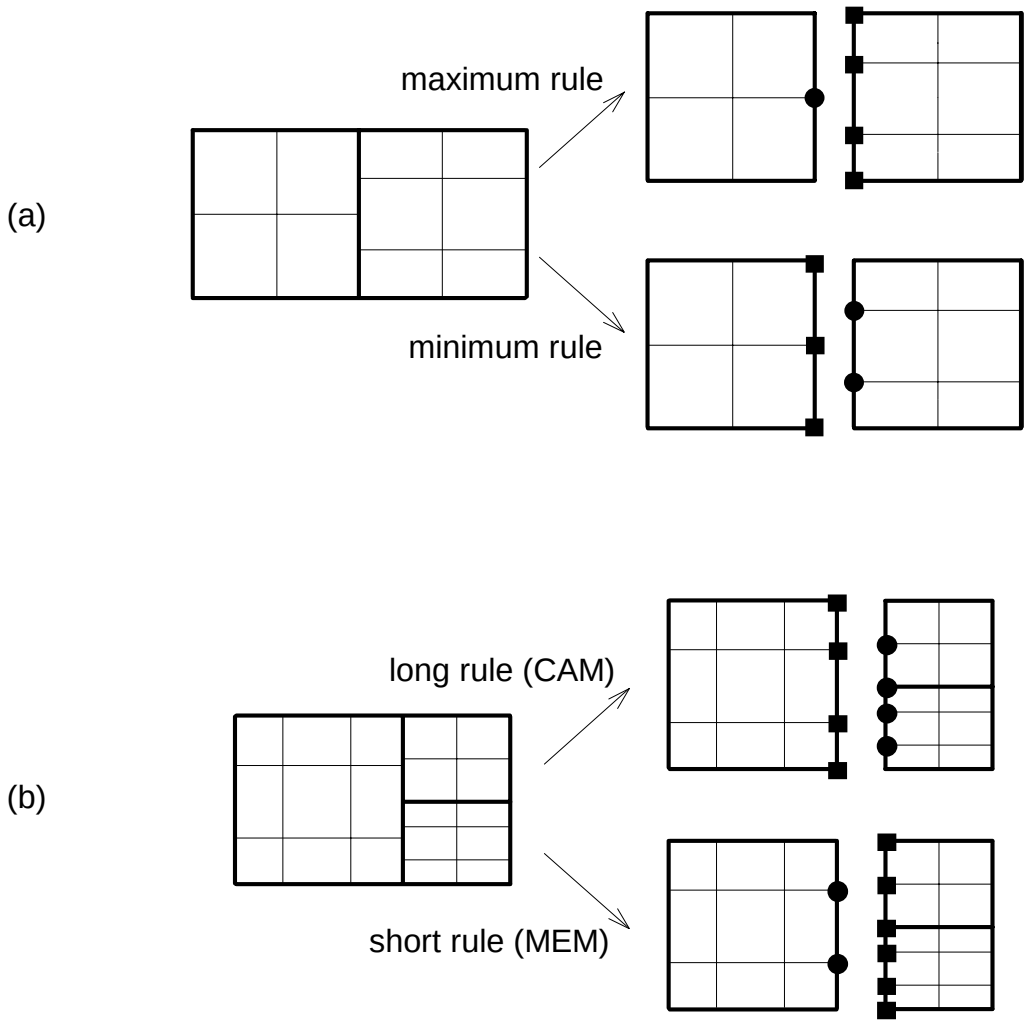

Fig. 7. Selection of active and passive faces at (a) a p-type nonconforming interface using maximum and minimum rules, and (b) an h-type nonconforming interface using long and short rules. Original configurations are the ones on the left of the arrows. Modified configurations on the right show the active points (squares) and passive points (circles), only at the interface.

respectively. Examples of long and short rules are given in Fig. 7b.

The collocation points of the modified configurations of Fig. 7 shown by squares are called the *active points*. The circles are called the *passive points*. As we will demonstrate shortly, CAM and MEM provide ways to express the unknowns at the passive points in terms of the ones at the active points. In other words, passive points are removed from the mesh and only the active points contribute to the global assembly process. Note that the corner points (end points of the faces), inner points (points that do not lie at a face) and points of a face that is not constrained are always active points.

B. Constrained Approximation Method (CAM)

As described in the previous section, at a non-conforming interface there is no one-to-one matching between the collocation points of the neighbor elements. This can also be viewed as the loss of continuity of the unknowns at the nonconforming interfaces. CAM is a method where we regain this lost C^0 continuity. This is done by a pointwise projection and matching of the unknowns of one face to the other. It is mostly used with the p-version of the finite element method [6, 22, 23], with very limited number applications to high-order spectral methods [24].

We will demonstrate this method using the configuration given at Fig. 8, which shows an element surrounded with five neighbors. We will concentrate on the shaded, middle element and study its interaction with its neighbors. In the expanded view of Fig. 8 only the faces of the neighbors' that are shared with the middle element are shown. Although the method is general and can use any combination of expansion orders, in this example we use 3^{rd} order expansions in both x and y directions. Local point numbering from 1 to 16 can be done in any way and different choices do not

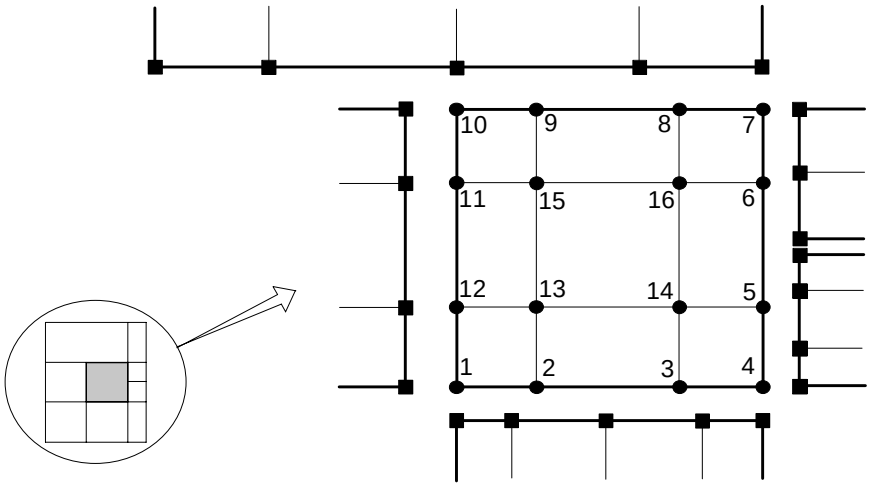

Fig. 8. An element with $N_x = N_y = 3^{rd}$ order expansion and $ncp = 16$ collocation points. Faces shared with five neighboring elements are also shown. South interface has p-type, East and North interfaces have h-type nonconformities. West interface is conforming. Points of the middle element and points of the neighbors are shown with circles and squares, respectively.

affect the following formulation.

Step 1 - Determine the nonconforming interfaces and type of nonconformities: In our example South interface has p-type, East and North interfaces have h-type nonconformities. West interface is conforming.

Step 2 - Decide on active and passive faces: At the nonconforming interfaces collocation points of two neighboring faces are not matching (circles are not matching with squares). Both set of points can not be used in the assembly process. A decision should be made on which set of points to be used. The points that will be used in the assembly process are the *active points* and remaining set of points are the *passive points*. Let's first concentrate on the South interface where we have p-type nonconformity. As discussed in the previous section, there are two possibilities in determining the active/passive faces: minimum and maximum rules. In this example maximum rule will be used. Now let's look at the East and North interfaces where we

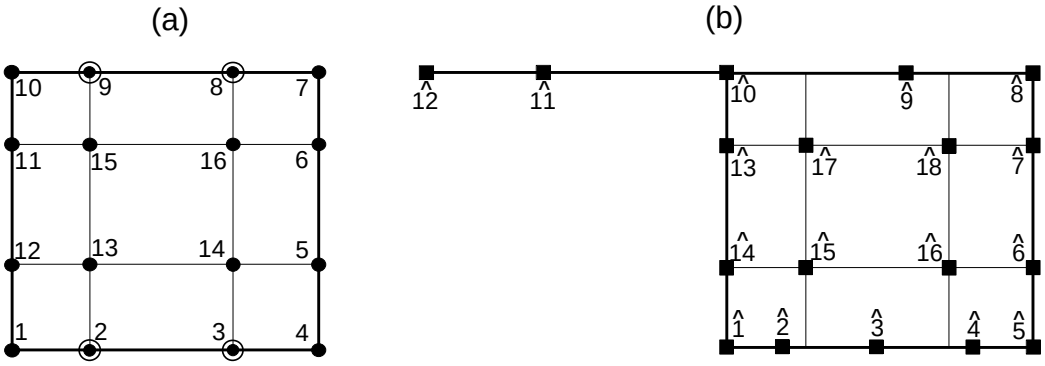

Fig. 9. CAM: (a) Original element with $ncp = 16$. (b) Constrained element with $\widehat{ncp} = \widehat{18}$. Passive points are shown with an extra circle around them. Active points are shown by squares.

have h-type nonconformity. At these interfaces there is only one choice: the long rule. East face is a long face, and therefore is active. That is, it will not be constrained. North face is a small face, and therefore is passive. It will be constrained. Later it will be clear why the other possibility, the *short rule* is not suitable for CAM. To summarize, we identified the South and the North faces to be passive, and West and East faces to be active.

Step 3 - Generate the modified element: Figure 9a shows the original element whose (according to the above discussion) South and North faces are passive. Figure 9b shows the modified element obtained by replacing the passive points of the original element by the points of the active neighboring faces. To make the discussion more clear, deleted points of the original element (2, 3, 8, 9) are the passive points (shown with an extra circle around them). By definition all the points of the modified element, shown as squares, are active points. These are the points that will go into the global assembly process. Points of the modified element are distinguished from that of the original element by a hat ($\widehat{\ }$) on them.

Step 4 - Write the unknowns at the passive points in terms of the unknowns at the

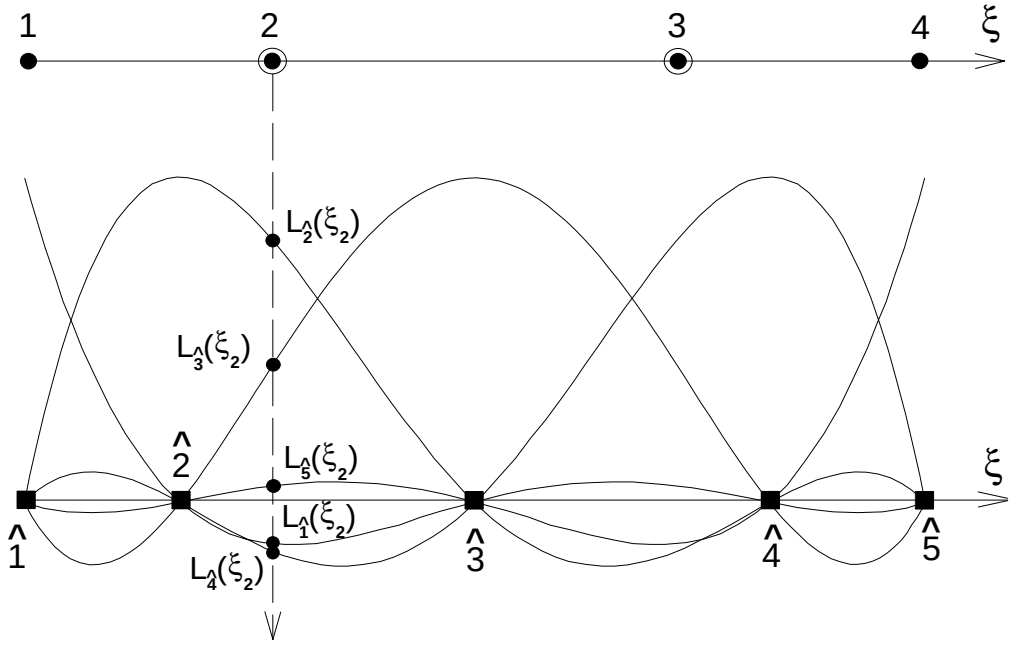

Fig. 10. Graphical interpretation of how pointwise projection of CAM works at a p-type interface

active points: This is the key step which is different for each nonconforming technique. CAM is one of the easiest ones, in which we enforce a projection of unknowns at the passive points onto the active faces.

Step 4a - Find the conformity equation for the South face: Let's start with the South face. The following formulation should be followed by referring to Fig. 10. We want to write the unknowns at the passive points 2 and 3 in terms of unknowns at the active points $\widehat{1},\ ...,\ \widehat{18}$. For this purpose, Eq. (2.10) can be used on the modified element. For example at point 2,

$$\theta_2 = \sum_{\widehat{j}=\widehat{1}}^{\widehat{ncp}} \theta_{\widehat{j}}^e \; S_{\widehat{j}}(\xi_2, \eta_2) \tag{3.1}$$

Note that point 2 is at a face where two-dimensional shape functions reduce to one-dimensional Lagrange interpolants (see Eq. (2.6)). Using this fact, Eq. (3.1) can

be simplified to

$$\theta_2^e = \theta_{\widehat{1}}^e L_{\widehat{1}}(\xi_2) + \theta_{\widehat{2}}^e L_{\widehat{2}}(\xi_2) + \theta_{\widehat{3}}^e L_{\widehat{3}}(\xi_2) + \theta_{\widehat{4}}^e L_{\widehat{4}}(\xi_2) + \theta_{\widehat{5}}^e L_{\widehat{5}}(\xi_2) \tag{3.2}$$

This is called the constrained approximation for the passive point 2. A similar equation can be written for point 3 and together they can be expressed in the following vector equation,

$$\begin{Bmatrix} \theta_2 \\ \theta_3 \end{Bmatrix}^e = \Big[C_S\Big]^e \begin{Bmatrix} \theta_{\widehat{1}} \\ \theta_{\widehat{2}} \\ \theta_{\widehat{3}} \\ \theta_{\widehat{4}} \\ \theta_{\widehat{5}} \end{Bmatrix}^e = \begin{bmatrix} L_{\widehat{1}}(\xi_2) & L_{\widehat{2}}(\xi_2) & L_{\widehat{3}}(\xi_2) & L_{\widehat{4}}(\xi_2) & L_{\widehat{5}}(\xi_2) \\ & & & & \\ L_{\widehat{1}}(\xi_3) & L_{\widehat{2}}(\xi_3) & L_{\widehat{3}}(\xi_3) & l_{\widehat{4}}(\xi_3) & L_{\widehat{5}}(\xi_3) \end{bmatrix}^e \begin{Bmatrix} \theta_{\widehat{1}} \\ \theta_{\widehat{2}} \\ \theta_{\widehat{3}} \\ \theta_{\widehat{4}} \\ \theta_{\widehat{5}} \end{Bmatrix}^e \tag{3.3}$$

where C_S is the conformity matrix for the South face.

Step 4b - Find the conformity equation for the North face: Following the above procedure an equation similar to Eq. (3.3) can be written for the passive points of the North face

$$\begin{Bmatrix} \theta_8 \\ \theta_9 \end{Bmatrix}^e = \Big[C_N\Big]^e \begin{Bmatrix} \theta_{\widehat{8}} \\ \theta_{\widehat{9}} \\ \theta_{\widehat{10}} \\ \theta_{\widehat{11}} \\ \theta_{\widehat{12}} \end{Bmatrix}^e = \begin{bmatrix} L_{\widehat{8}}(\xi_8^*) & L_{\widehat{9}}(\xi_8^*) & L_{\widehat{10}}(\xi_8^*) & L_{\widehat{11}}(\xi_8^*) & L_{\widehat{12}}(\xi_8^*) \\ & & & & \\ L_{\widehat{8}}(\xi_9^*) & L_{\widehat{9}}(\xi_9^*) & L_{\widehat{10}}(\xi_9^*) & L_{\widehat{11}}(\xi_9^*) & L_{\widehat{12}}(\xi_9^*) \end{bmatrix}^e \begin{Bmatrix} \theta_{\widehat{8}} \\ \theta_{\widehat{9}} \\ \theta_{\widehat{10}} \\ \theta_{\widehat{11}} \\ \theta_{\widehat{12}} \end{Bmatrix}^e \tag{3.4}$$

where the transformation

$$\xi_i^* = \frac{\xi_i - 1}{2}$$

is used in order to project the local coordinates of the North face of the original element onto the modified face properly (Fig. 11). This projection is necessary

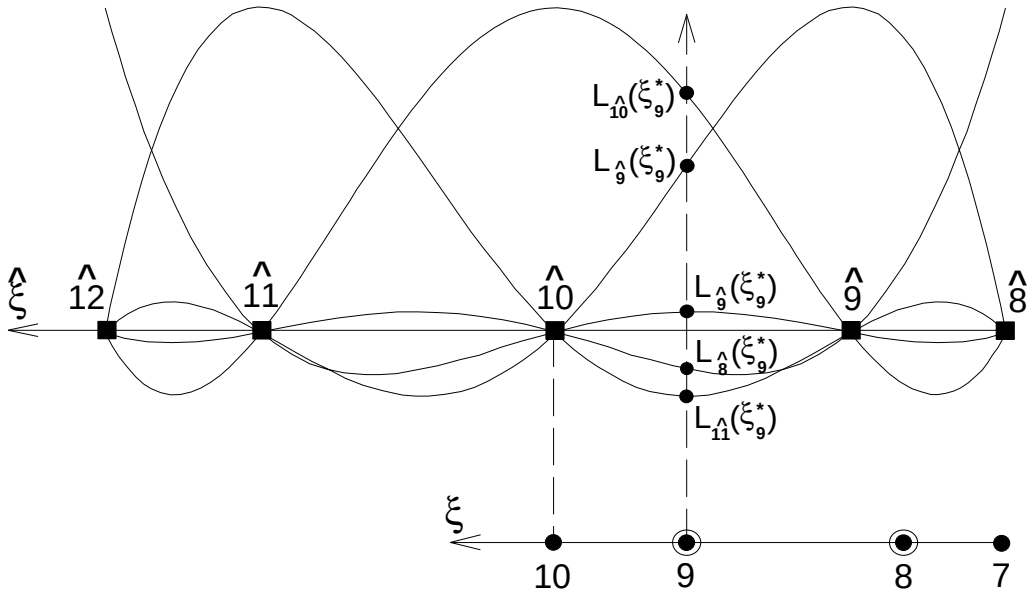

Fig. 11. Graphical interpretation of how pointwise projection of CAM works at an h-type interface

because in Eq. (3.4) Lagrange interpolants based on the modified face are evaluated at the collocation points of the original face, and the local coordinates of these two faces (ξ and $\widehat{\xi}$) do not match. It is also clear from Fig. 11 why the *short rule* is not suitable for CAM. Because that would require evaluation of Lagrange interpolants based on a short face at the collocation points of a long face, e.g. $L_9(\widehat{\xi}_{11})$, which is not defined (L_9 is only defined in $0 < \widehat{\xi} < 1$).

Now unknowns at all four passive points (2,3,8,9) are expressed in terms of the unknowns at the active points.

Step 5 - Setup the elemental conformity matrix: One can write similar constraint equations for East and West faces as well as corner points and inner points. However, they will all give unity conformity matrices. For the sake of completeness they are given below:

$$\text{East:} \quad \begin{Bmatrix} \theta_5 \\ \theta_6 \end{Bmatrix}^e = \begin{bmatrix} C_E \end{bmatrix}^e \begin{Bmatrix} \theta_{\widehat{7}} \\ \theta_{\widehat{8}} \end{Bmatrix}^e \qquad \text{West:} \quad \begin{Bmatrix} \theta_{11} \\ \theta_{12} \end{Bmatrix}^e = \begin{bmatrix} C_W \end{bmatrix}^e \begin{Bmatrix} \theta_{\widehat{11}} \\ \theta_{\widehat{12}} \end{Bmatrix}^e$$

$$\text{Corner:} \quad \begin{Bmatrix} \theta_1 \\ \theta_4 \\ \theta_7 \\ \theta_{10} \end{Bmatrix}^e = \begin{bmatrix} C_C \end{bmatrix}^e \begin{Bmatrix} \theta_{\widehat{1}} \\ \theta_{\widehat{5}} \\ \theta_{\widehat{8}} \\ \theta_{\widehat{10}} \end{Bmatrix}^e \qquad \text{Inner:} \quad \begin{Bmatrix} \theta_{13} \\ \theta_{14} \\ \theta_{15} \\ \theta_{16} \end{Bmatrix}^e = \begin{bmatrix} C_I \end{bmatrix}^e \begin{Bmatrix} \theta_{\widehat{15}} \\ \theta_{\widehat{16}} \\ \theta_{\widehat{17}} \\ \theta_{\widehat{18}} \end{Bmatrix}^e \tag{3.5}$$

Now all the conformity matrices given in Eqs. (3.3, 3.4, 3.5) can be assembled into an elemental conformity matrix C, to relate the unknowns of the original element to the unknowns of the modified element.

$$\{\theta\}^e = [C]^e \{\widehat{\theta}\}^e \qquad \text{where,} \qquad [C]^e = \begin{bmatrix} 1 & & & & & & & & & & & & & & & & & & \\ \vdots & \ddots & & & & & & & & & & & & & & & & & \\ \vdots & & 1 & & & & & & & & & & & & & & & & \\ \vdots & & & 1 & & & & & & & & & & & & & & & \\ \vdots & & & & 1 & & & & & & & & & & & & & & \\ \vdots & & & & & 1 & & & & & & & & & & & & & \\ \vdots & & & & & & \ddots & & & & & & & & & & & & \\ \vdots & & & & & & & 1 & & & & & & & & & & & \\ 0 & & & & & & & & 1 & & & & & & & & & & \\ & & & & & & & & & 1 & & & & & & & & & \\ & & & & & & & & & & 1 & & & & & & & & \\ & & & & & & & & & & & 1 & & & & & & & \\ & & & & & & & & & & & & 1 & & & & & & \\ & & & & & & & & & & & & & 1 & & & & & \\ & & & & & & & & & & & & & & 1 & & & & \\ & & & & & & & & & & & & & & & 1 & & & \\ & & & & & & & & & & & & & & & & 1 & & \\ & & & & & & & & & & & & & & & & & 1 & \\ & & & & & & & & & & & & & & & & & & 1 \end{bmatrix}_{ncp \times \widehat{ncp}} \tag{3.6}$$

where, $\{\widehat{\theta}\}$ represents the unknowns of the modified element. As seen from this equation, elemental conformity matrices are very sparse. This is because only the passive face points are affected by the constraint functions. Unity entries are due to one-to-one matching points of the original and modified elements. Non-unity entries coming from C_S and C_N are shown with dots.

Step 7 - Modified global assembly process: After setting up the elemental conformity matrices for each element, these can be used in the modified assembly process

$$[K] = \sum_{e=1}^{ne}{}' [C]^{eT}[K]^e[C]^e, \qquad \{F\} = \sum_{e=1}^{ne}{}' [C]^{eT}\{F\}^e \tag{3.7}$$

Here it is very important to note that up to the assembly process, having nonconformities does not make any difference. Elemental stiffness matrices and force vectors are constructed using original elements as if there were not any nonconformities. Therefore CAM requires very little direct programming and computational overhead due to the nonconformities. The challenge is the design and efficient management of elemental data, which is more flexible compared to a conforming mesh.

C. Mortar Element Method (MEM)

Unlike CAM, MEM does not regain the lost C^0 continuity at the nonconforming interfaces via pointwise projection. Instead, it minimizes the jump across such interfaces in a weighted integral sense [7, 27, 31]. Again we will end up with elemental conformity matrices and use them in the modified assembly process, but the numerical values of these matrices and the way they are obtained are quite different. Let's continue working on the same configuration given at Fig. 8 and see how MEM works step by step.

Step 1 - Determine the nonconforming interfaces and type of nonconformities: This is the same as the first step of CAM.

Step 2 - Decide on active and passive faces: At p-type nonconforming South interface there is again the freedom to choose either the minimum or the maximum rule. Let's again choose the maximum rule. At h-type nonconforming East and North interfaces short rule will be used. These selections make the South and East faces passive.

Step 3 - Generate the modified element: Figure 12a shows the original element.

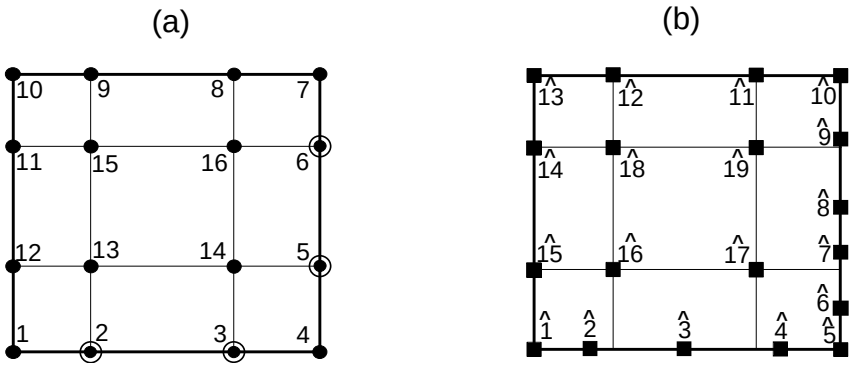

Fig. 12. MEM: (a) Original element with $ncp = 16$. (b) Constrained element with $\widehat{ncp} = \widehat{19}$. Passive points are shown with an extra circle around them. Active points are shown by squares.

Points with an extra circle around them are the passive points. Figure 12b shows the modified element obtained by replacing the points on the passive faces of the original element by the points of the active neighboring faces. Therefore this time passive points are 2, 3, 5, 6, and again all the points of the modified element are active. In the following discussion, at a p-type interface, expansion orders of the passive and active faces will be denoted by N_1 and N_2, respectively. Therefore for the South face of our example, $N_1 = 3,\ N_2 = 4$. At an h-type interface, expansion order of the long face will be denoted by N_1 and expansion orders of the two small faces by N_2 and N_3. For our example's East face, $N_1 = 3,\ N_2 = 3,\ N_3 = 2$.

Step 4 - Write the unknowns at the passive points in terms of the unknowns at the active points: This step is different than the fourth step of CAM, and it is implemented as follows.

Step 4a - Find the conformity equation for the South face: Let's first work on the South face. Fig. 13 shows the details about this p-type interface. We want to write the unknowns at the passive points 2 and 3 in terms of unknowns at the active points. This time the constraint functions will not enforce a pointwise matching, but rather

a weaker, integral type matching. We will start by taking a weighted line integral at the South face of the original element,

$$I_1 = \oint_{1-4} \theta\psi \; ds \tag{3.8}$$

where ψ is a weight function. In order to get two equations for unknowns at the two passive points (2 and 3), two weight functions are necessary. They are usually selected to be modified GLL interpolants that are two order less than the order of the original face (see Fig. 13).

$$\psi_i = (-1)^{N_1-i} \frac{P'_{N_1}(\xi)}{\xi_i - \xi} \qquad i = 1, \ldots, N_1 - 1 \tag{3.9}$$

Two order less because the end point conditions ($\theta_1 = \theta_{\hat{1}}, \; \theta_4 = \theta_{\hat{5}}$) removes two degrees of freedom from the constraint at each passive face. Using the discretized form of the unknown θ given by Eq. (2.10), Eq. (3.8) becomes

$$I_1 = \sum_{j=1}^{4} \oint_{1-4} \theta_j L_j \; \psi \; ds \tag{3.10}$$

Note that the summation includes only the points of the South face. There will be no contribution from other points because shape functions associated with those points have zero values at the South face (the face where the line integral is being evaluated). Also note that two-dimensional shape functions S, reduce to one-dimensional Lagrange interpolants L, on the faces. Now let's take a similar line integral but this time at the South face of the modified element

$$I_2 = \sum_{j=\hat{1}}^{\hat{5}} \oint_{\hat{1}-\hat{5}} \theta_j L_j \; \psi \; ds \tag{3.11}$$

Constraint functions for the two passive points can now be obtained by equating I_1 and I_2. But before doing that the two line integrals should be evaluated using

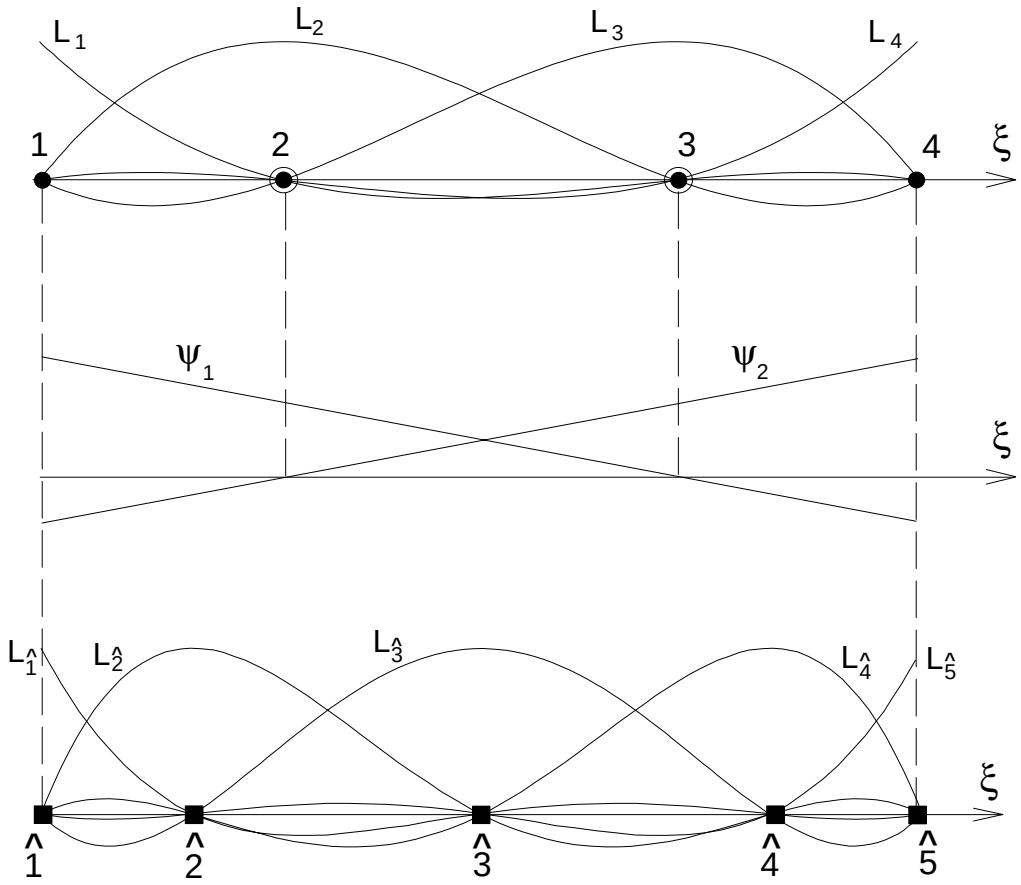

Fig. 13. Details about how MEM works at a p-type interface. 3^{rd} order original face is shown at the top. Points 2 and 3 are the passive points. 4^{th} order modified face is at the bottom. MEM uses the weight functions ψ, shown in the middle, for an integral projection of the unknowns at the passive points onto the modified face.

GLL quadratures. However, the important question is what order quadrature rule should be used. From Eq. (3.10), it can be seen that I_1 includes polynomials of order $(N_1 + N_1 - 2)$, which can be calculated exactly with N_1^{th} order GLL quadrature (N^{th} order GLL quadrature can evaluate $(2N-1)$-order polynomials exactly). On the other hand, I_2 has polynomials of order $(N_1 + N_2 - 2)$, which can be calculated exactly using a GLL quadrature of order $N = max(N_1, N_2)$. For this example $N_2 > N_1$, therefore N_2^{th} order integration will be used for I_2. After performing the numerical integrations, I_1 and I_2 take the following forms

$$I_1 = \frac{\ell}{2} \sum_{k=1}^{4} \sum_{j=1}^{4} \theta_j L_j(\xi_k) \psi(\xi_k) \rho_k \tag{3.12a}$$

$$I_2 = \frac{\ell}{2} \sum_{k=0}^{max(N_1,N_2)} \sum_{j=\widehat{1}}^{\widehat{5}} \theta_j L_j(\xi_k) \psi(\xi_k) \rho_k \tag{3.12b}$$

where $\ell/2$ comes from the Jacobian transformation, with ℓ being the physical length of the p-type interface. ξ_k and ρ_k are the integration points and weights for GLL integration, respectively. Note that for I_1, following the cardinality condition of the Lagrange interpolants, one can write $L_j(\xi_k)$ as δ_{jk} which drops one of the summations. This simplification can be applied to I_2 only if the maximum rule is used, which is the case in this example.

As discussed above, we need two constraint functions for two passive points. This can be done by using the two weight functions given by Eq. (3.9) in Eq. (3.12) and equating I_1 and I_2. This will yield to the following vector equation

$$\begin{bmatrix} \psi_1(\xi_1)\rho_1 & \psi_1(\xi_2)\rho_2 & \psi_1(\xi_3)\rho_3 & \psi_1(\xi_4)\rho_4 \\ \psi_2(\xi_1)\rho_1 & \psi_2(\xi_2)\rho_2 & \psi_2(\xi_3)\rho_3 & \psi_2(\xi_4)\rho_4 \end{bmatrix} \begin{Bmatrix} \theta_1 \\ \theta_2 \\ \theta_3 \\ \theta_4 \end{Bmatrix}^e =$$

$$\sum_{k=0}^{max(N_1,N_2)} \rho_k \begin{bmatrix} \psi_1(\xi_k) & 0 \\ 0 & \psi_2(\xi_k) \end{bmatrix} \begin{bmatrix} L_{\widehat{1}}(\xi_k) & L_{\widehat{2}}(\xi_k) & L_{\widehat{3}}(\xi_k) & L_{\widehat{4}}(\xi_k) & L_{\widehat{5}}(\xi_k) \\ L_{\widehat{1}}(\xi_k) & L_{\widehat{2}}(\xi_k) & L_{\widehat{3}}(\xi_k) & L_{\widehat{4}}(\xi_k) & L_{\widehat{5}}(\xi_k) \end{bmatrix} \begin{Bmatrix} \theta_{\widehat{1}} \\ \theta_{\widehat{2}} \\ \theta_{\widehat{3}} \\ \theta_{\widehat{4}} \\ \theta_{\widehat{5}} \end{Bmatrix}^e \tag{3.13}$$

where the summation sign individually applies to all the terms inside the matrices following it. This system can further be reduced by using the end point conditions of the interface, i.e. the fact that point 1 and 4 are exactly matching with points $\widehat{1}$ and $\widehat{5}$ (see Fig. 13). This allows us to reduce the left hand side of Eq. (3.13) by moving θ_1 and θ_4 (which are equal to $\theta_{\widehat{1}}$ and $\theta_{\widehat{5}}$, respectively) to the right hand side. The reduced system is

$$[B_S] \begin{Bmatrix} \theta_2 \\ \theta_3 \end{Bmatrix}^e = [P_S] \begin{Bmatrix} \theta_{\widehat{1}} \\ \theta_{\widehat{2}} \\ \theta_{\widehat{3}} \\ \theta_{\widehat{4}} \\ \theta_{\widehat{5}} \end{Bmatrix}^e \qquad \Rightarrow \qquad \begin{Bmatrix} \theta_2 \\ \theta_3 \end{Bmatrix}^e = [C_S] \begin{Bmatrix} \theta_{\widehat{1}} \\ \theta_{\widehat{2}} \\ \theta_{\widehat{3}} \\ \theta_{\widehat{4}} \\ \theta_{\widehat{5}} \end{Bmatrix}^e \tag{3.14}$$

where $[C_S] = [B_S]^{-1}[P_S]$ is the conformity matrix for the South face of the element we are studying. It is important to note that Eq. (3.14) has the exact same form as

Eq. (3.3) derived with CAM, but of course with different numerical values. Another point worth to mention is that $[B_S]$ is always a diagonal matrix because the weight functions ψ are nothing but reduced Lagrange interpolants and they have the cardinality property (i.e. in Eq. (3.13) $\psi_i(\xi_j) = \delta_{ij}$). Therefore taking the inverse $[B_S]$ is not a costly numerical operation.

Step 4b - Find the conformity equation for the East face: East interface, which has h-type nonconformity, requires a similar procedure to calculate the conformity matrix C_E. As sketched in Fig. 14, the original long face has to be projected to two short faces of the modified element. This time the weighted line integral taken along the original face (I_1) will be equated to the summation of two line integrals, one for each short face (I_2 and I_3)

$$I_1 = \sum_{j=4}^{7} \oint_{4-7} \theta\psi \; ds \tag{3.15a}$$

$$I_2 = \sum_{j=\widehat{5}}^{\widehat{8}} \oint_{\widehat{5}-\widehat{8}} \theta_j L_j \; \psi \; ds \tag{3.15b}$$

$$I_3 = \sum_{j=\widehat{8}}^{\widehat{10}} \oint_{\widehat{8}-\widehat{10}} \theta_j L_j \; \psi \; ds \tag{3.15c}$$

where weight functions ψ are the same as the ones given in Eq. (3.9) for the South face. These integrals can again be evaluated using GLL quadratures. I_1 has polynomials of degree $2N_1 - 2$, which can be evaluated exactly by N_1^{th} order quadrature. I_2 and I_3 has polynomials of order $N_1 + N_2 - 2$ and $N_1 + N_3 - 2$, and require $max(N_1, N_2)^{th}$ and $max(N_1, N_3)^{th}$ order quadratures, respectively (Note that in this example $N_1 = 3$, $N_2 = 3$ and $N_3 = 2$). After performing the numerical integrations Eqs. (3.15) take the following form

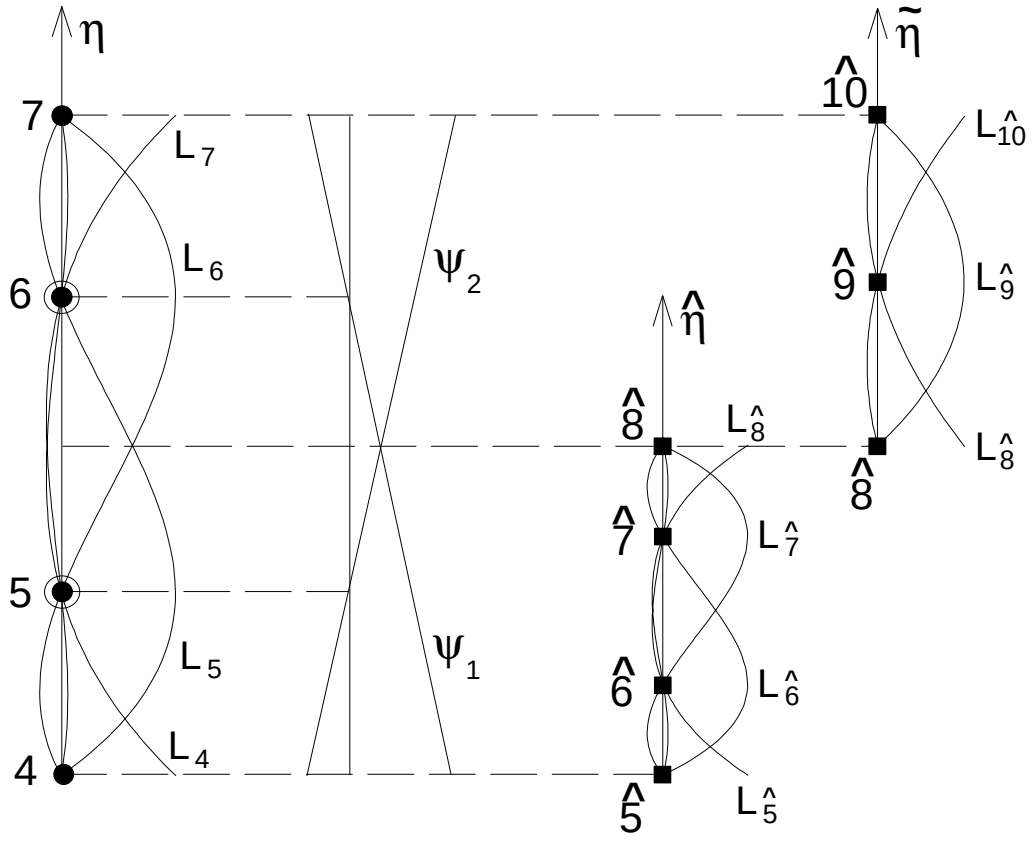

Fig. 14. Details about how MEM works at an h-type interface. 3^{rd} order original long face is shown at the left. Points 5 and 6 are the passive points. The modified short faces, of order 3 and 2, are at the right. MEM uses the weight functions ψ, shown in the middle, for an integral projection of the unknowns at the passive points onto the modified faces.

$$I_1 = \frac{\ell}{2} \sum_{k=4}^{7} \sum_{j=4}^{7} \theta_j L_j(\eta_k) \psi(\eta_k) \rho_k \tag{3.16a}$$

$$I_2 = \frac{\ell}{4} \sum_{k=0}^{max(N_1,N_2)} \sum_{j=\widehat{5}}^{\widehat{8}} \theta_j L_j(\eta_k) \psi(\eta_k^*) \rho_k \tag{3.16b}$$

$$I_3 = \frac{\ell}{4} \sum_{k=0}^{max(N_1,N_3)} \sum_{j=\widehat{8}}^{\widehat{10}} \theta_j L_j(\eta_k) \psi(\eta_k^{**}) \rho_k \tag{3.16c}$$

where ℓ is the physical length of the long face. Length of the short faces are $\ell/2$, and η_k and ρ_k are the integration points and weights, respectively. η^* and η^{**} are the projections of the local coordinates of short faces ($\widehat{\eta}$, $\tilde{\eta}$) onto the long face (η) given by (see Fig. 14)

$$\eta_k^* = \frac{\eta_k - 1}{2} \ , \qquad \eta_k^{**} = \frac{\eta_k + 1}{2}$$

Here one can understand why the short formulation is not suitable for MEM. Short formulation for MEM would require evaluation of weight functions based on short faces at collocation points of a long face, which is not possible. In other words, full projection of η onto $\widehat{\eta}$ or $\tilde{\eta}$ is not possible.

Finally the two constraint functions for passive points 5 and 6 can be obtained by using two different weight functions in Eq. (3.16) and forcing $I_1 = I_2 + I_3$

$$\begin{bmatrix} \psi_1(\eta_4)\rho_4 & \psi_1(\eta_5)\rho_5 & \psi_1(\eta_6)\rho_6 & \psi_1(\eta_7)\rho_7 \\ \psi_2(\eta_4)\rho_4 & \psi_2(\eta_5)\rho_5 & \psi_2(\eta_6)\rho_6 & \psi_2(\eta_7)\rho_7 \end{bmatrix} \begin{Bmatrix} \theta_4 \\ \theta_5 \\ \theta_6 \\ \theta_7 \end{Bmatrix}^e =$$

$$\sum_{k=0}^{max(N_1,N_2)} \rho_k \begin{bmatrix} \psi_1(\eta_k^*) & 0 \\ 0 & \psi_2(\eta_k^*) \end{bmatrix} \begin{bmatrix} L_{\widehat{5}}(\eta_k) & L_{\widehat{6}}(\eta_k) & L_{\widehat{7}}(\eta_k) & L_{\widehat{8}}(\eta_k) \\ L_{\widehat{5}}(\eta_k) & L_{\widehat{6}}(\eta_k) & L_{\widehat{7}}(\eta_k) & L_{\widehat{8}}(\eta_k) \end{bmatrix} \begin{Bmatrix} \theta_{\widehat{5}} \\ \theta_{\widehat{6}} \\ \theta_{\widehat{7}} \\ \theta_{\widehat{8}} \end{Bmatrix}^e \tag{3.17}$$

$$+ \sum_{k=0}^{max(N_1,N_3)} \rho_k \begin{bmatrix} \psi_1(\eta_k^{**}) & 0 \\ 0 & \psi_2(\eta_k^{**}) \end{bmatrix} \begin{bmatrix} L_{\widehat{8}}(\eta_k) & L_{\widehat{9}}(\eta_k) & L_{\widehat{10}}(\eta_k) \\ L_{\widehat{8}}(\eta_k) & L_{\widehat{9}}(\eta_k) & L_{\widehat{10}}(\eta_k) \end{bmatrix} \begin{Bmatrix} \theta_{\widehat{8}} \\ \theta_{\widehat{9}} \\ \theta_{\widehat{10}} \end{Bmatrix}^e$$

where the summation signs again individually apply to every term of the matrices following them. Using the endpoint conditions ($\theta_4 = \theta_{\widehat{5}}, \theta_7 = \theta_{\widehat{10}}$) this system can be reduced to

$$[B_E] \begin{Bmatrix} \theta_5 \\ \theta_6 \end{Bmatrix}^e = [P_E] \begin{Bmatrix} \theta_{\widehat{5}} \\ \theta_{\widehat{6}} \\ \theta_{\widehat{7}} \\ \theta_{\widehat{8}} \\ \theta_{\widehat{9}} \\ \theta_{\widehat{10}} \end{Bmatrix}^e \qquad \Rightarrow \qquad \begin{Bmatrix} \theta_5 \\ \theta_6 \end{Bmatrix}^e = [C_E] \begin{Bmatrix} \theta_{\widehat{5}} \\ \theta_{\widehat{6}} \\ \theta_{\widehat{7}} \\ \theta_{\widehat{8}} \\ \theta_{\widehat{9}} \\ \theta_{\widehat{10}} \end{Bmatrix}^e \tag{3.18}$$

where $[C_E]$ is the conformity matrix for the East face.

Step 5 - Setup the elemental conformity matrix: Similar to the 5^{th} step of CAM formulation, it is time to assemble the conformity matrices into one elemental

conformity matrix

$$\{\theta\}^e = [C]^e\{\widehat{\theta}\}^e \qquad \text{where,} \qquad [C]^e = \begin{bmatrix} 1 & & & & \\ \bullet\bullet\bullet\bullet\bullet & & & & \\ \bullet\bullet\bullet\bullet\bullet & & & & \\ & 1 & & & 0 \\ & \bullet\bullet\bullet\bullet\bullet & & & \\ & \bullet\bullet\bullet\bullet\bullet & 1 & & \\ & & & 1 & \\ & & & & 1 \\ & & & & & 1 \\ & 0 & & & & & 1 \\ & & & & & & & 1 \\ & & & & & & & & 1 \\ & & & & & & & & & 1 \end{bmatrix}_{ncp \times \widehat{ncp}} \tag{3.19}$$

where the entries shown with dots are coming from C_S and C_E.

Step 7 - Modified global assembly process: This step is again the same as that of the CAM formulation. Elemental conformity matrices are used to modify the global assembly process as shown in Eq. (3.7)

As demonstrated in the last two sections, formulation of CAM and MEM end up modifying the classical Galerkin formulation in very similar ways. However, they do not always perform equally well. In the next chapter we will compare their convergence and stability characteristics using simple test problems involving both p- and h-types of nonconformities.

CHAPTER IV

CONVERGENCE AND EIGENVALUE ANALYSIS OF THE DIFFUSION AND CONVECTION OPERATORS

In the previous chapter we presented two methods (CAM and MEM) that allows us to extend the conforming Galerkin Spectral Element Formulation to include p- and h-type nonconformities. Although they modify the classical formulation in similar ways, they do not always perform equally well. In this chapter, we will compare the convergence and eigenvalue characteristics of these two methods using steady and time dependent diffusion and convection operators. The behavior of the methods with these simple equations are important, because more complex equations can generally be seen as compositions of these equations.

A. Steady Diffusion Operator

Consider the following two-dimensional steady Poisson equation with Dirichlet boundary conditions

$$-\nabla^2\theta = f \qquad on \quad \Omega \in [0,1]\times[0,1] \tag{4.1a}$$

$$\theta = \theta_{exact} \qquad on \quad \Gamma \tag{4.1b}$$

The following force function

$$f = 4\pi sin(4\pi A)\left((\frac{\partial A}{\partial x})^2 + (\frac{\partial A}{\partial x})^2\right) + 4\pi cos(4\pi A)\left(\frac{\partial^2 A}{\partial^2 x} + \frac{\partial^2 A}{\partial^2 y}\right) \tag{4.2}$$

results in the exact solution of

$$\theta_{exact} = sin(4\pi A) \tag{4.3}$$

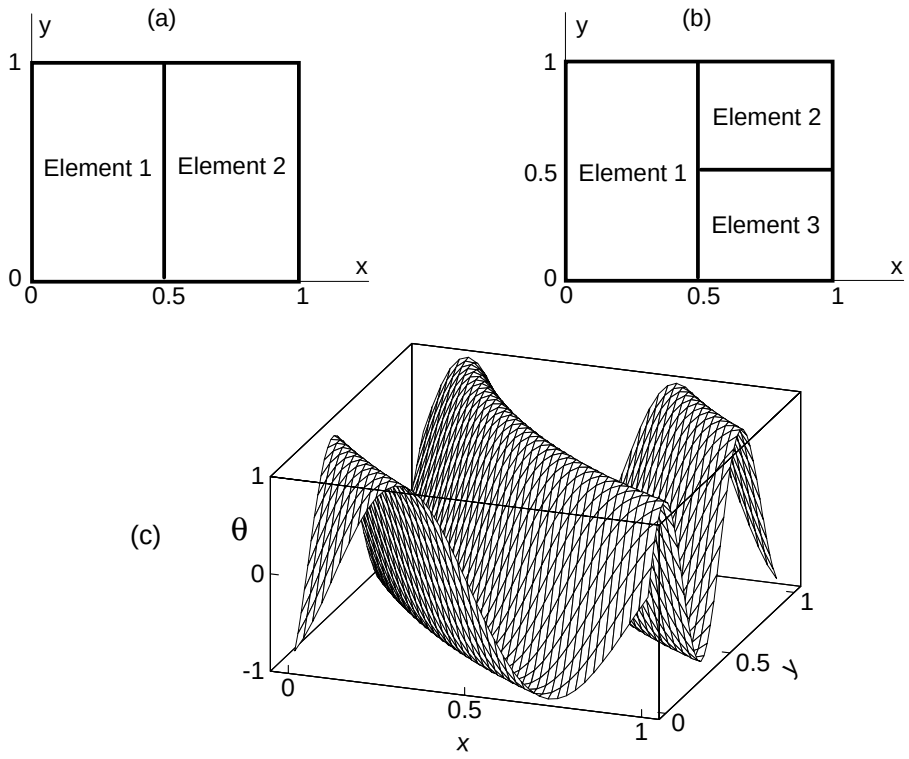

Fig. 15. (a) Two-element and (b) three-element meshes to test p-type and h-type non-conformities. (c) Exact solution given by equation Eq. (4.3)

where $A = \sqrt{(x-2)^2 + (y-2)^2}$

We will solve this problem using two different meshes shown in Fig. 15 (a and b), while Fig. 15c shows the exact solution given by Eq. (4.3).

1. Spectral Convergence on a Conforming Mesh

In the first test, defined below, we will utilize a fully conforming mesh to demonstrate the spectral convergence upon p-type refinement (p-type refinement is term used for increasing the expansion orders inside the elements without changing their geometry).

Test 1: Solve the system given in Eqs. (4.1) and (4.2) using the mesh shown in Fig. 15a. Use expansion orders of $N = N_{1x} = N_{1y} = N_{2x} = N_{2y}$, where N_{ix} and N_{iy} denotes the expansion order of the i^{th} element in the x and y directions, respectively.

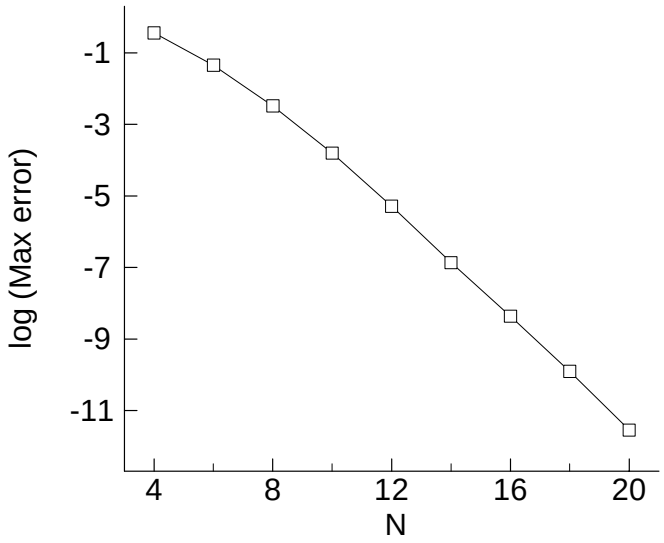

Fig. 16. Spectral convergence obtained for Test 1. Errors decrease exponentially upon increasing the expansion order N.

Figure 16 shows the convergence plot (maximum error vs expansion order) for this test. Exponential decay (straight line on a $log-lin$ plot) of the errors is a typical indication of spectral convergence. Spectral element methods provide exponential convergence for sufficiently smooth problems [1].

2. Convergence on a p-type Nonconforming Mesh

In the second test, defined below, convergence of CAM and MEM will be compared on a p-type nonconforming mesh.

Test 2: Use the same problem as in Test 1, but this time introduce p-type nonconformity by using expansion orders of $N_{1x} = N_{1y} = N_{2x} = 16$ and various values for N_{2y}. Test both CAM and MEM with minimum and maximum rules.

As seen from Fig. 17, maximum and minimum rule performs quite differently for CAM, but not much different for MEM. Let's first analyze the minimum rule cases, which are almost identical for CAM and MEM. Up to $N_{2y} = 16$ minimum rule curve

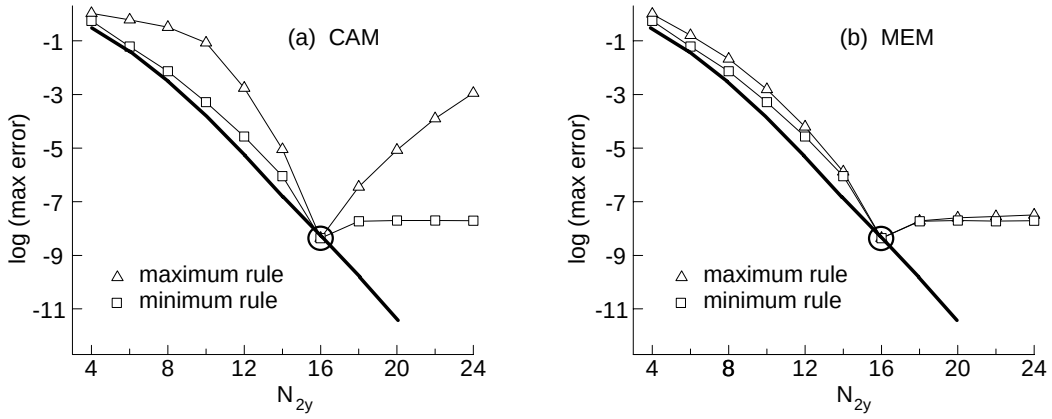

Fig. 17. Convergence obtained for Test 2. Two-element p-type nonconforming mesh is used with (a) CAM and (b) MEM. Thick line corresponds to the conforming case shown in Fig. 16 and provided for comparison.

follows the conforming convergence curve (thick line) closely (Note that N_{1y} is fixed at 16). In this interval, $N_{2y} < N_{1y}$ and maximum error occurs in element 2. Errors are slightly higher than the conforming case due to the additional "consistency error" paid for the nonconformity [34]. For $N_{2y} > 16$ maximum error shifts to element 1 and stays constant because the expansion order inside the first element is kept constant. Data points at $N_{2y} = 16$, shown with an extra circle around them, correspond to the special conforming case. That is why the curves make a dip at this point. Other than this special point, for both CAM and MEM, minimum rule curves show an almost exponential decay in the first interval and stay constant after that. This is the expected behavior. For MEM, maximum rule results are very close to the minimum rule ones, with slightly more consistency error. It is worth to mention that minimum rule uses less number of collocation points (degrees of freedom) and gives better results. With CAM, as shown in Fig. 17a, maximum rule behaves completely different. Up to $N_{2y} = 16$ it is clear that the spectral convergence is lost, and after that errors start increasing. This is not an expected behavior and shows a problem

that will be investigated in detail in the next section.

3. Convergence Problems of CAM with the Maximum Rule

Previous section showed that CAM, when used with the maximum rule, does not perform as expected. In this section we will study this behavior in more detail.

Test 3: This is an extended version of Test 2. We will solve the same problem by both varying N_{1y} and N_{2y}. Expansion orders in the x-direction are still kept constant at 16, which is high enough to make sure that the maximum errors are due to the discretization in the y-direction.

The discussion we made in the previous section about Fig. 17 is also true for Fig. 18. Fig. 18a and 18c shows that CAM and MEM performs as expected with the minimum rule. For the interval $N_{2y} < N_{1y}$, error curves closely follow the spectral convergence curve and stays constant after that. Results for MEM with maximum rule (Fig 18d) is very similar to the ones with minimum rule. However, CAM with maximum rule (Fig. 18b) does not show spectral convergence and results in much higher error levels. In this case "consistency errors" due to the formulation of the nonconformity clearly dominates the approximation errors, which exist in every case. We believe that these results are generalizations of the polynomial order incompatibility problem mentioned in [34], where the relative importance of consistency and approximation errors is analyzed for pointwise matching (CAM) and integral matching (MEM). They worked with polynomials and showed that for CAM, when used with maximum rule, consistency errors due to the nonconformity is not bounded for certain combinations of N_{1y} and N_{2y}. It is easy to demonstrate the findings in [34] by solving a Poisson problem with a polynomial exact solution.

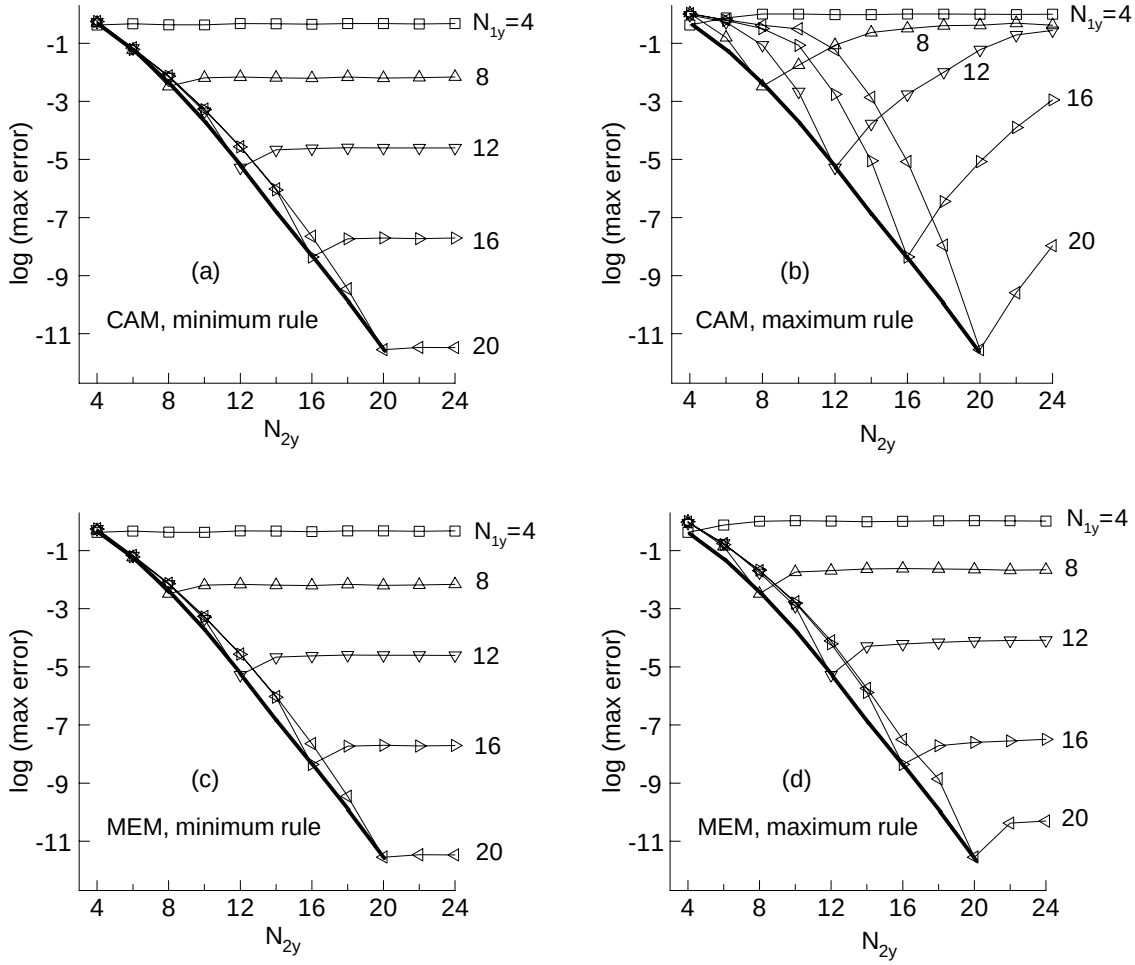

Fig. 18. Convergence curves obtained for Test 3. Two-element h-type nonconforming mesh is used with combinations of (a) CAM, minimum rule (b) CAM, maximum rule, (c) MEM, minimum rule, and (d) MEM, maximum rule. Thick line corresponds to the conforming case shown in Fig. 16 and provided for comparison.

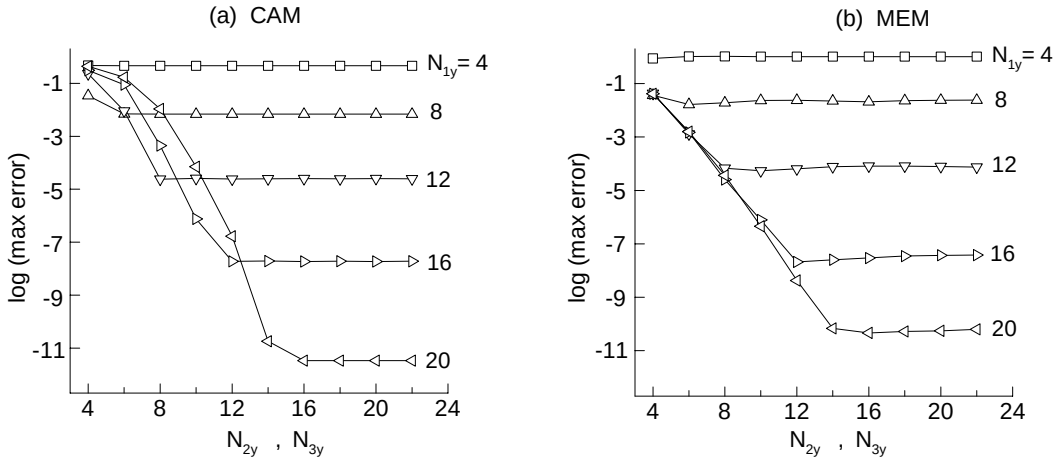

Fig. 19. Convergence obtained for Test 4. Three-element, h-type nonconforming mesh is used with (a) CAM and (b) MEM. Note that CAM uses the long rule and MEM uses the short rule.

4. Convergence on an h-type Nonconforming Mesh

This is another detailed test similar to the previous one, but this time on a three-element, h-type nonconforming mesh.

Test 4: Use the same problem as in Test 3, but this time use the three-element mesh with h-type nonconformity as shown in Fig. 15b. Take $N_{1x} = N_{2x} = N_{3x} = 16$, and use various values for N_{1y}, N_{2y} and N_{3y}. Test both CAM and MEM.

Figure 19 shows the convergence curves for this test. For h-type nonconformities, instead of maximum and minimum rules, we use long rule with CAM and short rule with MEM. Convergence curves follow a similar trend to those obtained in previous sections. Let's consider the curve obtained with MEM for $N_{1y} = 16$. Up to $N_{2y} = 12$ the error decays exponentially. Maximum error occurs inside one of the small elements. After $N_{2y} > 12$ maximum error shifts to the big element, i.e. element 1, and the error stays constant because the expansion order of element 1 is kept constant. Similar behavior is obtained for other values of N_{1y}. Curves for CAM deviate from the

straight line of spectral convergence in the interval $N_{2y} < N_{1y}$. Compared to MEM, CAM requires higher expansion orders to get the same level of error. For $N_{2y} > N_{1y}$ errors stay constant with values slightly lower than the corresponding MEM cases. However, in a physical problem it is not likely that the order of expansion in the small elements (N_{2y}, N_{3y}) to be higher than that of the large element (N_{1y}).

B. Eigenvalue Analysis of the Diffusion Operator

In this section we will analyze the eigenvalue spectrum of the diffusion operator.

Test 5: Analyze the eigenvalue spectrum of the diffusion operator using two-element p-type and three-element h-type nonconforming meshes. Unsteady Poisson equation given by

$$\frac{\partial \theta}{\partial t} - \nabla^2 \theta = 0 \tag{4.4}$$

gives (after a semi-discrete formulation) the global discrete system of $\dot{\theta} = M^{-1} D\theta$, which can be put into the following eigenvalue problem

$$(M^{-1}D - \lambda I)\phi = 0 \tag{4.5}$$

where λ and ϕ are the eigenvalues and corresponding eigenvectors, respectively. M and D are the mass and diffusion matrices. All the boundaries are taken to be Dirichlet type.

Figure 20 shows the growth of maximum eigenvalues with the expansion order. Figure 20a is for a conforming mesh. The straight line has a slope of two, suggesting that the maximum eigenvalue increases linearly with the square of the expansion order, i.e. $|\lambda|_{max} \sim \mathcal{O}(N^2)$. This agrees with the global spectral methods [28]. Similar trends are obtained for p-type and h-type non-conforming meshes. In Fig. 20c eigenvalues for MEM are slightly higher than those of CAM because MEM uses

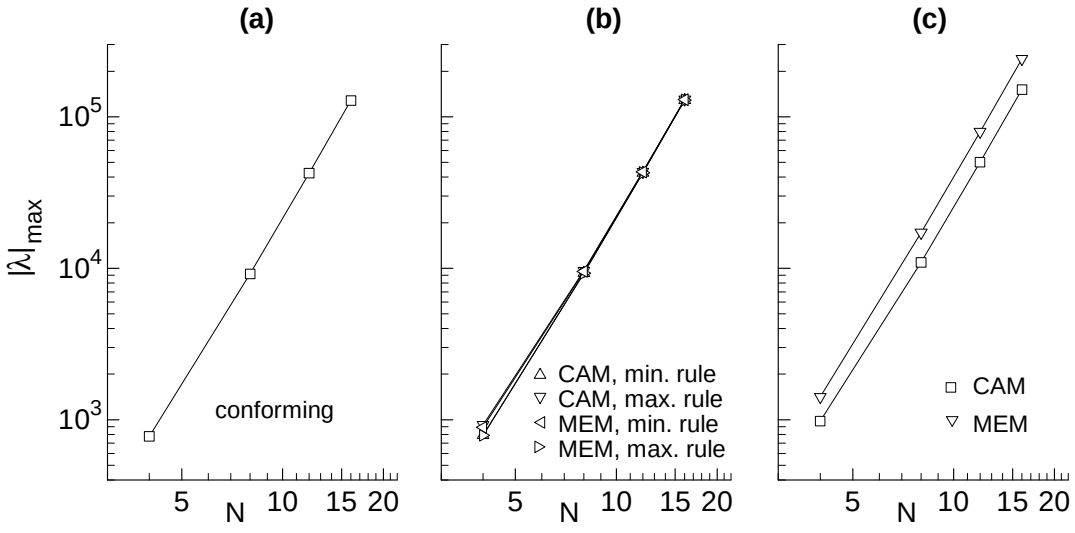

Fig. 20. Maximum eigenvalues for Test 5. Using (a) conforming mesh with same expansion order in both elements in both directions, (b) p-type nonconforming mesh with $N = N_{1x} = N_{1y} = N_{2x}$ and $N_{2y} = N+2$, (c) h-type nonconforming mesh with same expansion order in all elements in both directions.

the short rule resulting in more degrees of freedom. Note that for every case shown in Fig. 20, all the eigenvalues are real and negative. Therefore nonconformities do not bring any instability problems for the diffusion operator, if one uses absolutely stable implicit schemes.

C. Eigenvalue Analysis of the Convection Operator

Let's repeat similar eigenvalue tests for the convection operator.

Test 6a, 6b: Analyze the eigenvalue spectrum of the convection operator using the four-element, p-type nonconforming mesh shown in Fig. 21a. Unsteady convection equation is given by

$$\frac{\partial \theta}{\partial t} + \mathbf{u} \cdot \nabla \theta = 0 \tag{4.6}$$

where $\mathbf{u}$ is a two-dimensional velocity field. For simplicity we will use a velocity with

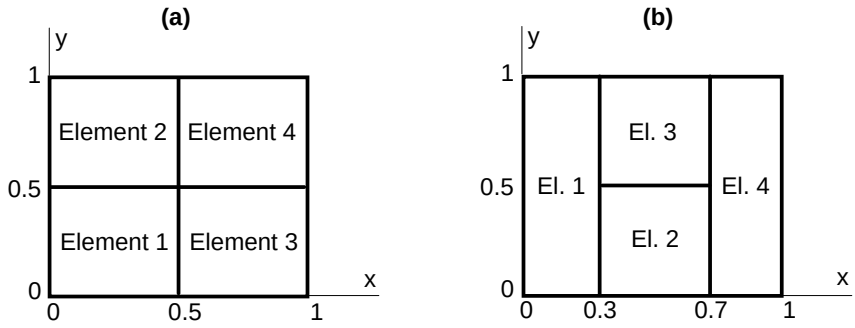

Fig. 21. Four-element meshes used in the convection tests

a magnitude of 1.0 and perform tests with flow going from left-to-right and right-to-left. After a semi-discrete formulation, Eq. (4.6) gives the global discrete system of $\dot{\theta} = -M^{-1}A\theta$, which can be put into the following eigenvalue problem

$$(-M^{-1}A - \lambda I)\phi = 0 \tag{4.7}$$

where A is the convection matrix. Two different sets of boundary conditions will be used.

(a) Dirichlet conditions on all four boundaries,

(b) Dirichlet conditions on the top and bottom boundaries, periodic conditions on the left and right boundaries.

These two cases will be referred to as Test 6a and Test 6b, respectively. Eigenvalue spectrums for Test 6a and 6b are shown in Fig. 22. Same results are obtained for CAM and MEM, so this figure will be referred without making a distinction between CAM and MEM. All the plots in this figure are for the case when the velocity field is from left-to-right. For cases when the velocity field is in the reverse direction we got symmetric plots with respect to the imaginary axis, which are not shown. In these plots, we are mostly concerned about the eigenvalues with positive real parts because they are known to create stability problems for long time integrations.

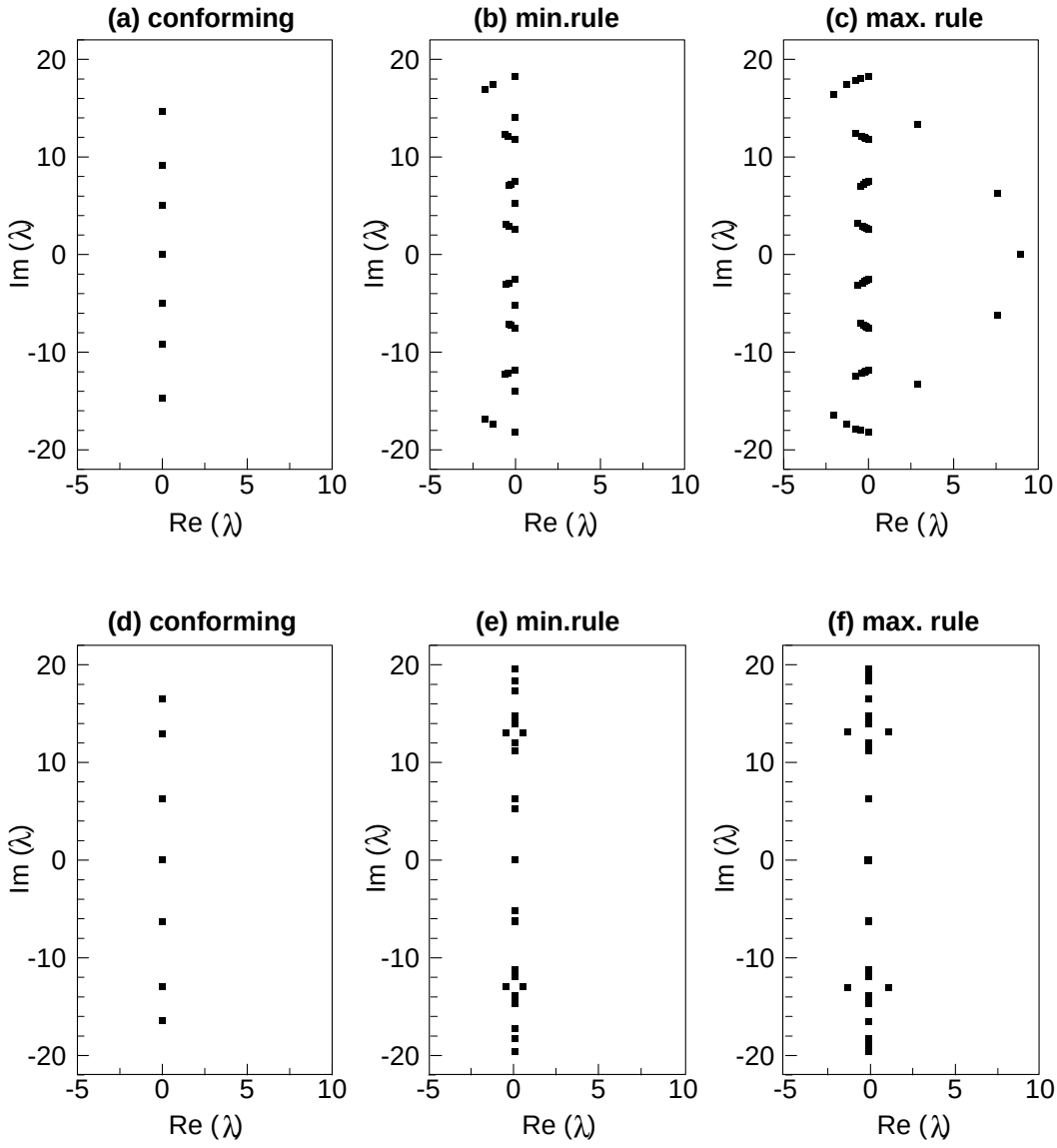

Fig. 22. Eigenvalue spectrums for Test 6a (top) and 6b (bottom). Using (a) conforming mesh, (b) nonconforming with minimum rule, (c) nonconforming with maximum rule. For conforming cases $N = 4$ is used in all elements. For nonconforming cases, expansion orders of $N_1 = N_2 = 4$ and $N_3 = N_4 = 5$ are used.

As seen from Figs. 22a and 22d, conforming configurations result in all imaginary eigenvalues, as expected for the convection operator. Fig. 22b is for a case when the flow is going from lower order $N = 4$ to higher order $N = 5$ using the minimum rule. We noticed that some of the eigenvalues shifted to the negative real plane. If we reverse the flow direction (the case when the flow is going from higher order to lower order, which is not shown) the eigenvalues will shift to the positive real plane, which is not desired. Fig. 22e is for periodic boundaries, which means low and high order elements repeat one after the other continuously. In other words, flow will pass from lower order to higher order and vice versa regardless of its direction. This configuration results in eigenvalues with symmetric real parts, and eigenvalues on the positive real plane can not be avoided.

Fig. 22c uses all Dirichlet boundary conditions and maximum rule with flow going from lower order to higher order. The results are similar to the case with minimum rule (Fig. 22b) with the exception of some eigenvalues with large positive real parts. Finally, Fig. 22f uses maximum rule with periodic boundaries. Similar to Fig. 22c, eigenvalues have symmetric real parts, that is the flow direction is not important.

Unlike the diffusion operator discussed in the previous section, eigenvalues of the convection operator behaves very different with conforming and nonconforming interfaces. The eigenvalues obtained by CAM and MEM are very close to each other. They depend on the choice of minimum or maximum rule. They also depend on the direction of the flow, that is passing from a high order element to a low order one or vice versa makes a difference. Positive real eigenvalues seen in most cases are due to the consistency errors, and make the solution of this time dependent problem difficult. Note that with the maximum rule (Figs. 22c and 22f) this problem is more severe compared to the minimum rule (Figs. 22b and 22e). Later in this chapter we'll solve

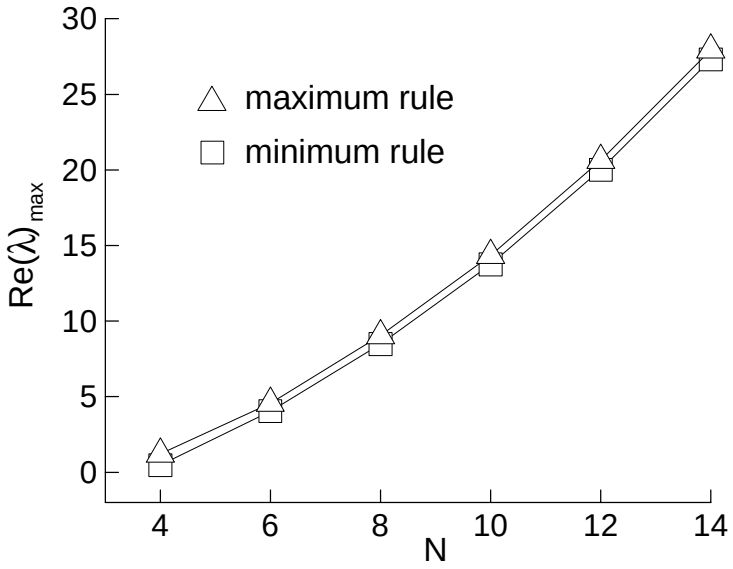

Fig. 23. Maximum real part of the eigenvalues for Test 6b using maximum and minimum rules. Four-element mesh of Fig. 21a, with periodic inlet outlet is used with expansion orders of $N_1 = N_2 = N$ and $N_3 = N_4 = N + 1$.

a pure convection problem to demonstrate the effects of the positive eigenvalues.

We will continue by solving Test 6b using various orders of expansions to understand the relationship between the maximum real part of the eigenvalues $Re(\lambda)_{max}$, and the expansion order N (This is similar to Test 5 that was performed for the diffusion operator). Results are shown in Fig. 23. Minimum and maximum rules behaves very similarly. $Re(\lambda)_{max}$ increases *almost* linearly with the expansion order, which makes the problem numerically more difficult to solve.

Test 7a, 7b: Previous test considered only p-type nonconformities. In this test we will study the eigenvalue spectrum of the convection operator using the three-element, h-type nonconforming mesh shown in Fig. 15b. Again we will distinguish two cases, Test 7a: all four boundaries are Dirichlet type, and Test 7b: top and bottom boundaries are Dirichlet type and right and left boundaries are Periodic.

Eigenvalue spectrums for Test 7a and 7b are shown in Fig. 24. The flow is going

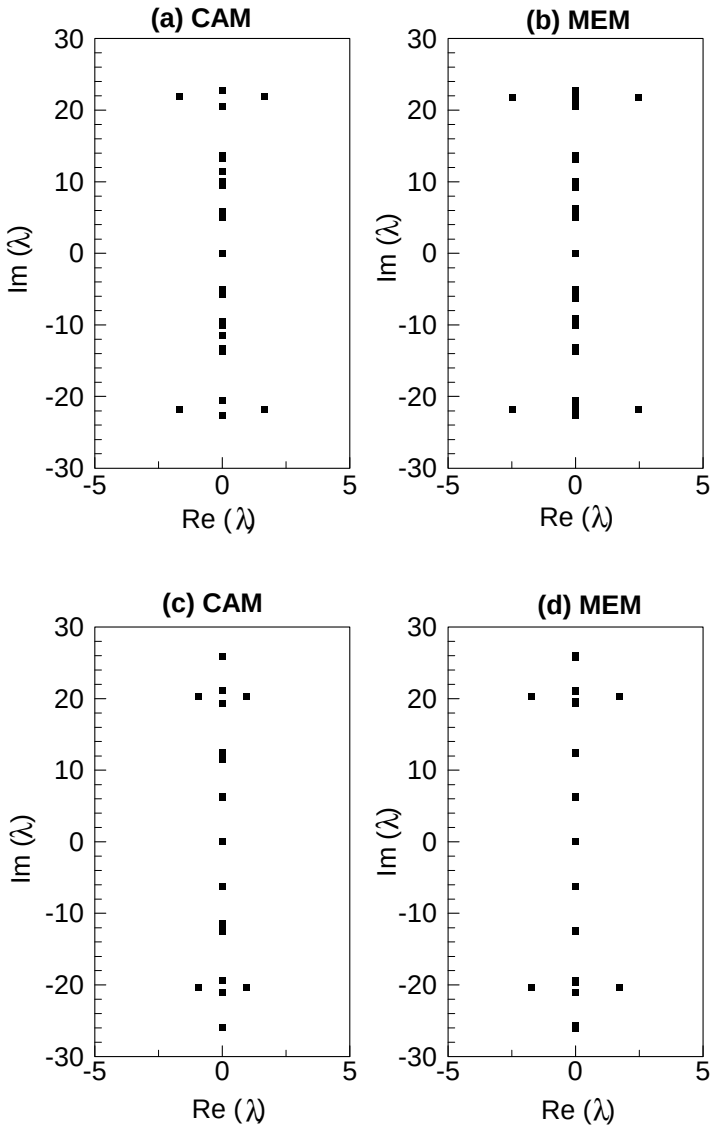

Fig. 24. Eigenvalue spectrums for Test 7a (top) and 7b (bottom). $N_x = N_y = 4$ used in all elements.

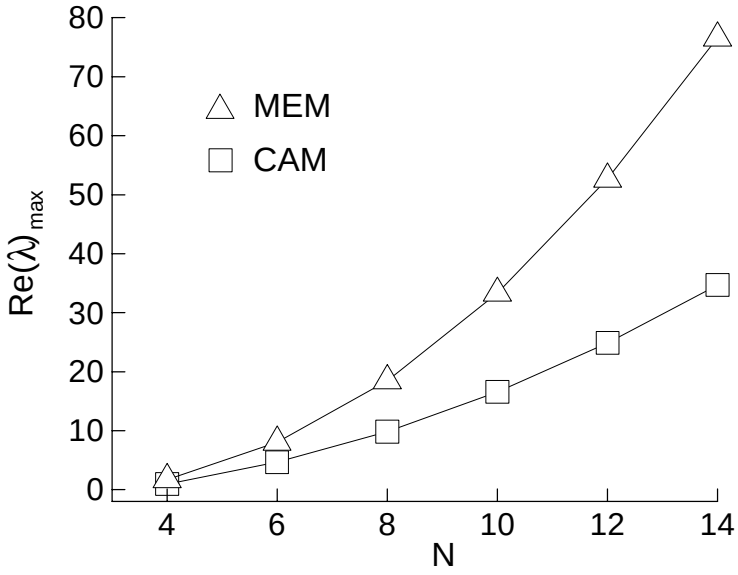

Fig. 25. Maximum real parts of the eigenvalues for Test 7b using CAM and MEM. Four-element mesh of Fig. 21b, with periodic inlet outlet, is used with expansion orders of N in each element.

in the positive x direction. Unlike p-type nonconformities, results for CAM and MEM are different, because the former uses the long rule while the latter uses the short rule. Eigenvalues obtained with MEM (Figs. 24b and 24d) are spread more on the real axis with larger real parts. Different than p-type nonconformities, Figs. 24a and 24c are symmetric with respect to the imaginary axis, meaning that the direction of the flow is not important.

Fig. 25 shows the relationship between the maximum real part of the eigenvalues $Re(\lambda)_{max}$, and the expansion order N. Behavior of CAM is similar to the one obtained for the p-type refinement (Fig. 23). $Re(\lambda)_{max}$ for MEM increases more rapidly.

D. Convergence Analysis of the Pure Convection Equation

In the last section we studied the eigenvalue spectrum of the convection operator in case of nonconforming interfaces. Now we will study the convergence characteristics

of the unsteady convection problem. Our focus will be on the eigenvalues with real positive parts and their affects on the stability of the time integration.

Consider the following two-dimensional unsteady convection-diffusion equation

$$\frac{\partial \theta}{\partial t} - \alpha \nabla^2 \theta + \frac{\partial \theta}{\partial x} = f \qquad on \;\; \Omega \in [0,1] \times [0,1] \tag{4.8}$$

which, for a zero force function, will yield the following exact solution

$$\theta_{exact} = sin(2\pi(x-t)) \; sin(\pi y) \; e^{-5\pi^2 \alpha t} \tag{4.9}$$

where α is the constant diffusivity. To get a pure convection equation we will take α to be zero. The solution for this problem is a modified sine wave traveling in the positive x-direction. The initial condition, obtained by setting $t = 0$ in Eq. (4.9), is shown in Fig. 26. We will use the four-element meshes shown in Fig. 21. On the top and bottom boundaries, exact solution will be specified as a Dirichlet boundary condition. Left and right boundaries will be periodic. Time integration will be done by the second-order, implicit Crank Nicolson scheme, with a time step of 0.0002.

Test 8: Let's start with a fully conforming four-element mesh, using same expansion order in all elements and in both x and y-directions. Note that we are solving a pure convection problem with zero diffusivity.

Figure 27 shows the time history of the errors for various expansion orders. Error levels decrease exponentially as expansion order is increased from $N = 4$ to $N = 8$. Small time step of 0.0002 results in errors dominated by space discretization, which accumulate slightly as time passes. All three cases are stable.

Test 9: Let's repeat the previous test with expansion orders of $N_1 = N_2 = N, N_3 = N_4 = N + 2$ so that there will be p-type nonconforming interfaces. CAM with the maximum rule will be used. Note that MEM gives the same results as CAM and minimum rule differs only slightly from the maximum rule (see Figs. 22 and 23).

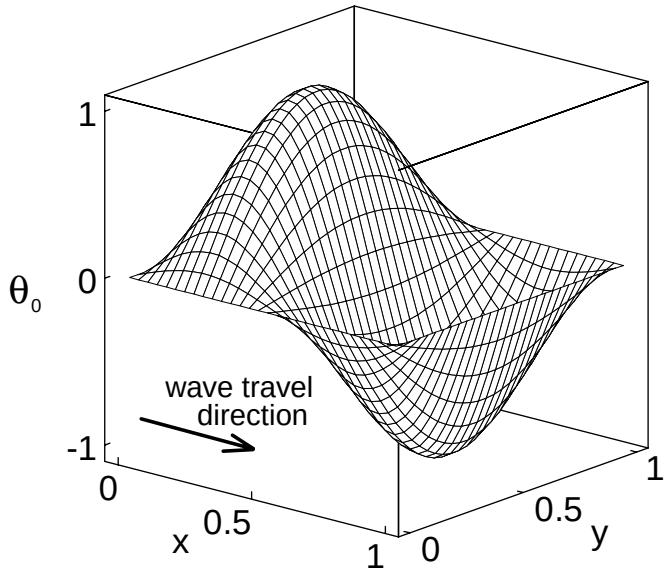

Fig. 26. Initial condition for the convection problem, $\theta_0 = sin(2\pi x)sin(\pi y)$

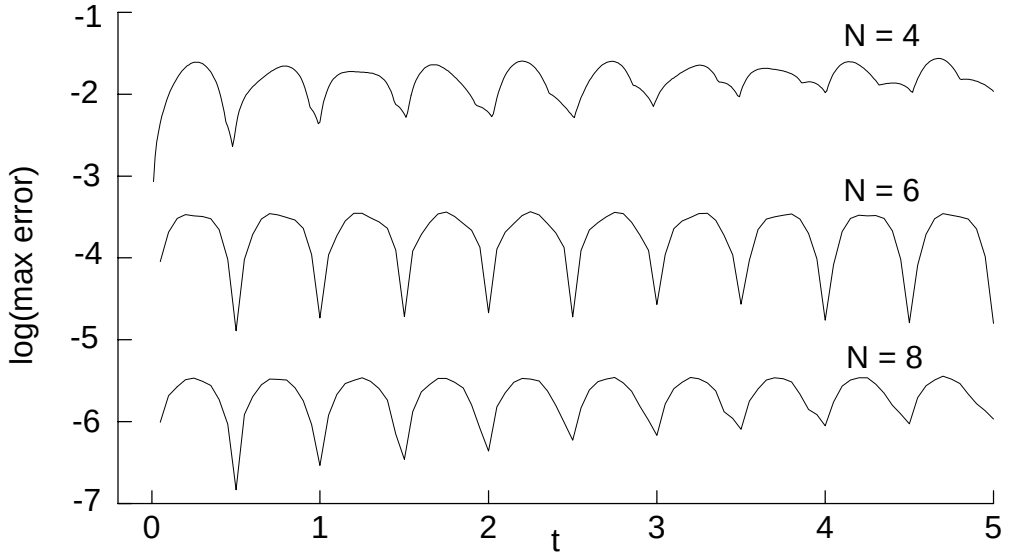

Fig. 27. Time history of the error for Test 8. Uses a conforming mesh with all four elements having the same expansion order N. $t = 1$ corresponds to one cycle of the sine wave.

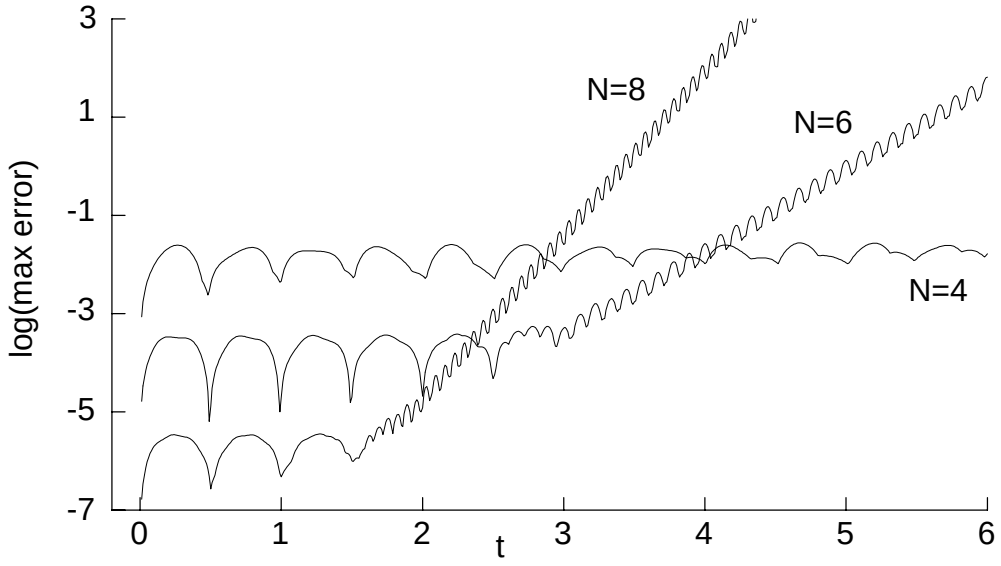

Fig. 28. Time history of the error for Test 9. p-type nonconforming interfaces are generated by using expansion orders of $N_1 = N_2 = N, N_3 = N_4 = N + 1$. $t = 1$ corresponds to one cycle of the sine wave.

Figure 28 shows the time history of the errors for various expansion orders. Only the case for $N = 4$ runs successfully for six cycles of the sine wave. Cases for $N = 6$ and $N = 8$ goes unstable after couple of cycles. Eigenvalues with positive real parts, introduced by the nonconforming formulation, are responsible for these blow-ups. The rate at which the error increases for $N = 8$ is larger than that of for $N = 6$. These error growth rates are directly related to the maximum positive real part of the eigenvalues (see Fig. 23).

Test 10: We will repeat Test 8 using the h-type nonconforming, four-element mesh shown in Fig. 21b. Same expansion order will be used in all elements.

Figure 29a and 29b show the time history of the errors for various expansion orders, for CAM and MEM, respectively. CAM results are very similar to the results of the previous test shown in Fig. 29. This is expected because of the similarity seen between the the max eigenvalue results shown in Figs. 23 and 25. For MEM, insta-

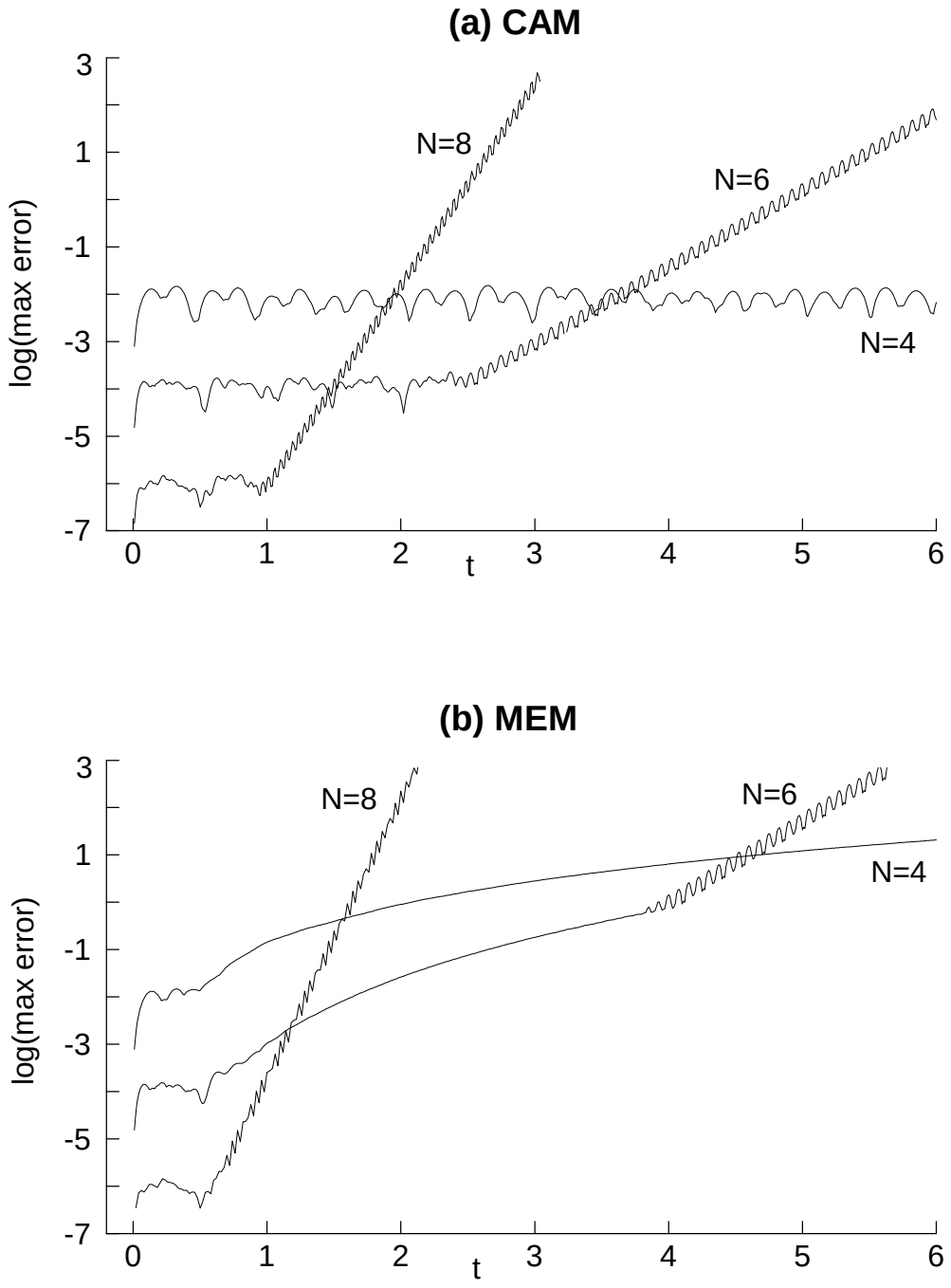

Fig. 29. Time history of the error for Test 10. Using (a) CAM, (b) MEM. All four elements use the same expansion order. $t = 1$ corresponds to one cycle of the sine wave.

bilities setup earlier and errors increase with higher slopes, which can be explained by Fig. 25, which shows higher positive eigenvalues for MEM compared to CAM. Even the case $N = 4$ is giving problems with MEM.

In the last three tests (8, 9, 10), a semi-discrete formulation with Crank-Nicolson time integration is used. Crank-Nicolnson scheme is an absolutely stable scheme, with the stability region covering the whole 2^{nd} and 3^{rd} quadrants of the eigen-plane. But nonconforming formulations produces eigenvalues with positive real parts, which are responsible for the blow-ups. Additional consistency errors due to the nonconforming formulations are causing convergence problems. To understand further if this is a stability or a consistency problem, we repeated all three runs using a fully-coupled space time formulation (instead of the previously used semi-discrete formulation). Similar to the spatial discretization, Lagrange interpolation functions based on GLL points are used for the time discretization. Although the coupled formulation practically has no stability restrictions, we obtained the same results. Therefore we conclude that for the pure convection problem, the additional consistency errors due to the nonconforming formulations result in difficulties for unsteady problems. Our eigenvalue results are similar to those presented in [29], although in that study only p-type nonconformities are considered and CAM and MEM are only used with the minimum and maximum rule, respectively. The conclusion was that CAM and MEM behaves differently and MEM results in stability problems for certain cases. However, we showed that these behaviors can be explained by the use of minimum and maximum rules (compare Fig. 22b and 22c), not CAM and MEM. Therefore, the stability problems they reported are due to the use of the maximum rule, rather than the use of MEM.

E. Convergence Analysis of the Convection-Diffusion Equation

In the previous section we considered the pure convection problem. Now we will study the generalized convection-diffusion equation given by Eq. (4.8) with a nonzero diffusivity. Same travelling wave problem will be solved, exact solution of which is given by Eq. (4.9).

Test 11: Solve the convection-diffusion equation with a diffusivity of $\alpha = 0.01$ and periodic side boundaries. Use the four-element meshes shown in Fig. 21 to study fully conforming, p-type nonconforming and h-type nonconforming cases.

For the conforming case all four elements have expansion orders N. For the p-type nonconforming case, elements 1 and 2 have expansion orders N, and elements 3 and 4 have expansion orders $N + 2$. For the h-type nonconforming case, all elements have expansion order $N_x = N$ in the x direction, elements 1 and 4 have expansion orders $N_y = N$, and elements 2 and 3 have expansion orders $N_y = 2$ in the y-direction. Convergence results are shown in Fig. 30. As given by Eq. (4.9), the analytical solution decreases exponentially by time, and so is the error. In order to circumvent this, we normalized the error by dividing it with $e^{-5\pi^2\alpha t}$. Crank-Nicolson scheme is used for time integration. All four cases shown in Fig. 30 ran successfully for 10 cycles (first 5 is plotted), providing spectral convergence upon increasing the expansion order. The added diffusion is enough to shift all the eigenvalues to the left eigen-plane (in other words, enough to suppress the consistency errors), resulting in successful solutions. For the p-type nonconforming cases (b and c), maximum rule results in larger errors, although it uses more degrees of freedom. The difference between minimum and maximum rule is more apparent for lower expansion orders, especially with CAM. For the h-type nonconforming case CAM and MEM provides very similar results.

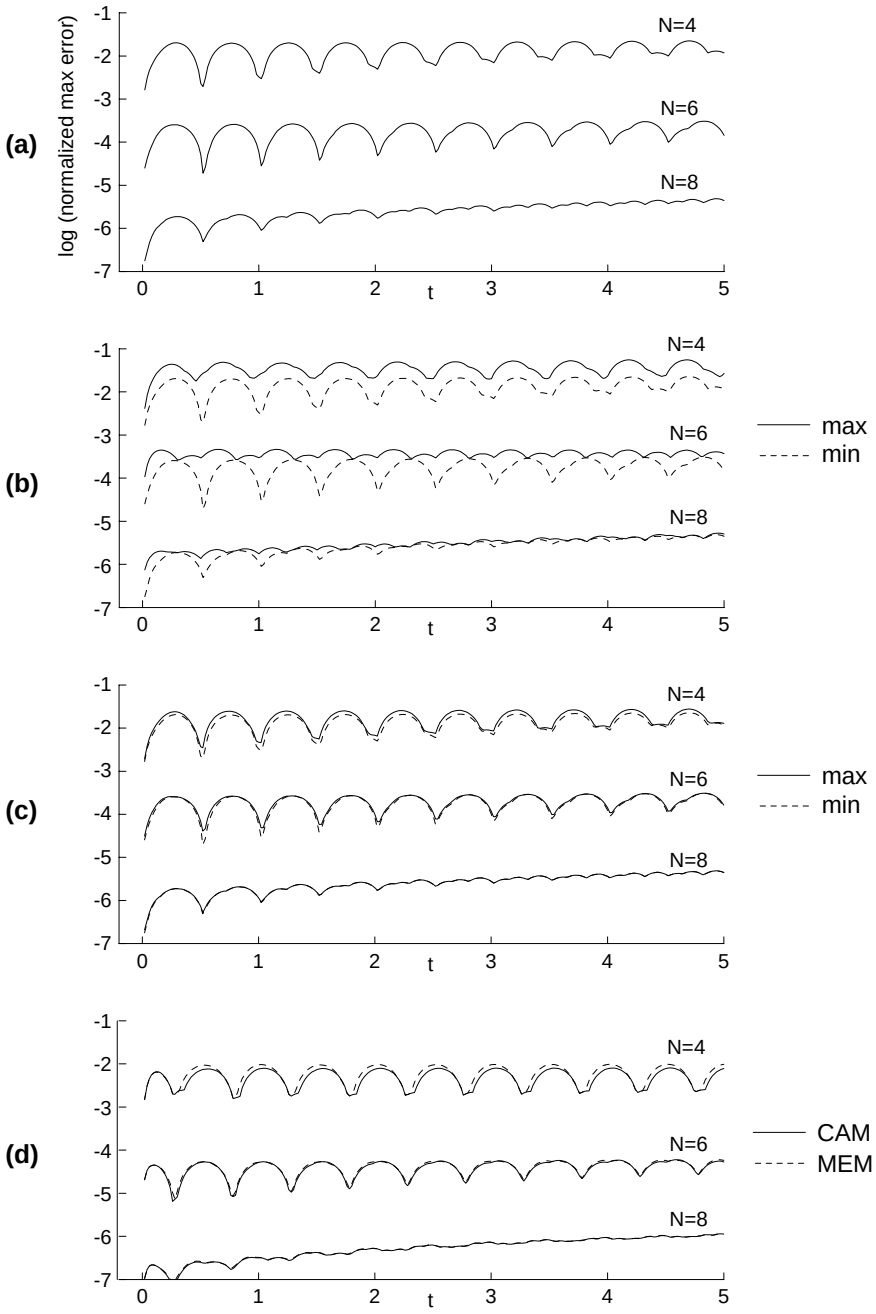

Fig. 30. Time history of the error for Test 11. Using (a) conforming mesh, (b) p-type nonconforming mesh with CAM, (c) p-type nonconforming mesh with MEM, (d) h-type nonconforming mesh. $t = 1$ corresponds to one cycle of the sine wave.

CHAPTER V

INCOMPRESSIBLE STOKES AND NAVIER-STOKES EQUATIONS

In this section we will develop Stokes and Navier-Stokes solvers for two-dimensional, steady and unsteady, laminar, incompressible flows, with the emphasis on the utilization of nonconforming meshes. We will start with the governing equations, summarize popular solution techniques and continue with the Galerkin Spectral Element formulation. Than we will validate the solvers using a number of test problems. These problems will be solved using both for conforming and nonconforming meshes to observe the affects of nonconforming formulations on spectral convergence. Nonconforming problems will be solved using both CAM and MEM to compare their convergence and stability characteristics.

A. Governing Equations

Dynamics of laminar, incompressible fluid flow is governed by the Navier-Stokes equations (written using the primitive variables)

$$\frac{\partial \mathbf{v}}{\partial t} + (\mathbf{v} \cdot \nabla)\mathbf{v} - \nu \nabla^2 \mathbf{v} + \nabla p = \mathbf{f} \tag{5.1a}$$

$$\nabla \cdot \mathbf{v} = 0 \tag{5.1b}$$

where $\mathbf{v} = u\mathbf{i} + v\mathbf{j}$ is the velocity vector on the Cartesian coordinates, p is the pressure, ν is the kinematic viscosity and $\mathbf{f} = f_x\mathbf{i} + f_y\mathbf{j}$ is the body force vector. For simplicity we assume that the density is $\rho = 1$. Eq. (5.1b) is the incompressibility constraint, and it is usually treated as a part of the Navier-Stokes equations. First term on the left hand side of the Eq. (5.1a) drops for steady problems. Second term of this equation represents the inertial affects and they are negligible for low speed flows. If

this term is dropped, one ends up with the Stokes equation. Although Stokes equation is a simplified form of the Navier-Stokes, it accurately represents many physical flows. For example, most microflows exhibit Stokes flow conditions [35].

B. Typical Numerical Solution Techniques

Although there are countless research papers and textbooks devoted to the numerical solution of incompressible Navier-Stokes equations, this topic still remains to be an open research area [36]. The main difficulty in solving incompressible Navier-Stokes equations is due to the incompressiblity constraint. In the set of equations given by (5.1), pressure is not a thermodynamic variable because there is no equation of state for an incompressible fluid [37]. For incompressible flows, pressure is responsible for maintaining a divergence free velocity field, and it achieves this without actually appearing in the continuity equation (5.1b). This makes it impossible to solve both pressure and velocity field at once and brings many challenges to the numerical solution process. Another difficulty is due to the nonlinear inertial terms (which are not present in the Stokes equations). For time dependent problems these nonlinear terms are usually treated explicitly in an effort to increase computational efficiency. But for stability, implicit schemes are preferred for the remaining terms, which results in multi-step solution procedures. Other difficulties arise for advection dominated (high Reynolds number) flows, which are usually handled with upwinding techniques.

The most widely used methods for solving incompresible Navier-Stokes equations fall into one the following categories:

1. Projection methods: These methods decouple solution of the pressure and velocity fields in a very efficient and easy to implement way. They involve two steps: a convection-diffusion problem is solved to obtain an intermediate velocity field (which

is not divergence free) and a Poisson problem is solved to find the pressure. Presure correction methods and fractional-step (splitting) methods are commonly used examples of this method. Although widely used, the basic principles of these methods are still open for discussion (see the "biharmonic miracle" discussion in [38]). For example the boundary conditions that are necessary for the pressure Poisson equation are not well understood. The use of simple but improper boundary conditions are not uncommon, which yields unphysical numerical boundary layers [37]. These methods are known to perform better for advection dominated flows and not preferred for low Reynolds number problems [14, 19]. They are mostly first-order in time, although high-order splitting schemes based on stiffly-stable time integration rules are also developed [39].

2. Penalty method: This is an effective technique that is used to eliminate the pressure from the momentum equation (Eq. (5.1a)) [4, 19]. It is based on the simple fact that, for incompressible flows pressure acts like a Lagrange multiplier to maintain a divergence free velocity field. A concern with the penalty formulation is the selection of a penalty parameter, which affects the accuracy of the scheme. This parameter is generally problem dependent and needs some trial and error process for a good estimate. Large penalty parameters result in solutions that satisfy the incompressibility condition better, but also result in stiff systems that are difficult to solve.

3. Uzawa method: This is probably the simplest and the "most clean" method among the ones discussed here. It involves two steps: In the first step, the incompressibility constraint, Eq. (5.1b), is substituted into the momentum equation, Eq. (5.1a), to solve for the pressure. Next step simply solves for the velocity field using the already computed pressure. It enables to staisfy the incompressibility constraint exactly [39]. In order to satisfy the *inf-sup* or Ladhyzenskaya-Bubuska-Brezzi (LBB)

condition [15] and to eliminate spurious pressure modes [40] it uses lower order expansions for the pressure approximation, which usually requires use of a semi staggered grid. A semi staggered grid does not have any pressure nodes at the boundaries, therefore no pressure boundary condition is needed. It also makes nonconforming formulations easier because pressure is not evaluated at element interfaces, therefore no special treatment is necessary for it. The only disadvantage of the Uzawa method is that it is computationaly demanding. It is usually used with iterative solvers, although direct solutions are possible with the use of Schur complement decomposition (static condensation) technique [14, 19]. Details of the Uzawa formulation will be discussed in the following sections.

C. Galerkin Spectral Element Formulation of the Navier-Stokes Equations

In this section we will provide and discuss the set of algebraic equations that can be obtained after following a procedure similar to the one given in Chapter 2. This procedure basically involves the strong formulation, residual equation, weight functions and integration by parts. Skipping the intermediate steps (details of which can be found in Reddy [4]) a typical semi-discrete Galerkin formulation of the incompressible Navier-Stokes equations results in the following global set of equations

$$\begin{bmatrix} [M^{11}] & [0] & [0] \\ [0] & [M^{22}] & [0] \\ [0] & [0] & [0] \end{bmatrix} \begin{Bmatrix} \{\dot{u}\} \\ \{\dot{v}\} \\ \{\dot{p}\} \end{Bmatrix} + \begin{bmatrix} [K^{11}] & [K^{12}] & [K^{13}] \\ [K^{12}]^T & [K^{22}] & [K^{23}] \\ [K^{13}]^T & [K^{23}]^T & [0] \end{bmatrix} \begin{Bmatrix} \{u\} \\ \{v\} \\ \{p\} \end{Bmatrix} = \begin{Bmatrix} \{F^1\} \\ \{F^2\} \\ \{0\} \end{Bmatrix} \quad (5.2)$$

where the elemental matrices are

$$
\begin{aligned}
M_{ij}^{11^e} &= M_{ij}^{22^e} = \int_{\Omega^e} S_i S_j \; d\Omega^e \\
K_{ij}^{11^e} &= \int_{\Omega^e} \nu \left(2\frac{\partial S_i}{\partial x}\frac{\partial S_j}{\partial x} + \frac{\partial S_i}{\partial y}\frac{\partial S_j}{\partial y} \right) d\Omega^e + \int_{\Omega^e} S_i \left(\bar{u}\frac{\partial S_j}{\partial x} + \bar{v}\frac{\partial S_j}{\partial y} \right) d\Omega^e \\
K_{ij}^{12^e} &= \int_{\Omega^e} \frac{\partial S_i}{\partial y}\frac{\partial S_j}{\partial x} \; d\Omega^e \\
K_{ij}^{13^e} &= -\int_{\Omega^e} \frac{\partial S_i}{\partial x}\tilde{S}_j \; d\Omega^e \\
K_{ij}^{22^e} &= \int_{\Omega^e} \nu \left(\frac{\partial S_i}{\partial x}\frac{\partial S_j}{\partial x} + 2\frac{\partial S_i}{\partial y}\frac{\partial S_j}{\partial y} \right) d\Omega^e + \int_{\Omega^e} S_i \left(\bar{u}\frac{\partial S_j}{\partial x} + \bar{v}\frac{\partial S_j}{\partial y} \right) d\Omega^e \\
K_{ij}^{23^e} &= -\int_{\Omega^e} \frac{\partial S_i}{\partial y}\tilde{S}_j \; d\Omega^e \\
F_i^{1^e} &= \int_{\Omega^e} f_x S_i \; d\Omega^e + \oint_{\Gamma^e} t_x \; ds^e \\
F_i^{2^e} &= \int_{\Omega^e} f_y S_i \; d\Omega^e + \oint_{\Gamma^e} t_y \; ds^e
\end{aligned}
\tag{5.3}
$$

where $\bar{u}$ and $\bar{v}$ are known values of the velocity components of the previous iteration level (or time step for unsteady problems). t_x and t_y are the traction terms representing the Neumann boundary conditions. S is the GLL based shape function for the velocity approximation, given by Eq. (2.9). $\tilde{S}$ is the shape function for the pressure approximation, which is the tensor product of one-dimensional Gauss Lobatto (GL) interpolants $\tilde{L}$, given by

$$
\tilde{L}_M(\xi_m) = \frac{P_{M+1}(\xi)}{P'_{M+1}(\tilde{\xi}_m)(\xi - \tilde{\xi}_m)} \; , \qquad m \in [0, M] \tag{5.4}
$$

where P and P' are Legendre polynomial and its derivative, respectively. $\tilde{\xi}$ are the GL collocation points. Using GLL points for velocity and GL points for pressure results in a semi staggered grid, an example of which is shown in Fig. 31. As seen from the figure, there are no pressure points on the element faces, which means that for nonconforming meshes no special treatment is necessary for the pressure. This is an advantage of using semi staggered grids in nonconforming formulations.

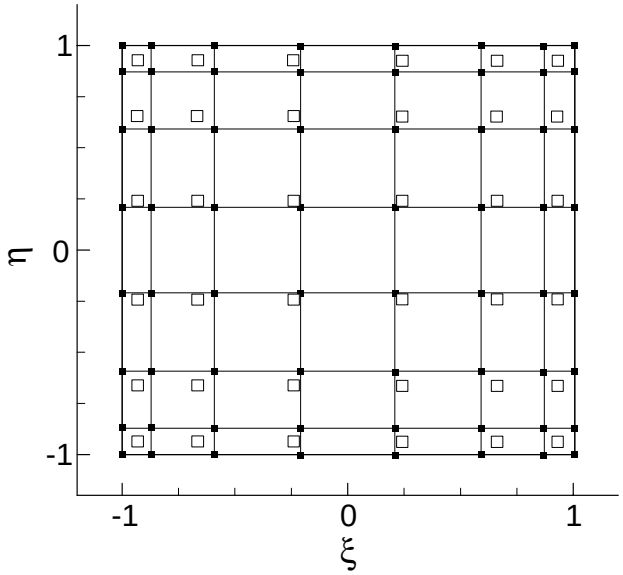

Fig. 31. A typical semi staggered grid element. It uses 7th and 5th order polynomials for velocity and pressure approximations, respectively. GLL points for velocity are shown by dots and GL points for pressure are shown by squares.

In such a grid configuration, pressure approximation becomes two order less than the velocity approximation, which is necessary to satisfy the *inf-sup* condition [15]. Although staggered grids are commonly used for incompressible Navier-Stokes equations, nonstaggered grids with equal order velocity and pressure approximation were also reported to give successful results. One typical use of nonstaggered grids involves a velocity approximation based on GLL interpolants and same order of pressure approximation based on Legendre functions. Many other examples can be found in [40].

Eq. (5.2) is not symmetric due to the nonlinear terms in $[K^{11}]$ and $[K^{22}]$. These nonlinear terms will be dropped for the Stokes equations, resulting in a symmetric system. It is important to mention that the convective terms in equation Eq (5.2) are written using a conservative form. Other forms are available, such as skew-symmetric or convective. Although mathematically they are equivalent, each has advantages and

disadvantages considering numerical calculations. For example, when the convective form is used for the Stokes equations, a rearrangement of the terms in Eq. (5.3) will result in zero matrices for $[K^{12}]$ and $[K^{21}]$. A detailed discussion about different ways of implementing the convective terms can be found in [29].

D. Uzawa Method

The system of equations given in (5.2) has zero diagonal entries, and can not be inverted and solved as it is. As mentioned earlier in this chapter, Uzawa method provides a simple way to solve for velocity and pressure separately. It is straightforward and enforces the incompressibility constraint as accurately as possible. Let's start by writing Eq. (5.2) as two separate equations

$$\begin{bmatrix} [M^{11}] & [0] \\ [0] & [M^{22}] \end{bmatrix} \begin{Bmatrix} \{\dot{u}\} \\ \{\dot{v}\} \end{Bmatrix} + \begin{bmatrix} [K^{11}] & [K^{12}] \\ [K^{21}] & [K^{22}] \end{bmatrix} \begin{Bmatrix} \{u\} \\ \{v\} \end{Bmatrix} + \begin{bmatrix} [K^{13}] \\ [K^{23}] \end{bmatrix} \Big\{ p \Big\} = \begin{Bmatrix} \{F^1\} \\ \{F^2\} \end{Bmatrix} \tag{5.5a}$$

$$\begin{bmatrix} [K^{31}] & [K^{32}] \end{bmatrix} \begin{Bmatrix} \{u\} \\ \{v\} \end{Bmatrix} = \Big\{ 0 \Big\} \tag{5.5b}$$

which can be put into the following compact form

$$[M]\{\dot{V}\} + [L]\{V\} + [D]^T\{p\} = \{F\} \tag{5.6a}$$

$$[D]\{V\} = \{0\} \tag{5.6b}$$

For the sake of clarity let's present the Uzawa method separately for steady and unsteady equations.

1. Uzawa Method for Steady Problems

For steady Navier-Stokes equations first term in Eq. (5.6) will drop.

Firt step of the Uzawa method: Premultiplying Eq. (5.6a) by $[D][L]^{-1}$ gives

$$[D]\{V\} + [D][L]^{-1}[D]^T\{p\} = [D][L]^{-1}\{F\} \tag{5.7}$$

First term of Eq. (5.7) can be eliminated using Eq. (5.6b), to get the following pressure equation

$$\{p\} = \left([D][L]^{-1}[D]^T\right)^{-1} \; [D][L]^{-1}\{F\} \tag{5.8}$$

where $[S] = [D][L]^{-1}[D]^T$ is called the pressure matrix.

Second step of the Uzawa method: Velocity field can now be calculated by using the already calculated pressure in Eq. (5.6a)

$$\{V\} = [L]^{-1} \; \left(\{F\} - [D]^T\{p\}\right) \tag{5.9}$$

First step is numerically costly, since the pressure matrix $[S]$ is a full matrix and its inversion is not easy. Usually conjugate gradient type iterative methods are used for this step, because $[S]$ can be preconditioned effectively [19]. For unsteady problems, especially the preconditioning becomes more involved. In this study however, we will use a direct solution approach and reduce the computational requirements (both storage and computational time) using the Schur complement decomposition technique.

2. Uzawa Method for Time Dependent Problems

The method described in the previous section can be extended to time dependent problems. Here we will present the formulation for general α-schemes [4]. For the

following general system of equations

$$[M]\{\dot{\theta}\} + [K]\{\theta\} = \{F\} \tag{5.10}$$

α-schemes result in the following time discretization

$$[\hat{K}]_{n+1}\{\theta\}_{n+1} = [\bar{K}]_n\{\theta\}_n + \{\hat{F}\}_{n,n+1} \tag{5.11}$$

where

$$\begin{aligned} [\hat{K}]_{n+1} &= [M] + \alpha\Delta t[K]_{n+1} \\ [\bar{K}]_n &= [M] - (1-\alpha)\Delta t[K]_n \\ \{\hat{F}\}_{n,n+1} &= \Delta t\ [\ \alpha\{F\}_{n+1} + (1-\alpha)\{F\}_n\ ] \end{aligned} \tag{5.12}$$

with subscripts n and $n+1$ representing the values at the current and the next time levels, respectively. Δt is the constant time step. When we apply this to the unsteady Navier-Stokes equations, Eqs. (5.6) take the following form

$$[\hat{L}]_{n+1}\{V\}_{n+1} + [\hat{D}]^T\{p\}_{n+1} = \{\hat{F}\}_{n,n+1} + [\bar{L}]_n\{V\}_n - [\hat{D}]^T\{p\}_n \tag{5.13a}$$

$$[\hat{D}]\{V\}_{n+1} = [\hat{D}]\{V\}_n \approx \{0\} \tag{5.13b}$$

where

$$[\hat{L}]_{n+1} = \begin{bmatrix} [M] & [0] \\ [0] & [M] \end{bmatrix} + \alpha\Delta t \begin{bmatrix} [K^{11}] & [K^{12}] \\ [K^{21}] & [K^{22}] \end{bmatrix}_{n+1} \tag{5.14a}$$

$$[\bar{L}]_n = \begin{bmatrix} [M] & [0] \\ [0] & [M] \end{bmatrix} - (1-\alpha)\Delta t \begin{bmatrix} [K^{11}] & [K^{12}] \\ [K^{21}] & [K^{22}] \end{bmatrix}_n \tag{5.14b}$$

$$[\hat{D}] = \alpha\Delta t[D] \tag{5.14c}$$

$$[\bar{D}] = (1-\alpha)\Delta t[D] \tag{5.14d}$$

In the first step, we multiply Eq. (5.13a) by $[\hat{D}][\hat{L}]_{n+1}^{-1}$ to eliminate the first step, and end up with the following pressure equation

$$\{p\}_{n+1} = [\hat{S}]^{-1} \left(\{\hat{F}\}_{n,n+1} + [\bar{L}]_n \{V\}_n - [\hat{D}]^T \{p\}_n \right) \tag{5.15}$$

where $[\hat{S}]^{-1} = [\hat{D}][\hat{L}]_{n+1}^{-1}[\hat{D}]^T$ is the pressure matrix for the unsteady formulation. In the second step, velocity field at the new time level is calculated by

$$\{V\}_{n+1} = [\hat{L}]_{n+1}^{-1} \left(\{\hat{F}\}_{n,n+1} + [\bar{L}]_n \{V\}_n - [\hat{D}]^T \{p\}_n - [\hat{D}]^T \{p\}_{n+1} \right) \tag{5.16}$$

The α-schemes take different names for different α values. In this study we will use the second-order, implicit Crank-Nicolson scheme, which corresponds to $\alpha = 0.5$.

E. Test Problems

In this section we'll solve three test problems to validate our Navier-Stokes solvers. First one is the time-periodic oscillatory flow in a channel with known exact solution, which is used to test the time stability of the solvers. Second one is the steady Kovasznay flow, which resembles the flow behind a set of cylinders. Finally we will study the lid-driven cavity problem at $Re = 500$. In each problem we will use CAM and MEM on both p- and h-type nonconforming meshes and compare the results.

1. Oscillatory Flow in a Channel

Later in Chapter 6 we will study the heat transfer in two-dimensional channels by oscillatory forced convection. Velocity field for this problem has a known analytical solution, which will be used here to test the time stability of our Navier-Stokes solver. For the sake of completeness, we preferred to keep the details of this problem in Chapter 6. As shown in Fig. 37 we are considering the flow between two parallel

plates, driven harmonically in time with a pressure gradient given in Eq. (6.6). The resultant velocity profile is given by Eq. (6.7) [41]. Here we will study this problem for a Womersley number of 10 (see Eq. (6.2)), by solving the unsteady Navier-Stokes equations and compare the results with the analytical solution. The following three strategies will be used

a) Conforming: Four element mesh shown in Fig. 21a is used (with a different range in the y-axis, $-0.5 < y < 0.5$). In the y-direction, same expansion order N_y is used for all elements. Since the flow is not changing in the x-direction, a low order expansion $N_x = 3$ is used for all elements. This is also true for the following cases.

b) p-type nonconforming: Same four element mesh is used. Elements 1 and 4 have expansion orders N_y, and elements 2 and 3 have expansion orders $N_y + 2$.

c) h-type nonconforming: Geometrically nonconforming four element mesh shown in Fig. 21b is used. Elements 2 and 3 have expansion orders N_y, and elements 1 and 4 have expansion orders $N_y + 4$.

Exact solution at time zero is provided as the initial condition and the Navier-Stokes equations are integrated in time for 10 cycles. All cases run without any stability problems, with the errors shown in Fig. 32. As seen, spectral convergence is obtained for all cases. For the p-type nonconforming cases, despite it uses more degrees of freedom, maximum rule does not perform as good as the minimum rule. These findings are in agreement with the results of the diffusion operator study given in Chapter 4 (see Fig. 18). For the h-type nonconforming case CAM performs better than MEM, as expected. This is because of the *short rule* CAM uses, which uses more degrees of freedom.

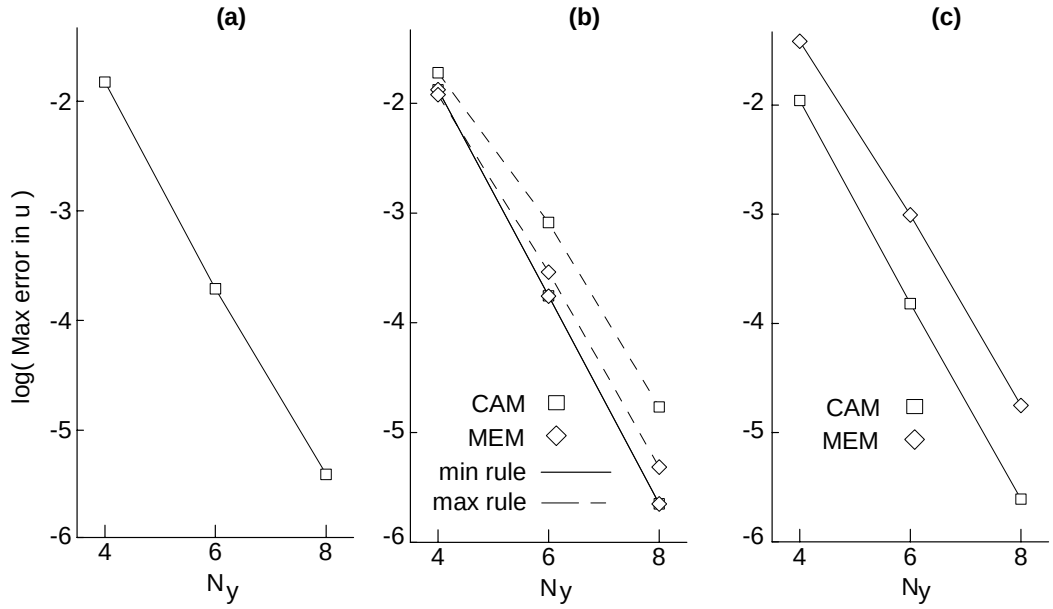

Fig. 32. Convergence results for the solution of the oscillatory flow in a channel. For (a) conforming (b) p-type nonconforming (c) h-type nonconforming cases. $N_x = 3$ for all elements in all cases.

2. Kovasznay Flow

Kovasznay flow is a steady, laminar flow with a known exact solution. It was first studied by Kovasznay in 1948. Later it became a popular test problem for high-order methods [19, 39]. The flow looks similar to the low-speed flow of a viscous flow past an array of cylinders as seen in Fig. 33a. The analytical solution to the Navier-Stokes equations is given by

$$\begin{aligned} u &= 1 - e^{\lambda x} cos(2\pi y) \\ v &= \lambda/2\pi \; e^{\lambda x} sin(2\pi y) \\ p &= 0.5(1 - e^{\lambda x}) \end{aligned} \tag{5.17}$$

where $\lambda = 0.5/\nu - (0.25/\nu^2 + 4\pi^2)^{0.5}$ and we choose $\nu = 1/40$. Similar to the previuous test problem we will perform conforming, p-type nonconforming and h-

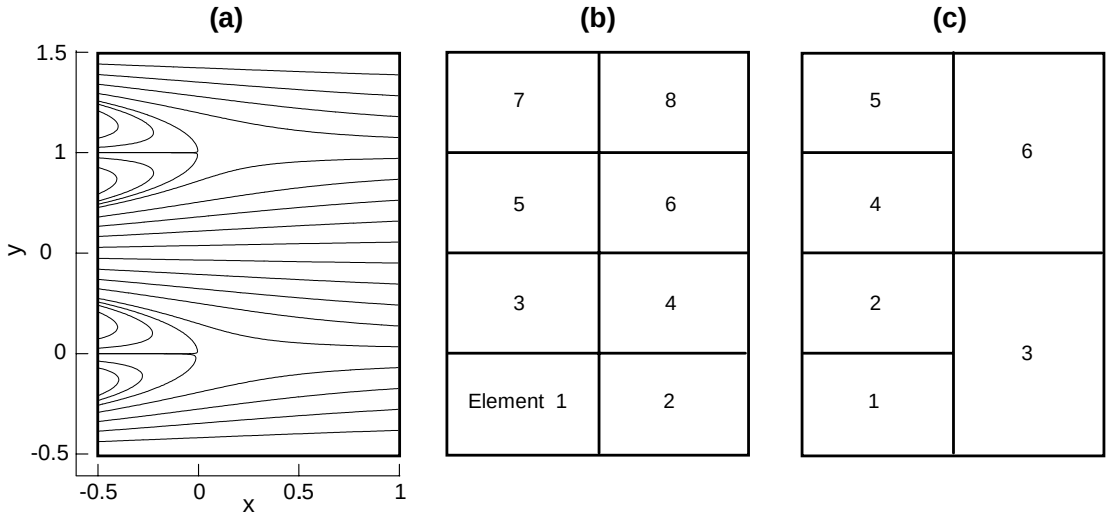

Fig. 33. Streamlines for the exact solution of the Kovasznay flow and two-different meshes used for the Kovasznay problem

type nonconforming solutions, as follows

a) Conforming: Eight element mesh shown in Fig. 33b is used. Same expansion order N is used in all elements.

b) p-type nonconforming: Same eight element mesh is used. Elements 1, 3, 5, 7 has expansion orders N, whereas elements 2, 4, 6, 8 has expansion orders $N-2$. Only the maximum rule is tested.

c) h-type nonconforming: Six element mesh shown in Fig. 33c is used. All elements has expansion order N, except elements 3 and 6 has expansion orders $N+4$ in the y-direction.

Known exact solution is specified at all boundaries. Fig. 34 shows convergence results obtained from the steady Navier-Stokes solver. This time maximum error is plotted against the square root of total number of degrees of freedom (including both velocity and pressure dof). Nonconforming solutions use more than one expansion order, therefore in order to provide a fair comparison of different solutions on a single

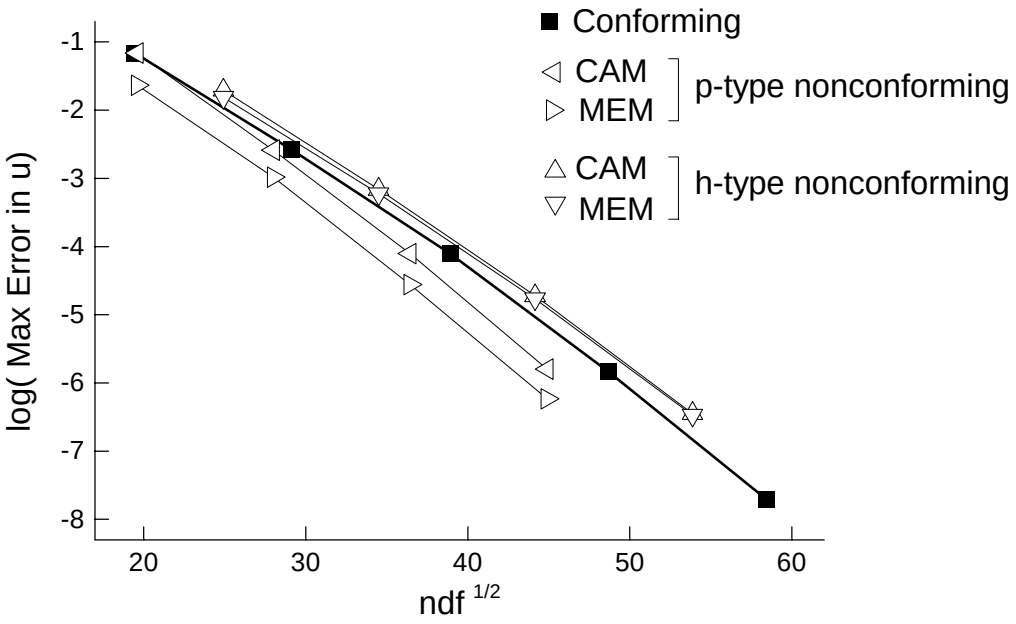

Fig. 34. Convergence results for different solutions of the Kovasznay flow. Maximum rule is used for the p-type nonconforming case. ndf is the total degrees of freedom including both velocity and pressure.

plot *ndf* is used instead of N. Taking the square root of ndf makes sure that the exponential convergence appears as a straight line on a log-lin graph. As seen from the figure, all three strategies result in spectral convergence. Similar to the previous case when we use maximum rule with p-type nonconformity MEM performs better than CAM. For the h-type nonconformity case, CAM and MEM results are practically the same.

3. Lid-Driven Cavity Problem

Lid-driven cavity problem is a classical Navier-Stokes test case due to its simple geometry, yet challenging nature. The problem geometry and boundary conditions are shown in Fig. 35. Top wall is moving with a velocity of $u = -1$, while all other walls are stationary. Although this problem does not have a closed form exact

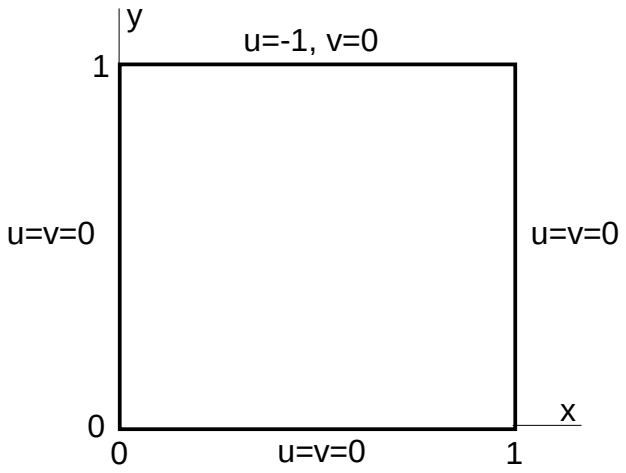

Fig. 35. Lid-driven cavity problem. Top wall is moving with a velocity of $u = -1$. Other walls are stationary.

solution, it has been studied extensively and many highly accurate benchmark results are available [42, 43]. The challenging aspect of this problem is due to the resolution of the corner singularities. Pressure and vorticity are not finite at the top corners, which makes the problem difficult for high-order formulations. At the bottom corners, singularities are much weaker.

Using a Reynolds number of 500, we performed a series of h- and p-type refinements. Results are shown in Fig. 36 as contour plots of u velocity. Case (a) uses four elements of order N=8. In order to resolve the top corners better, in case (b), top two elements are divided into four. Further h-type refinement results in case (c), which has 24 elements. Finally in case (d) elements at the top corners are further refined and approximation orders of the shaded elements are increased to 10 or 12. This last case has both h- and p-type nonconformities. Although we are not presenting any numerical values, smoothness of the velocity contours clearly shows that h- and p-type refinements provide better resolution. Similar to the previous test problems, the results for CAM and MEM are practically the same. The results shown are

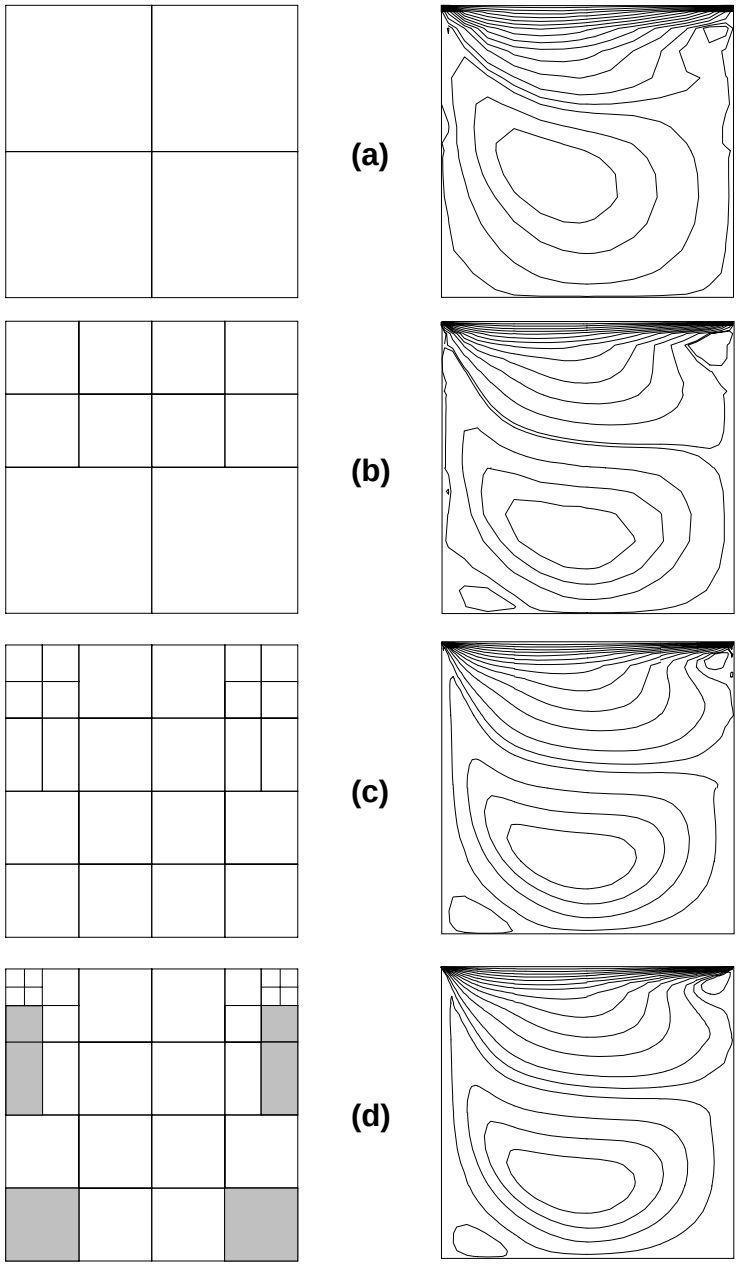

Fig. 36. Meshes used and u-velcoity contours obtained for the lid-driven cavity problem at $Re = 500$. h-type refinement is done from (a) to (b) and (b) to (c). p-type refinement is done from (c) to (d) only on the shaded elements. Contour plots are produced by Tecplot, which can not perform polynomial expansions, creating coarser looking results than the actual high-order ones.

obtained with the steady Navier-Stokes solver starting from a stationary condition. The problem is also solved with the unsteady solver successfully, without any time instabilities.

CHAPTER VI

APPLICATION: OSCILLATORY FLOW FORCED CONVECTION IN TWO-DIMENSIONAL CHANNELS

In this chapter we will use the developed solvers to study a practical engineering problem, oscillatory forced convection cooling in two-dimensional channels. We will perform a detailed analysis and comparison of the heat transfer characteristics of oscillatory and unidirectional flows for a channel with heated top wall. Time dependent velocity and temperature profiles, instantaneous and time-averaged surface and bulk temperature distributions, and Nusselt number variations will be presented.

A. Background

Fluid flow and heat transfer in circular tubes, ducts and channels have extensive engineering applications, including heat exchanger design, biomedical engineering and micro-fluidics. Steady forced convection heat transfer in channels and tubes is well understood. Simple geometry and steady flow conditions enable analytical solutions and collection of reliable experimental data. This results in analytical and empirical relations for the Nusselt number variations in terms of the flow parameters [44]. However, there are relatively fewer investigations of oscillatory-flow heat transfer, which has more stringent time and spatial resolution requirements. Oscillatory flows can be grouped into two categories: pulsating (modulated) and reciprocating (fully reversing) flows. Pulsating flows are always unidirectional and can be decomposed into steady and unsteady components, such as in the case of blood flow in arteries [45]. For reciprocating flows, the flow direction changes cyclically. Hence, these flows convect zero net mass. With the advent of micro-electromechanical systems (MEMS) and micro-fluidics, pulsating and reciprocating flows are finding more engineering

applications. For example, membrane driven micro-pumps and peristaltic micro-mixers result in pulsating flows [46, 47]. Several novel heat exchanger devices for electronic cooling applications utilize reciprocating flow and heat transfer [48, 49]. Reciprocating flows are also utilized to enhance mixing in micro-scales [50, 51].

Analyses of pulsating and reciprocating flow heat transfer differ from each other, mainly due to the thermal and velocity boundary conditions. Pulsating flows are uni-directional. Hence, they have permanent inflow and outflow regions, where one can easily define the inlet velocity and temperature boundary conditions. Reciprocating flows require interchange between the inflow and outflow boundaries during a cycle. For most applications, it is difficult to determine the inflow/outflow boundary conditions, since fluid particles exiting the flow domain during a part of the cycle are fed back into the domain, later in the cycle. Although the momentum equation yields an analytical solution for two-dimensional fully developed reciprocating channel flows, analytical solution of the heat transfer problem is not possible, unless the thermal boundary conditions are simplified. In this study, we mainly concentrate on reciprocating flow heat transfer. Hence, we will discuss the previous work on reciprocating flow heat transfer in detail. Some experimental, numerical and analytical studies on pulsating flow heat transfer can be found in [52, 53, 54, 55, 56, 57].

A literature survey on reciprocating flow heat transfer shows two different categories of investigations. The first one is focused on heat conduction enhancement with high frequency, low amplitude oscillations, while the second one is focused on forced convection with low frequency, large amplitude oscillations in relatively short channels. One of the early studies of the former category is due to Chatwin [58], who showed enhancement of species diffusion under high frequency oscillations. Later this phenomenon was applied to enhance heat transfer, where effective thermal diffusivities, that are about three orders of magnitudes higher than the values due to

molecular thermal diffusion, are achieved [59, 60].

Regarding the second category, Li and Yang [61] investigated heat transfer in reciprocating flows at low frequencies and large amplitudes by numerical simulations. They showed heat transfer enhancement due to the intra-cycle oscillations, which were caused by "sudden changes of the inlet and exit boundary conditions". Liao et al. [48] performed forced-convection experiments on microprocessor chips by means of channelled zero-mean oscillatory air flow. They measured the surface temperature of several power generating components in a typical personal computer, and reported heat transfer enhancement by oscillatory forced convection, compared to the conventional fan cooling. Based on the Reynolds number (Re), they distinguished two different heat transfer enhancement mechanisms. In the low Re regime, heat transfer enhancement was observed due to the reduction in the Stokes layer thickness with increased flow frequency. While for the high Re regime, heat transfer enhancement was observed due to the presence of "higher-order harmonics of imposed flow frequency". Cooper et al. [62] investigated forced convection heat transfer by heating the bottom wall section of a rectangular duct. Experiments were performed at low frequencies with large tidal displacements. The results showed enhanced heat transfer rates for increased oscillation frequencies and tidal displacements, and decreased duct heights. Chou et al. [63] used oscillatory flow to cool electronic devices. Their idea was to carry the heat away from the source using bubbles oscillating in a micro channel. Preliminary results show heat transfer enhancement caused by the oscillatory flow.

In this study, we present numerical solutions of reciprocating fluid flow and heat transfer in two-dimensional channels. This chapter is organized as follows. First, we further define the problem, and state the boundary conditions. Then the governing equations are presented. Fluid flow problem will be discussed by referring to the Navier-Stokes test problem we solved in Chapter 5. Next, the temperature field

results are presented and the effects of various flow and heat transfer parameters on time-periodic oscillatory forced convection are discussed. Finally, the results obtained for oscillatory flows will be compared with the ones for unidirectional flows.

B. Problem Definition and Important Parameters

A schematic view of the computational domain along with the associated boundary conditions is shown in Fig. 37. We consider fully reversing flow driven by an oscillatory pressure gradient. The middle portion of the top plate is uniformly heated, while its two sides are kept at constant temperature, and the bottom plate is insulated. The presence of constant temperature zones allows a time-periodic solution for the heat transfer problem. Periodic boundary conditions are specified at the two ends. The periodicity condition is such that fluid coming out of one side enters through the other side. Therefore, the velocity and temperature values are always the same at both ends. For a better understanding of the periodic boundary conditions, this problem can be visualized as a portion of an infinitely long channel with repeated constant temperature and constant heat flux sections as shown in Fig. 38. Such a configuration can be observed in electronic cooling applications, where the IC boards usually have a repeating pattern. For this application, our analysis would be valid sufficiently away from the device inlet/exit regions, where flow development effects are negligible.

In our simplified two-dimensional model, there are four important geometric length scales: channel height H^*, total channel length L^*, length of the heated portion of the channel L_h^*, where heat flux is applied, and the penetration length L_p^* (tidal displacement). Penetration length is the average distance travelled by fluid particles during one-half of an oscillation period ($\tau^*/2$). Considering sinusoidal oscillations,

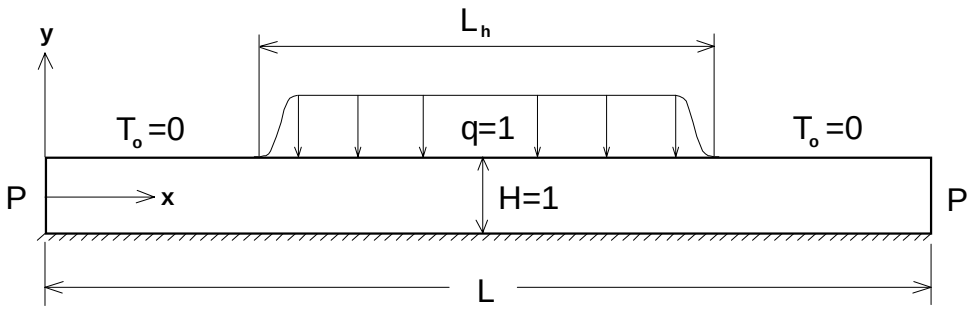

Fig. 37. The geometry and thermal boundary conditions used for the oscillatory flow forced convection problem. On the top surface, uniform heat flux is specified at $5 < x < 15$. For $4 < x < 5$ and $16 > x > 15$, the heat flux varies from zero to unity sinusoidally. Zero wall temperature is specified for $x < 4x < 16$. Bottom wall is insulated, while side surfaces are periodic.

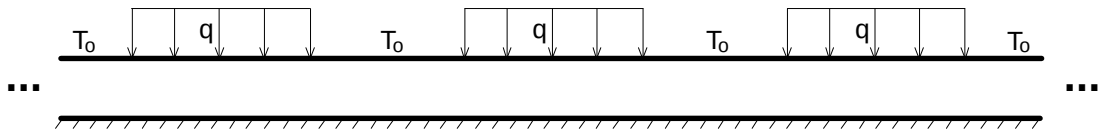

Fig. 38. Schematic view of a hypothetical problem that consists of a channel with repeating heated and constant temperature boundaries

the penetration length is defined as

$$L_p^* = \bar{\bar{u}}^* \frac{\pi}{\omega *} \tag{6.1}$$

where $\omega^* = 2\pi/\tau^*$ is the oscillation frequency and $\bar{\bar{u}}^*$ is the time- and cross-channel averaged axial velocity. The parameter L_p^* is a practical measure of the oscillation amplitude. For efficient cooling, L_p^* should be large enough so that the heated fluid under the constant heat-flux region will travel towards the constant temperature boundaries, where efficient heat transfer to the surroundings can take place.

For oscillatory flows the Womersley number is an important non-dimensional parameter, defined as

$$\alpha = \sqrt{\frac{\omega^* {H^*}^2}{\nu^*}} \tag{6.2}$$

The Womersley number determines the velocity profile. Small α values result in a quasi-steady flow with oscillatory parabolic velocity profiles. However, large α values lead to the well-known "Richardson's annular effect" that results in near-wall velocity overshoots, where the maximum velocity no longer occurs at the symmetry plane [56, 64]. This has direct effects on heat transfer, since high velocities with large gradients increase the heat removal rate from the surfaces. Zhao and Cheng [56] reported observing annular effects in the temperature profiles. This is also verified in our current study. The Womersley number is sometimes called the "kinetic Reynolds number" because it plays the same role as the Reynolds number in unidirectional steady flows. The Prandtl number (ratio of momentum and thermal diffusivities) is also important in heat transfer. For reciprocating flows, the thermal boundary layer thickness is determined by both the Prandtl and Womersley numbers.

Selecting the channel height H^* as the characteristic length scale, the important non-dimensional parameters are $L\ (= L^*/H^*),\ L_h\ (= L_h^*/H^*),\ L_p\ (= L_p^*/H^*),\ \alpha$ and

Pr. This five-parameter space makes it difficult to study the importance of every parameter in detail. Therefore, we fixed the normalized channel length L and the heated region length L_h, and varied L_p, α and Pr, by using two different values for each of these parameters. This results in eight different conditions, which are summarized in Table 1. The parameters appearing in Table 1 are all non-dimensional.

In our simulations the input parameters are L_p α and Pr. The flow is driven by an oscillatory pressure gradient given by,

$$\frac{\partial p^*}{\partial x^*} = -A^* cos(\omega^* t^*) \tag{6.3}$$

where p^* and A^* are the pressure and the pressure gradient, respectively. The amplitude A^* is directly related to $\bar{\bar{u}}^*$ introduced in Eq. (6.1). Its value is calculated using the analytical velocity profile, which will be demonstrated in the forthcoming sections.

Table I. Non-dimensional parameters used in the oscillatory forced convection simulations

Case no.	L	L_h	L_p	α	Pr	Re'
1	20	12	5	1	1	$5/\pi$
2	20	12	5	1	10	$5/\pi$
3	20	12	5	10	1	$500/\pi$
4	20	12	5	10	10	$500/\pi$
5	20	12	10	1	1	$10/\pi$
6	20	12	10	1	10	$10/\pi$
7	20	12	10	10	1	$1000/\pi$
8	20	12	10	10	10	$1000/\pi$

C. Non-Dimensionalization and Governing Equations

Numerical simulations are performed using non-dimensional parameters. The length, time, velocity, pressure, temperature and heat flux are normalized as follows:

$$\begin{aligned} x &= \frac{x^*}{H^*} \qquad y = \frac{y^*}{H^*} \qquad t = \frac{t^*}{1/\omega^*} \qquad u = \frac{u^*}{\omega^* H^*} \\ p &= \frac{p^*}{\rho^*(\omega^* H^*)^2} \qquad T = \frac{T^* - T_o^*}{\Delta T^*} \qquad q = \frac{q^*}{k^* \Delta T^*/H^*} = 1 \end{aligned} \tag{6.4}$$

where the velocity is normalized by $\omega^* H^*$ due to the lack of a characteristic velocity scale in the problem. In Eq. (6.4), T^* and q^* represent the temperature and heat flux, respectively, while the specified wall temperature is T_o^*, and ΔT^* is a reference temperature difference in the domain. Since there is only one reference temperature value on the wall (T_o^*) and uniform or zero heat flux conditions are specified on the rest of the boundary, ΔT^* is determined in the post-processing stage. We calculate the appropriate value for ΔT^* using the maximum allowable temperature difference in the flow domain (based on the design considerations) and the calculated maximum nondimensional temperature (T_{max}). As an example, lets consider an electronic cooling application, where the maximum temperature difference between the ambient and the chip surface is 30^oC. If our simulation results in $T_{max} = 2$, then $\Delta T^* = 15^oC$. We can calculate the maximum possible heat dissipation q^* from the system using $q^* = qk\Delta T^*/H^*$. Alternatively, one can select the desired heat flux q^*, and calculate ΔT^* to find the maximum surface temperature. This normalization makes it easier to utilize dynamic similarity for obtaining the dimensional temperature and heat flux values.

Governing equations are the conservation of mass, incompressible Navier-Stokes

and heat transport equations, presented in the following non-dimensional form,

$$\nabla \cdot \vec{u} = 0 \tag{6.5a}$$

$$\frac{\partial \vec{u}}{\partial t} + (\vec{u} \cdot \nabla)\vec{u} = -\nabla p + \frac{1}{Re}\nabla^2 \vec{u} \tag{6.5b}$$

$$\frac{\partial T}{\partial t} + (\vec{u} \cdot \nabla)T = \frac{1}{Pe}\nabla^2 T \tag{6.5c}$$

where $Re = \alpha^2$ for oscillatory flows. Thermal conduction coefficient and viscosity are assumed to be constant and the viscous heating terms in the heat transport equation are neglected. These assumptions and approximations are consistent with the previous analytical and numerical studies. As will be discussed in the next section, the velocity field for this problem has an available analytical solution. Therefore solution of only the heat transport equation, which is a scalar convection-diffusion equation, is sufficient.

At this point it is worthwhile to mention that the flow inside the channel is hydrodynamically-fully-developed (i.e. the streamwise gradient of the velocity vector is zero) at all times. Based on Fig. 38 and the discussion about the periodic end conditions, fully-developed flow is automatically satisfied. Therefore, the entry and flow development effects are excluded in the current study.

D. Analytical Solution of the Velocity Field

As studied in Chapter 4, the analytical solution of the oscillatory flow in a two-dimensional channel is known. Consider the flow between two parallel plates, driven harmonically in time with a pressure gradient of the following form,

$$\frac{\partial p}{\partial x} = -Ae^{-it} \tag{6.6}$$

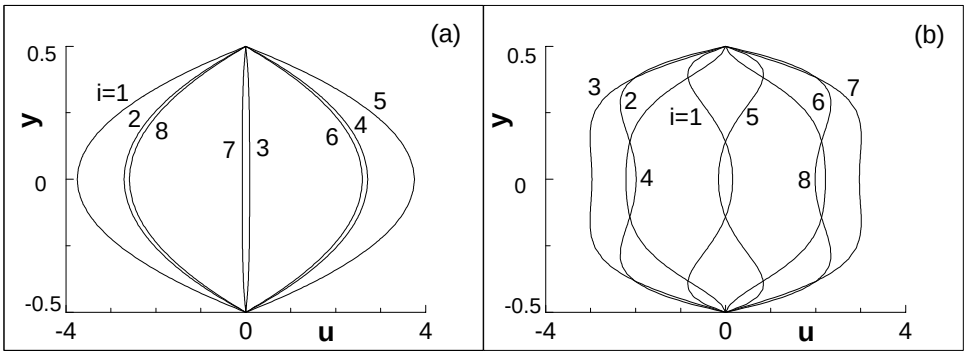

Fig. 39. Analytical solution of the velocity profiles at various times during a cycle for (a) $\alpha = 1$, (b) $\alpha = 10$ flow. Index i represents time within a period of the pressure pulse ($t = (i-1)/8\tau$).

where A is the pressure gradient normalized with ($\rho^*\ \omega^{*2}\ H^{*3}$), and $i = \sqrt{-1}$. The velocity profile for this flow is given by [41]

$$u(y,t) = Real\left\{ iAe^{-it}\left[1 - \frac{cos\left(\frac{(i+1)\sqrt{2}}{\alpha}y\right)}{cos\left(\frac{(i+1)}{\sqrt{2}\alpha}\right)}\right]\right\} \tag{6.7}$$

where y is the cross channel distance normalized by the channel height H^*. Fig. 39 shows the velocity profiles at various instances during a cycle for $\alpha = 1$ and $\alpha = 10$ flows. Quasi-steady flow behavior is observed for $\alpha = 1$, while the Richardson's annular effect is present for $\alpha = 10$.

The time- and cross-channel-averaged velocity $\bar{\bar{u}}$ is obtained by integrating Eq. (6.7) as follows,

$$\bar{\bar{u}} = \frac{1}{\tau H}\int_0^{\tau}\int_{-H/2}^{H/2} u(y,t)\ dy\ dt \tag{6.8}$$

where $\tau = 2\pi$ (radians) is the normalized oscillation period and $H = 1$ is the normalized channel height. This integral is evaluated numerically, and $\bar{\bar{u}} = 0.0528A$ and $\bar{\bar{u}} = 0.5647A$ are obtained for $\alpha = 1$ and $\alpha = 10$, respectively. For a desired tidal displacement L_p, we calculate the corresponding pressure amplitude A, using $\bar{\bar{u}} = L_p/\pi$,

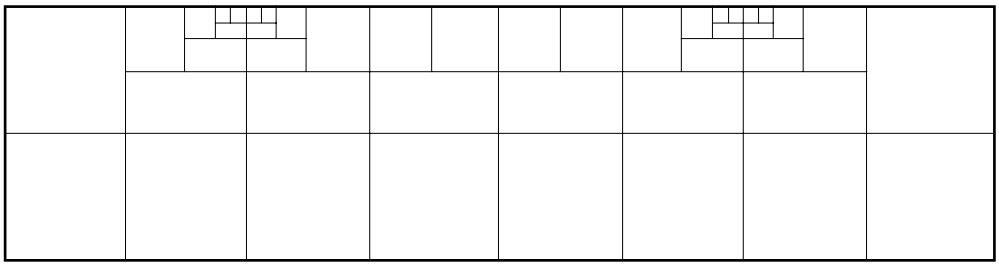

Fig. 40. A typical mesh used for the solution of the heat transfer problem that takes advantage of h- and p-type nonconforming elements, as well as anisotropic expansions (elements with $N_x \neq N_y$).

which is a non-dimensional form of Eq. (6.1).

The spatial convergence characteristics of our solver is already discussed in the first test problem solved in Chapter 4 (see Fig. 32). For the solution of the heat transfer part of the problem a typical mesh shown in Fig. 40 will be used. This mesh takes advantage of h- and p-type nonconforming elements, as well as anisotropic expansions (elements with $N_x \neq N_y$). At the top wall, temperature is discontinuous at two locations, where the Neumann and Dirichlet boundaries meet. These boundary condition singularities can be handled with proper h-type refinement. As will be seen from the results, close to the side walls, solution does not have sharp gradients, therefore the use relatively large elements are appropriate. Accurate approximation of the specified heat flux conditions at the top and bottom walls are crucial to the overall accuracy of the solution. This can effectively be achieved by using anisotropic expansion in the elements adjacent to the top and bottom walls, i.e. using higher order expansions in the direction perpendicular to the walls.

E. Results

In this section we present detailed analyses of temperature field and heat transfer results for the cases presented in Table 1. We examine the effects of the Prandtl and

the Womersley numbers as well as the tidal displacement on heat transfer. The results presented in the following sections are obtained after the simulations have reached their corresponding time-periodic states.

1. Temperature Contours

We present snapshots of temperature contours for cases 2, 4, 6 and 8 (Pr=10) in Fig. 41. These snapshots are synchronized with the pressure pulse, and they are obtained at 0τ, $1/8\tau$, $1/4\tau$ and $3/8\tau$. Comparisons of cases in the horizontal and vertical directions indicate the effects of α and L_p, respectively. The left column (cases 2 and 6) shows temperature contours oscillating back and forth with rather monotonic shapes. Especially for case 2, temperature contours across the channel are almost uniform at any time. Small L_p and α values for case 2 result in the lowest axial velocities. Hence, conduction (in the axial direction) dominates over convection, as can be deduced from the temperature contours. For case 2, the hot fluid pocket under the heat source is not effectively convecting towards the cold walls. Case 6 has twice the tidal displacement of case 2, and it shows stronger cross-channel temperature variations. Values of the normalized temperature are significantly reduced from case 2 to case 6, indicating increased convective cooling with increased tidal displacement L_p. Large cross-channel temperature variations are observed for cases 4 and 8, which correspond to $\alpha = 10$ flows. Case 8 has the highest L_p and α values used in this work. Temperature contours for this case concentrate near the top surface, which indicates thin thermal boundary layers and enhanced forced convection. Temperature values are also significantly lower than the other cases. Our overall observation from Fig. 41 is that the normalized fluid temperature in the channels are decreased with increased tidal displacement L_p and Womersley number α, and the temperature distribution in the channel is highly affected by the velocity profile.

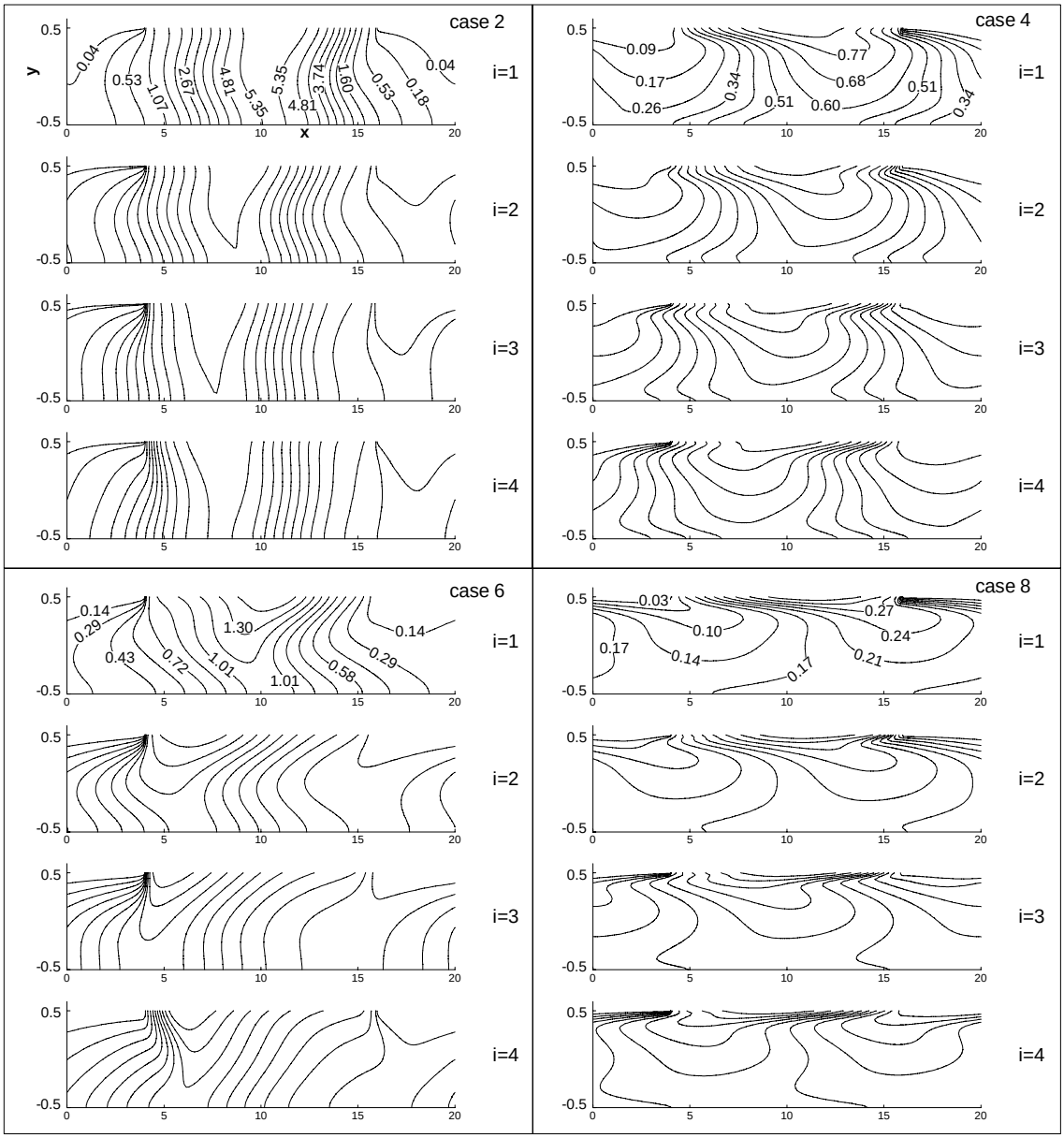

Fig. 41. Instantaneous temperature contours for cases 2, 4, 6 and 8. Index i represents time within half a period of the pressure pulse ($t = (i-1)/8\tau$). The flow and thermal conditions are presented in Table 1.

2. Temperature Profiles

Detailed descriptions of temperature profiles for reciprocating flows are not common in the literature. In Fig. 42, we present the temperature distribution at $x = 5$ (solid-lines) and $x = 10$ (dashed-lines) for all cases. Each figure shows the temperature profiles obtained at eight different instances. These snapshots are synchronized with the velocity profiles, which are shown at the bottom of the figure. The abscissa shows the temperature value, while the ordinate shows the cross-channel coordinate. The location $x = 10$ corresponds to the geometric center of the channel, where non-dimensional heat flux of $q = 1$ is imposed on the top wall. Due to the symmetry plane at $x = 10$, temperature profiles at this location repeat twice cyclically from $i = 1$ to 4, while the temperature profiles at $x = 5$ cycle from $i = 1$ to 8. In Fig. 42, the top four cases (1, 2, 5 and 6) are obtained under oscillatory parabolic velocity profiles ($\alpha = 1$), while the bottom four cases (3, 4, 7 and 8) are obtained for $\alpha = 10$ flow. For $\alpha = 10$ cases, sharp velocity gradients near the walls result in enhanced oscillations in the temperature profiles. For example, the temperature profile in case 7 has as many as five inflection points at times $i = 2, 3, 5, 6$. It is clear from these results that the Richardson's annular effect, which exists in the velocity profiles at large frequencies, affects the temperature profiles. For case 1, temperature profiles are almost uniform at all times. An increase in the tidal displacement L_p results in monotonic temperature variations, as shown in case 5. In cases 1 and 2, temperature values at $x = 10$ are higher than the values at $x = 5$, which is an indication of hot fluid being stuck under the heated region. The comparison of cases 6 and 7 in Fig. 42 shows that an increased Womersley number results in localized temperature gradients near the top wall with sudden temperature fluctuations. An increase in the Prandtl number creates sharper temperature variations in the cross-flow direction, as can be

seen by a comparison of cases 7 and 8. It is interesting to note that for a given axial location, the bottom wall temperature for cases 4, 7 and 8 remains almost constant throughout the cycle. All of these cases have a large α value, which corresponds to a large Re and enhanced convection. Heat supplied from the top plate rapidly convects along the channel and most of the thermal activity is occurring near the top wall. These cases result in bulk temperatures that are significantly lower than the surface temperatures, which results in high Nusselt numbers, as discussed in detail in the following sections.

3. Top-Wall Temperature Variations

In electronic cooling applications, exceeding a certain temperature may result in chip failure. Therefore, the maximum surface temperature is an important design parameter. In addition to the maximum surface temperature, the time of exposure to high temperatures also plays an important role. Figure 43 shows top wall temperatures at five different instances during half a cycle. Comparison of the left ($L_p = 5$) and right ($L_p = 10$) columns shows that the maximum top wall temperature for low penetration length simulations occurs in a narrowly bounded region near the channel center. However for $L_p = 10$, the location of the maximum surface temperature is oscillating throughout the entire heated region. Comparisons of all eight cases show that the maximum surface temperature decreases with increased L_p, α and Pr.

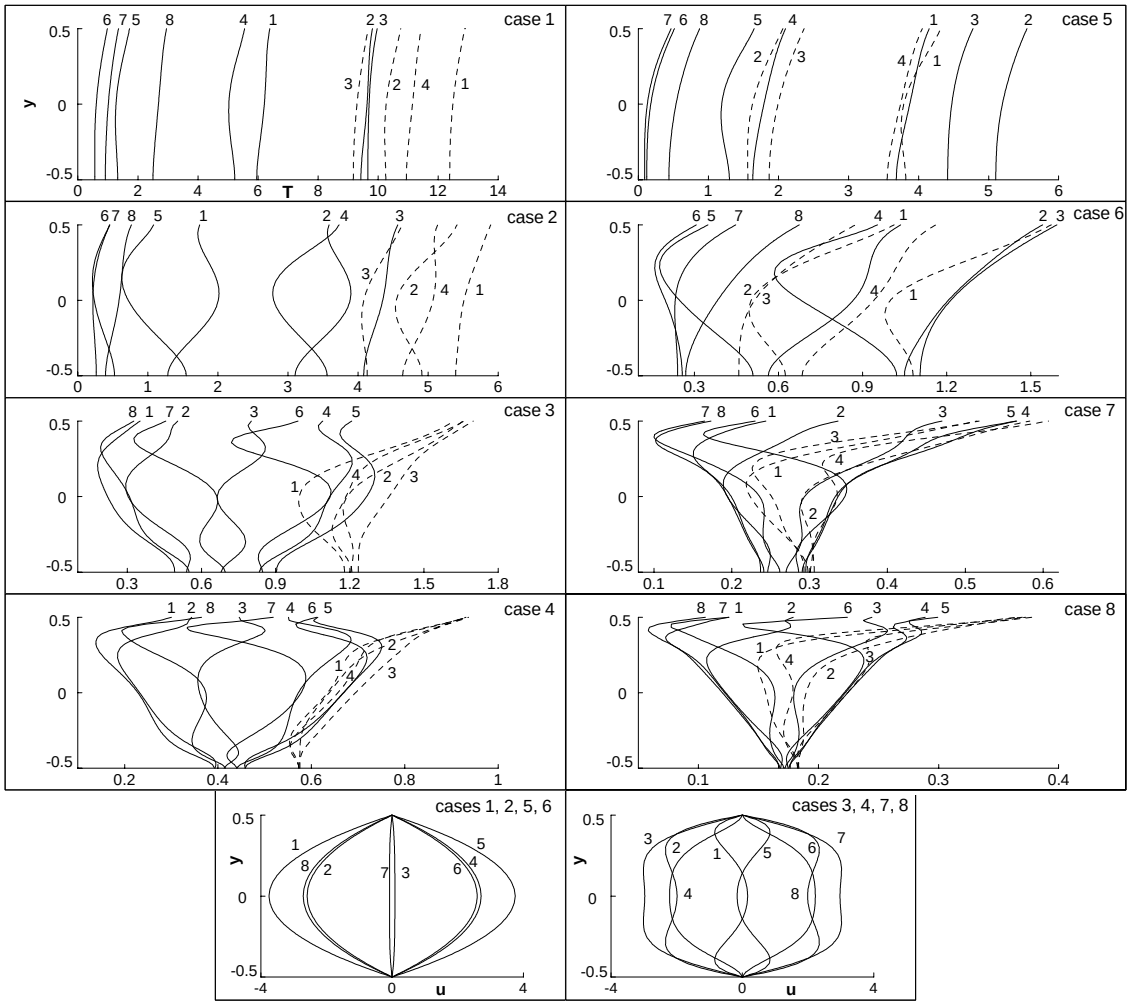

Fig. 42. Instantaneous temperature and velocity profiles at axial locations of $x = 5$ (solid-lines) and $x = 10$ (dashed-lines). Index i represents time within a period of the pressure pulse ($t = (i-1)/8\tau$). Simulation parameters are presented in Table 1.

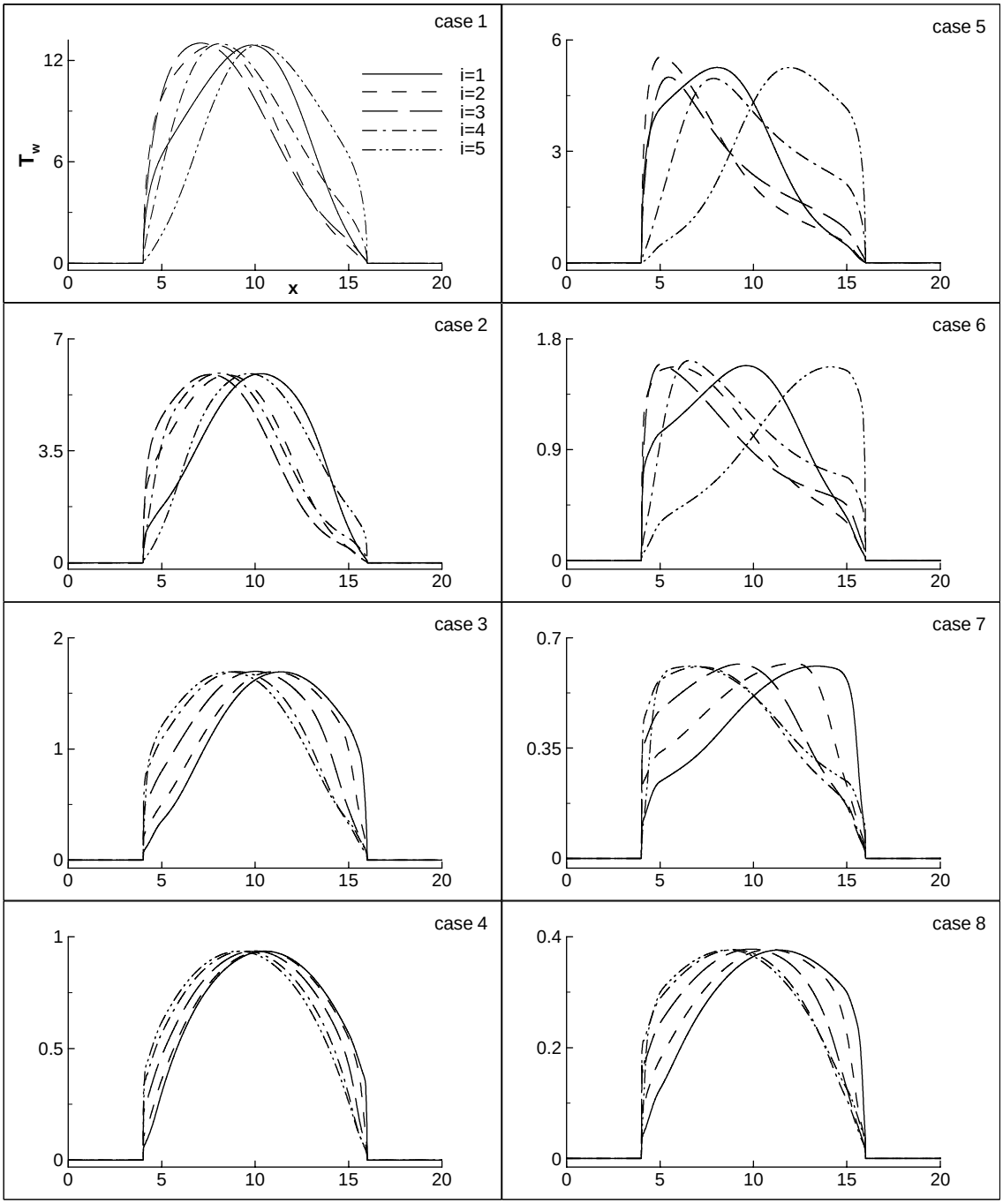

Fig. 43. Instantaneous top-wall temperatures. Index i represents time within half a period of the pressure pulse ($t = (i-1)/8\tau$). Simulation parameters are presented in Table 1.

4. Bulk Temperature and the Nusselt Number

Bulk temperature is an important parameter, used in the calculation of the Nusselt number. Classical definition of the bulk temperature is

$$T_b(x,t) = \frac{\frac{1}{H}\int_{-H/2}^{H/2} u(y,t)\ T(x,y,t)\ dy}{\frac{1}{H}\int_{-H/2}^{H/2} u(y,t)\ dy} \tag{6.9}$$

This definition is not preferred in a reciprocating flow, because the denominator becomes zero twice during a cycle. To overcome this difficulty, we defined a time-averaged bulk temperature in the following form,

$$\bar{T_b}(x) = \frac{\frac{1}{\tau H}\int_0^{\tau}\int_{-H/2}^{H/2} |u(y,t)|\ T(x,y,t)\ dy\ dt}{\bar{\bar{u}}}. \tag{6.10}$$

The absolute value in the numerator is used in order to avoid negative bulk temperatures during the flow reversal. An alternative definition can utilize time integration over a half cycle rather than a full cycle, which will yield the same result due to the half-period symmetry of the velocity and temperature fields.

Figure 44 shows axial variations of time-averaged top-wall (solid lines) and bulk (dashed lines) temperatures. The dashed-dotted and dashed-dotted-dotted lines in the figure correspond to unidirectional steady forced convection cases, which will be discussed in the next section. This figure shows that both the time-averaged wall temperature and bulk temperature decrease with increasing L_p, α and Pr. For $\alpha = 1$ cases (top four plots), the bulk temperature values are close to the time-averaged wall temperature at $5 < x < 15$. This is especially noticeable for cases 1 and 2. On the other hand, bulk temperatures for cases 7 and 8 are almost half of the time-averaged wall temperatures at $5 < x < 10$. Here we mention that cases 7 and 8 are

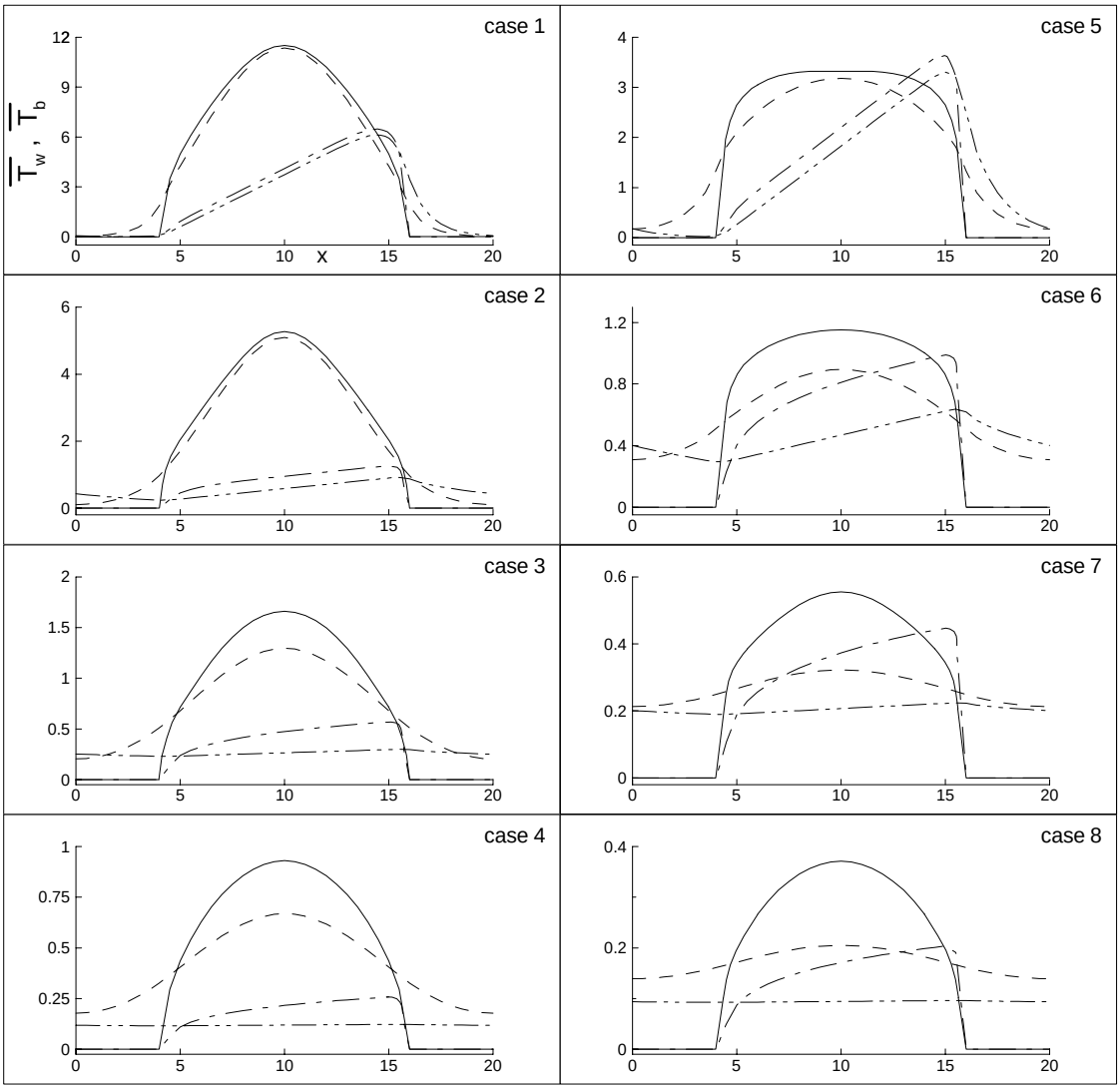

Fig. 44. Time-averaged wall-temperature (solid lines) and time-averaged bulk temperature (dashed-lines) variations for reciprocating flows. Wall temperature (dashed-dotted lines) and bulk temperature (dashed-dotted-dotted lines) variations for unidirectional steady flows are also shown. Simulation parameters are presented in Table 1.

the most effective in evenly spreading heat to the entire channel, as can be seen from their almost flat bulk temperature distributions. This also shows enhanced forced convection cooling for these cases.

In the simulations we specified a nondimensional constant heat flux value of unity in the region $5 < x < 15$. For $q = 1$, the time-averaged Nusselt number can be calculated as [49]

$$\overline{Nu}(x) = \frac{2}{\bar{T}_w - \bar{T}_b} \tag{6.11}$$

Variations of time-averaged Nusselt number along the heated portion of the channel are shown in Fig. 45a. We separated the low and high Womersley number cases. For $\alpha = 1$ (cases 1, 2, 5 and 6), the maximum $\overline{Nu}$ occurs at the middle of the channel ($x = 10$). For these cases, slight increases at $x = 5$ and $x = 15$ are due to the change in the boundary conditions (See Fig. 37). Specifically, the wall temperature suddenly drops to zero at $x = 4$ and $x = 16$, while the bulk temperature is decreasing gradually. These variations in the boundary conditions result in localized increases in the Nusselt number. It is interesting to notice that the tidal displacement and Prandtl number are both important here. Case 6 shows an almost uniform time averaged Nusselt number in the heated zone, which is an indication of effective heat transfer. The results for $\alpha = 10$ are shown on the top left figure. For cases 3, 4, 7 and 8, the maximum $\overline{Nu}$ occurs at both ends of the heated region, whereas the minimum $\overline{Nu}$ occurs at the channel center. Comparing case 3 with case 4 (or case 7 with case 8), we observe that the time averaged Nusselt number is increased by increasing the Prandtl number. Comparing case 3 with case 7 (or case 4 with case 8) shows that increasing the tidal displacement increases the Nusselt number. Finally, comparing cases 6 and 8 shows that $\overline{Nu}$ increases with the Womersley number.

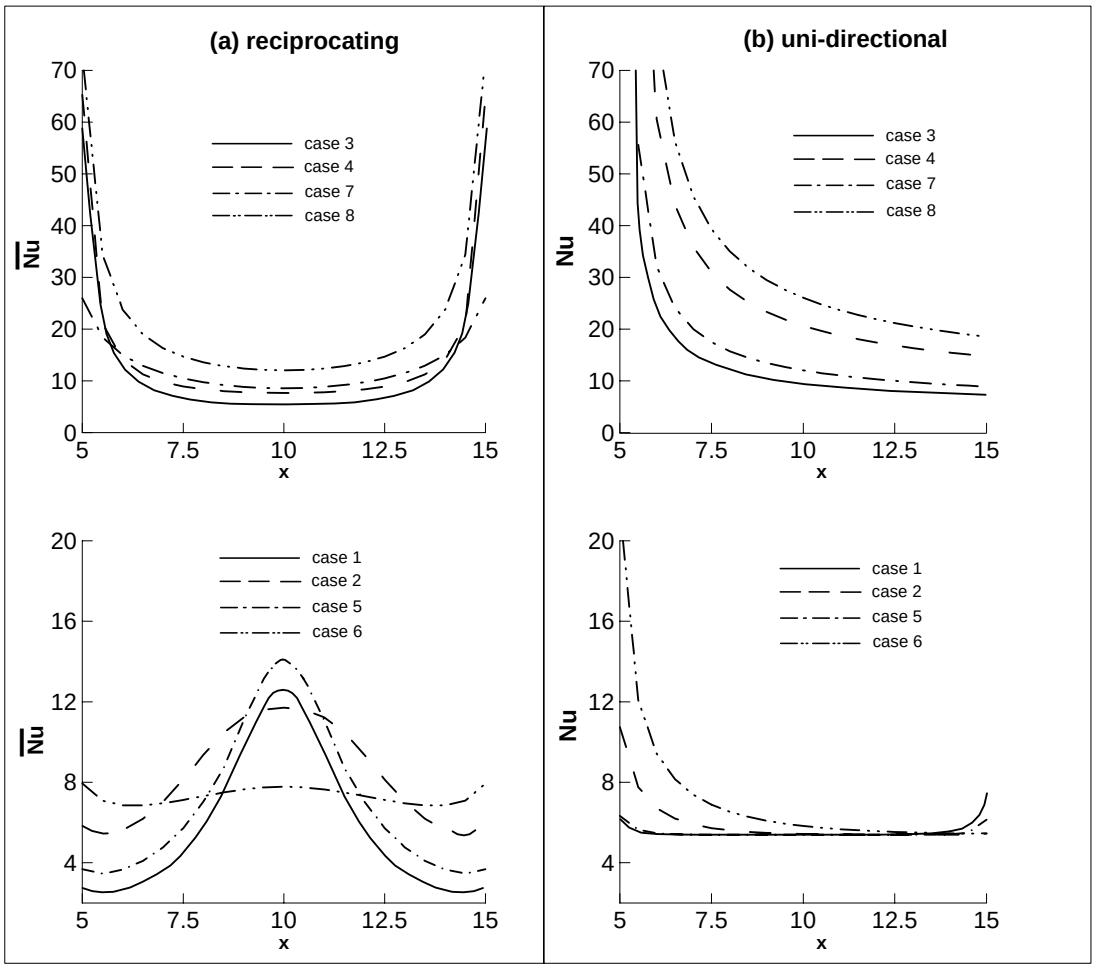

Fig. 45. Axial distribution of time-averaged Nusselt number for (a) reciprocating, (b) unidirectional steady flows. Simulation parameters are presented in Table 1.

5. Steady Unidirectional Forced Convection

In this section, previously obtained oscillatory flow temperature and Nusselt number results are compared against the steady, unidirectional forced convection. We match the oscillatory and unidirectional flows by matching the time-averaged flowrate. Reynolds number of the corresponding unidirectional flows is calculated by

$$Re' = \frac{\bar{\bar{u}}^* H^*}{\nu *} = \frac{\alpha^2 {L_p}^*}{\pi H^*} \tag{6.12}$$

which is presented in Table 1. The velocity and temperature boundary conditions at the channel ends are periodic. Flow is from left to right, and it is maintained by a constant pressure gradient. The resultant velocity profiles are parabolic, typical of pressure driven laminar flows. Due to the periodic temperature boundary conditions, fluid leaving from the right boundary is entering from the left with a temperature equal to the exit temperature. Numerical results correspond to the steady state conditions.

Bulk and wall temperature variations along the channel are shown in Fig. 44 using dashed-dotted-dotted and dashed-dotted lines, respectively. For cases 1, 2 and 5, bulk and wall temperatures increase linearly with the same slope in most of the heated region, indicating thermally developed flow. We also observe that case 6 is *almost* thermally developed. Cases 1, 2, 5 and 6 correspond to low Reynolds numbers ($Re' < 4$), resulting in relatively small Peclet numbers. Cases 3, 4, 7 and 8 correspond to Reynolds numbers that are two orders-of-magnitude higher than the corresponding low Reynolds number cases (See Table 1). This is due to the quadratic dependence of the Reynolds number on the Womersley number, given by Eq. (6.12). For these cases, thermally developed conditions are not observed. In all of the cases, unidirectional forced convection results in smaller bulk and surface temperatures than the recipro-

cating flow, with the exception of case 5. In addition, we note that time-averaged top wall temperatures in Fig. 44 are less than the instantaneous maximum wall temperature shown in Fig. 43. Low L_p cases (cases 1, 2, 3 and 4) give considerably higher maximum wall temperatures than their unidirectional flow counterparts. For cases 4 and 8, the bulk temperature of the unidirectional flows are almost uniform throughout the channel, and these cases correspond to the maximum Peclet numbers simulated in our work. Unidirectional flows result in increasing surface temperatures in the downstream direction, where oscillatory flows experience oscillating temperature maxima, as can be seen from Figs. 44, and 43, respectively. This basic difference may become important for various applications.

Nusselt number variations of unidirectional steady flows in the heated region are shown in Fig. 45b. Maximum Nusselt number is observed at the entrance of the heated region and decreases continuously. Two exceptions are the slight increases seen at $x = 15$ for cases 1 and 5. These cases have the lowest Pe, and local increase in the Nusselt number is due to noticeable heat conduction in the upstream direction. Cases 1, 2 and 5 have reached thermally developed conditions with constant Nusselt number of 5.387, a value very close to 5.3846 given by [44]. Cases 3, 4, 7, and 8 correspond to high Peclet numbers. For these cases, high Nusselt numbers are observed due to the thermally developing flow conditions.

F. Summary of Oscillatory Forced Convection Studies

Motivated by its potential in electronic cooling and microfluidics applications, we simulated reciprocating flow forced convection in two-dimensional channels, and compared our results with the corresponding unidirectional flows. We assumed a cyclically repeating flow section and imposed periodicity of velocity and temperature fields at

the sides of the computational domain. To our knowledge, periodic thermal boundary conditions in reciprocating flows have not been investigated before. Simulation results indicate that the instantaneous and time-averaged surface temperatures, and the time-averaged bulk temperature are reduced by increasing the penetration length, Womersley and Prandtl numbers. Therefore, it is possible to determine a combination of L_p, α and Pr that will keep the maximum surface temperature below a desired value, which is important for cooling applications. Unlike unidirectional flows, reciprocating flows convect heat to both sides of the heated region. This results in oscillation of the maximum surface temperature along the heated region of the channel, which may be advantageous over unidirectional forced convection, where the maximum surface temperature occurs at the exit of the heated region.

Numerical simulations show an increase of the time-averaged Nusselt number with increasing α, Pr and L_p. Variation of the time-averaged Nusselt number along the heated region of the channel shows different trends for $\alpha = 1$ and $\alpha = 10$ flows, indicating that velocity profiles have strong influences on the heat transfer characteristics. Richardson's annular effect, observed in the velocity profiles for high frequency oscillatory flows, affects the temperature profiles and heat transfer characteristics, as shown by the instantaneous temperature contours and profiles. Unidirectional flows corresponding to $\alpha = 1$ cases show thermally fully developed conditions towards the downstream portion of the channel. For these cases, the reciprocating flow Nusselt numbers is comparable to or higher than the corresponding unidirectional flow cases. Overall unidirectional flows resulted in smaller surface temperatures than the reciprocating flows. However, we believe that with proper combinations of the parameters, heat transfer rates higher than the corresponding unidirectional flows can be achieved. In future studies, a larger parameter space will be explored by varying the heated length (L_h) and the total length (L) of the channel.

Finally, temperature dependence of fluid properties, viscous heating and three-dimensionality effects are not considered. Temperature dependence of fluid properties is significant for large temperature variations. This may be checked by calculating the maximum temperature difference ΔT^* obtained for a desired heat flux value. Viscous heating may become important for high Re flows. Three-dimensionality effects are important for turbulent channel flows; but all cases studied here, including the steady unidirectional flows, fall into the laminar flow regime.

CHAPTER VII

SUMMARY AND DISCUSSIONS

Spectral Element Methods (SEM) combine the exponential convergence properties of global Spectral Methods with the domain discretization capability of low-order Finite Elements Methods (FEM). SEM provides fast convergence and small diffusion and dispersion errors. It enables easier implementation of the *inf-sup* condition for incompressible Navier-Stokes equations. Due to the elemental structure, it exhibits larger volume-to-surface data ratio that is suitable for efficient parallel processing. It provides better input/output handling due to the smaller volume of data compared to low-order methods that require relatively larger degrees of freedom [19]. However, SEM divides the problem domain into macro elements, much larger than the elements required by a finite element solution. These rather large elements limits the geometric discretization flexibility, especially when domains have boundaries with fine scale details. Also for domains with geometric singularities and for solutions with low regularity, high-order methods may not provide better accuracy than the low-order ones [34]. These deficiencies might be resolved by the implementation of nonconforming formulations. Nonconforming elements are also a necessity for adaptive refinement strategies.

Motivated by the geometric flexibility and high accuracy they offer, we investigated the Galerkin SEM on nonconforming configurations, with an emphasis on thermo-fluidics applications. Galerkin SEM solvers, based on Legendre polynomials on isoparametric elements, are developed for common differential operators and incompressible Navier-Stokes equations. Below is a summary of the contributions of this work.

- A review of the existing literature clearly shows a lack of consistent terminology for nonconforming formulations. We defined the following terms, many of which are first used in this study

  p-type nonconformity: The condition of having an interface of two elements, which are geometrically matching, but the polynomial orders used in each element are different. *h-type nonconformity:* The condition of having an interface of multiple elements (three in case of a 1-irregular grid), which are geometrically not matching, i.e. the intersection of the faces sharing the interface is not a whole face or vertex. *Maximum rule:* For a p-type nonconformity, using the face with higher expansion order as the active face. *Minimum rule:* For a p-type nonconformity, using the face with lower expansion order as the active face. *Long rule:* For an h-type nonconformity, using the longer face as the active face. *Short rule:* For an h-type nonconformity, using the two short faces as the active faces (valid for 1-irregular grids).

- Two most popular nonconforming configurations, namely the Constrained Approximation Method (CAM) and the Mortar Element Method (MEM) are discussed in detail for both p- and h-type nonconformities. CAM is the preferred method in finite element community, whereas MEM is mostly used with spectral formulations. The literature studying these two methods together are very limited. In this thesis we studied them in a comparative way. We began with the basic formulations, providing visual descriptions and step by step formulations of CAM and MEM. The formulations for p- and h-type nonconformites are discussed separately using sample mesh configurations.

- We studied the convergence characteristics of CAM and MEM for the steady diffusion operator. We discussed in detail the problems of using the maximum

rule with CAM, where consistency errors dominates, resulting in the loss of spectral convergence. The problem is more severe with p-type nonconformities, but does not exist for MEM. In case of the minimum rule CAM and MEM provide results with comparable accuracy.

- We studied the eigenvalue spectrum of CAM and MEM for the unsteady convection operator. p- and h-type conformities are investigated separately. We concluded that, for p-type nonconformities CAM and MEM has the same eigenvalue spectrums. When maximum rule is used for p-type nonconformities, the consistency errors due to the nonconforming configurations shift some of the eigenvalues into the positive real eigen-plane. The direction of the flow (whether it is going from a low order element to a high order one or vice versa) plays a role in this shift. We correctly linked this shift of eigenvalues to the use of maximum or minimum rules and not to the use of CAM or MEM. The situation is similar for h-type nonconformities, where the shift is larger for MEM (due to the use of the short rule) compared to CAM (which uses the long rule). Effect of the eigenvalues with positive real parts on the convergence of the unsteady convection problem are also studied. It is shown that pure convection problems on nonconforming grids do not provide successful results due to consistency problems. Coupled space-time formulations are also used to correctly identify the source of these problems to be the consistency errors coming from nonconforming formulations.

- Steady and unsteady incompressible Stokes and Navier-Stokes equations are studied using the Uzawa technique. The developed flow solvers are validated using a number of test problems on nonconforming grids. For the problems with known exact solution, spectral convergence is demonstrated using both

CAM and MEM. Once again, it is shown that, although it uses more degrees of freedom, the maximum rule does not perform as good as the minimum rule. We reported that CAM and MEM provide comparable results, with no distinct advantage of one over the other.

- Finally we used the developed solvers in a detailed parametric analysis of the oscillatory flow forced convection cooling in two-dimensional channels. We took advantage of p- and h-type nonconformities and anisotropic expansions to properly resolve boundary condition singularities and thin thermal boundary layers. We studied the affects of the penetration length, Womersley number and Prandtl number on the heat transfer characteristics of oscillatory flows. We provided temperature profiles and contours, bulk and wall temperature and Nusselt number distributions. We compared the results with corresponding unidirectional flows and concluded that in the investigated parameter range, unidirectional flows provide higher heat removal rates.

Based on the present study we make the following suggestions for future work

- We plan to optimize our algorithms to enable efficient use of computational time. We want to continue to take advantage of the simplicity of direct solvers with the help of the static condensation technique. Studies about the implementation of multi-level static condensation [19] that provides effective parallelization, will be helpful.

- Nonconforming formulations becomes more effective when coupled with adaptive refinement strategies. We plan to work on the effective use of adaptive algorithms, which includes studies on posteriori error estimators and efficient and easy to use data storage mechanisms [23, 30, 31].

REFERENCES

[1] C. Canuto, M. Y. Hussaini, A. Quarterino and T. A. Zang, *Spectral Methods in Fluid Dynamics*, New York: Springer-Verlag, 1988.

[2] D. Gottlieb and J. S. Hesthaven, *Spectral Methods for Time-Dependent Problems*, New York: Cambridge University Press, 2001.

[3] J. P. Boyd, *Chebyshev and Fourier Spectral Methods*, 2nd ed., Mineola, NY: Dover Publications, 2000.

[4] J. N. Reddy, *An Introduction to the Finite Element Method*, 2nd. ed., New York: McGraw-Hill, 1993.

[5] A. T. Patera, "A spectral element method for fluid dynamics, laminar flow in a channel expansion," *J. Comp. Phys.*, vol. 54, pp. 468–488, 1984.

[6] L. Demkowicz, J. T. Oden, W. Rachowicz and O. Hardy, "Toward a universal h-p adaptive finite element strategy: Part I: Constrained approximation and data structure," *Comp. Meth. Appl. Mech. Eng.*, vol. 77, pp. 79–112, 1989.

[7] C. Bernardi, Y. Maday, C. Mavriplis and A. T. Patera, "The mortar element method applied to spectral discretizations," in *Finite Element Analysis in Fluids, Seventh Int. Conf. on Finite Element Methods in Flow Problems*, Eds. T. J. Chung and G. R. Karr, Huntsville, AL: UAH Press, 1989.

[8] I. Babuska and M. Suri, "The p and h-p versions of the finite element method, basic principles and properties," *SIAM Rev.*, vol. 36, pp. 578–632, 1994.

[9] S. A. Orszag, "Numerical Methods for the simulation of turbulence," *Phys. Fluids*, vol. 12, pp. 250–257, 1969.

[10] S. A. Orszag, "Comparison of pseudospectral and spectral approximations," *Stud. Appl. Math.*, vol. 51, pp. 253–259, 1972.

[11] M. Y. Hussaini and T. A. Zang, "Spectral methods in fluid dynamics," *Ann. Rev. Fluid Mech.*, vol. 19, pp. 119–367, 1987.

[12] D. Gottlieb and S. A. Orszag, *Numerical Analysis of Spectral Method: Theory and Applications*, Philadelphia: SIAM, 1977.

[13] R. Peyret, *Spectral Methods for Incompressible Viscous Flow*, New York: Springer-Verlag, 2002.

[14] K. Z. Korczak and A. T. Patera, "An isoparametric spectral element method for solution of the Navier-Stokes equations in complex geometry," *J. Comp. Phys.*, vol. 62, pp. 361–382, 1986.

[15] Y. Maday and A. T. Patera, "Spectral element methods for the incompressible Navier-Stokes equations," in *State-of-the-Art Surveys on Computational Mechanics*, Ed. A. Noor, New York: ASME, pp. 71–143, 1989.

[16] E. M. Ronquist and A. T. Patera, "Spectral element multigrid. I. Formulation and numerical results,", *J. Sci. Comput.*, vol 2. pp. 389–406, 1987.

[17] P. F. Fischer, E. M. Ronquist and A. T. Patera, "Parallel spectral element methods for viscous flow," in *Parallel Supercomputing Methods, Algorithms and Applications*, Ed. G. F. Carey, Chichester, UK: Wiley, pp. 223-232, 1989.

[18] G. E. Karniadakis and R. D. Henderson, "Spectral element methods for incompressible flows," in *Handbook of Fluid Dynamics*, Ed. R. W. Johnson, Boca Raton, FL: CRC Press, pp. 29.1–29.41, 1998.

[19] G. E. Karniadakis and S. J. Sherwin, *Spectral /hp Element Methods for CFD*, New York: Oxford University Press, 1999.

[20] C. T. Tsai and B. A. Szabo, "A constraint method - A new finite element technique," in *NASA Technical Memorandum TM X-2893*, pp. 551–568, 1973.

[21] A. K. Gupta, "A finite element for transition from a fine to a coarse grid," *Int. J. Numer. Meth. Eng.*, vol. 12, pp. 35–45, 1978.

[22] W. Rachowicz and L. Demkowicz, "An hp-adaptive finite element method for electromagnetics Part I: Data structure and constrained approximation," *Comp. Meth. Appl. Mech. Eng.*, vol. 187, pp. 307–335, 2000.

[23] M. Ainsworth and B. Senior, "Aspects of an adaptive hp-finite element method: Adaptive strategy, conforming approximation and efficient solvers," *Comp. Meth. Appl. Mech. Eng.*, vol. 150, pp. 65–87, 1997.

[24] R-Y. Chang and C-H. Hsu, "A variable-order spectral element method for incompressible viscous flow simulation," *Int. J. Numer. Meth. Eng.*, vol. 39, pp. 2865–2887, 1996.

[25] D. Funaro, A. Quarteroni and P. Zanolli, "An iterative procedure with interface relaxation for domain decomposition methods," *SIAM J. Numer. Anal*, vol. 25, pp. 1213–1236, 1988.

[26] R. D. Henderson and G. E. Karniadakis, "Hybrid spectral element-low order methods for incompressible flows," *J. Sci. Comput.*, vol. 6, pp. 79-92, 1991.

[27] C. Bernardi, Y. Maday and A. T. Patera, "A new nonconforming approach to domain decomposition: The mortar element method," in *Nonlinear Partial*

Differential Equations and Their Applications XI, Eds. H. Brezis and J. L. Lions, Essex, UK: Longman, pp. 13–51, 1994.

[28] R. D. Henderson and G. E. Karniadakis, "Unstructured spectral element methods for simulation of turbulent flows," *J. Comp. Phys.*, vol. 122, pp. 191–217, 1995.

[29] E. M. Ronquist, "Convection treatment using spectral elements of different order," *Int. J. Numer. Meth. Fluids*, vol. 22, pp. 241–264, 1996.

[30] C. Mavriplis, "Adaptive mesh strategies for the spectral element method," *Comp. Meth. Appl. Mech. Eng.*, vol. 116, pp. 77–86, 1994.

[31] R. D. Henderson, "Dynamic refinement algoritms for spectral element methods," *Comp. Meth. Appl. Mech. Eng.*, vol. 175, pp. 395–411, 1999.

[32] C. Lacour and Y. Maday, "Two different approaches for matching nonconforming grids: The mortar element method and the FETI method," *BIT*, vol. 37, pp. 720–738, 1997.

[33] E. M. Ronquist and A. T. Patera, "A Legendre spectral element meethod for the Stefan problem," *Int. J. Numer. Meth. Eng.*, vol 24, pp. 2273–2299, 1987.

[34] C. Begue, C. Bernardi, N. Debit, Y. Maday, G. E. Karniadakis, C. Mavriplis and A. T. Patera, "Non-conforming spectral element-finite element approximations for partial differential equations," *Comp. Meth. Appl. Mech. Eng.*, vol. pp. 109–125, 1989.

[35] G. E. Karniadakis and A. Beskok, *Micro Flows: Fundamentals and Simulation*, New York: Springer-Verlag, 2002.

[36] P. M. Gresho, "Some current CFD issues relevant to the incompressible Navier-Stokes equations," *Comp. Meth. Appl. Mech. Eng.*, vol. 87, pp. 201–252, 1991.

[37] P. M. Gresho and R. L. Sani, "On pressure boundary conditions for the incompressible Navier-Stokes equations," *Int. J. Numer. Meth. Fluids*, vol. 7, pp. 1111–1145, 1987.

[38] P. M. Gresho, "On the theory of semi-implicit projection methods for viscous incompressible flow and its implementation via a finite element method that also introduces a nearly consistent mass matrix. Part I: Theory," *Int. J. Numer. Meth. Fluids*, vol. 11, pp. 587–620, 1990.

[39] G. E. Karniadakis, M. Israeli and S. A. Orszag, "High-order splitting methods for the incompressible Navier-Stokes equations," *J. Comp. Phys.*, vol. 97, pp. 414–443, 1991.

[40] M. R. Schumack, W. W. Schultz and J. P. Boyd, "Spectral element solution of the Stokes equations on nonstaggered grids," *J. Comp. Phys.*, vol. 94, pp. 30–58, 1991.

[41] L. D. Landau and E. M. Lifshitz, *Course of Theoretical Physics Volume 6 - Fluid Mechanics,* 2nd ed., New York: Pergamon Press, 1987.

[42] W. W. Schultz, N. Y. Lee and J. P. Boyd, "Chebyshev pseudospectral method of viscous flows with corner singularities," *J. Sci. Comput.*, vol. 4, pp. 1–24, 1989.

[43] O. Botella and R. Peyret, "Benchmark spectral results on the lid-driven cavity flow," *Comp. and Fluids*, vol. 27, pp. 421–433, 1998.

[44] R. K. Shah and A. L. London, "Laminar flow forced convection in ducts," in *Advances in Heat Transfer*, Eds. T. F. Irvine Jr. and J. P. Hartnett, New York: Academic Press, 1978.

[45] M. Zamir, *The Physics of Pulsatile Flow*, New York: Springer-Verlag, 2000.

[46] A. Beskok and T. C. Warburton, "Arbitrary Lagrangian Eulerian analysis of a bidirectional micro-pump using spectral elements," *Int. J. Comp. Eng. Sci.*, vol. 2, pp. 43–57, 2001.

[47] M. Yi, H. H. Bau and H. Hu, "A peristaltic meso-scale mixer," in *Proceedings of ASME IMECE Meeting*, MEMS vol. 2, pp. 367–374, 2000.

[48] Q. D. Liao, K. T. Yang and V. W. Nee, "Microprocessor chip cooling by channeled zero-mean oscillatory air flow," in *Advances in Electronics Packaging*, EEP vol. 10, pp. 789–794, 1995.

[49] C. Sert and A. Beskok, "Oscillatory flow forced convection in micro heat spreaders," *Numer. Heat Trans. Part A*, vol. 42, pp. 131–137, 2002.

[50] M. H. Oddy, J. G. Santiago and J. C. Mikkelsen, "Electrokinetic instability micromixing," *Analytical Chemistry*, vol. 73, pp. 5822-5832, 2001.

[51] P. Dutta and A. Beskok, "Time periodic electroosmotic flows: Analogies to Stokes' second problem," *Analytical Chemistry*, vol. 73, pp. 5097–5102, 2001.

[52] R. Siegel and M. Perlmutter, "Heat Transfer for Pulsating Laminar Duct Flow," *J. Heat Trans.*, vol. 84, pp. 111–123, 1962.

[53] R. Siegel, "Influence of oscillation-induced diffusion on heat transfer in a uniformly heated channel," *J. Heat Trans.*, vol. 109, pp. 244–247, 1987.

[54] S. Y. Kim, B. H. Kang and J. M. Hyun, "Heat transfer in the thermally developing region of a pulsating channel flow," *Int. J. Heat Mass Trans.*, vol. 36, pp. 4257–4266, 1993.

[55] T. Moschandreou and M. Zamir, "Heat transfer in a tube with pulsating flow and constant heat flux," *Int. J. Heat Mass Trans.*, vol. 40, pp. 2461–2466, 1997.

[56] T. Zhao and P. Cheng, "A numerical solution of laminar forced convection in a pipe subjected to a reciprocating flow," *Int. J. Heat Mass Trans.*, vol. 38, pp. 3011–3022, 1995.

[57] M. Greiner, P. F. Fischer and H. Tufo, "Numerical simulations of resonant heat transfer augmentation at low Reynolds numbers," in *Proceedings of ASME IMECE Meeting*, New York: HTD-24100, 2001.

[58] P. C. Chatwin, "The longitudinal dispersion of passive contaminant in oscillating flow in tubes," *J. Fluid Mech.*, vol. 71, pp. 513–527, 1975.

[59] U. H. Kurzweg and L. Zhao, "Heat transfer by high-frequency oscillations: A new hydrodynamic technique for achieving large effective thermal conductivities," *Phys. Fluids*, vol. 27, pp. 2624–2627, 1984.

[60] U. H. Kurzweg, "Enhanced heat conduction in oscillating viscous flows within parallel-plate channels," *J. Fluid Mech.*, vol. 156, pp. 291–300, 1985.

[61] P. Li and K. T. Yang, "Mechanisms for the heat transfer enhancement in zero-mean oscillatory flows in short channels," *Int. J. Heat Mass Trans.*, vol. 43, pp. 3551–3566, 2000.

[62] W. L. Cooper, V. W. Nee and K. T. Yang, "An experimental investigation of convective heat transfer from the heated floor of a rectangular duct to a low frequency large tidal displacement oscillatory flow," *Int. J. Heat Mass Trans.*, vol. 37, pp. 581–592, 1994.

[63] F-C. Chou, J-G. Weng and C-L. Tien, "Cooling of micro hot spots by oscillatory flow," in *Proceedings of 11th Int. Symp. on Transport Phenomena*, Hsinchu, Taiwan: pp. 324–329, 1998.

[64] E. G. Richardson and E. Tyler, "The transverse velocity gradient near the mouths of pipes in which an alternating or continuous flow of air is established," *Proc. Phys. Soc. London*, vol. 42, pp. 1–15, 1929.

[65] A. Beskok and T. C. Warburton, "An unstructured h/p finite element scheme for fluid flow and heat transport in moving domains," *J. Comp. Phys.*, vol. 174, pp. 492–509, 2001.

VITA

Cuneyt Sert graduated with a B.S. degree in mechanical engineering from Middle East Technical University, Ankara, Turkey in June 1996. He was ranked first in a graduating class of 190 students. He got his M.S. degree from the same department in June 1998. In June 1999, he joined the Department of Mechanical Engineering at Texas A&M University. He graduated with a Ph.D. degree in mechanical engineering in August 2003.

Cuneyt Sert may be contacted through Dr. Ali Beskok at the Mechanical Engineering Department, Texas A&M University, College Station, TX 77843-3123.